Cyprus
University of
Technology

Faculty of Engineering
and Technology
Department of
Mechanical Engineering
and Materials Science
and Engineering

Doctoral Thesis

INTERFACE ENGINEERING FOR EFFICIENT AND THERMALLY STABLE HYBRID PEROVSKITE PHOTOVOLTAICS

Fedros Galatopoulos

Supervisor: Professor Stelios Choulis

Limassol, September 2022

INTERFACE ENGINEERING FOR EFFICIENT AND THERMALLY STABLE HYBRID PEROVSKITE PHOTOVOLTAICS

Presented by

Fedros Galatopoulos

BEng Electronic Engineering

MSc Nanoelectronics and Nanotechnology

Submitted to the Department of Mechanical Engineering and Materials Science and Engineering in partial fulfillment of the requirements for the degree

Doctor of Philosophy

CYPRUS UNIVERSITY OF TECHNOLOGY

Supervisor: Professor Stelios Choulis

Signature ____

Committee President: Professor Lioz Etgar

Signature ____

Member of the committee: Professor Michael Saliba

Signature ____

Cyprus University of Technology, Limassol, September 2022

Intellectual rights

Copyright © Fedros Galatopoulos, 2022

All rights reserved.

The approval of the Doctoral thesis by the Department of Mechanical Engineering and Materials Science and Engineering does not imply necessarily the approval by the Department of the views of the writer.

Acknowledgements

First and foremost I would like to thank my supervisor, Prof. Stelios Choulis for the knowledge he has passed down on me throughout the years. Without his continuous support and guidance over the course of this study I would not be the scientist I am today. I would also like to thank Achilleas Savva for the training and knowledge he has provided me with, in order for my experimental work to come to fruition. Huge thanks are given also to my fellow MEP colleagues, Dr. Efthymios Georgiou, Dr. Sergey Pozov, Alexandra Chrysou, Dr. Apostolos Ioakeimidis, Dr. Ioannis Papadas and Ioanna Antoniou for their continuous support and enjoyable work environment that they have provided. Honorable mentions are also given to my past MEP colleagues Dr. Ignasi Burgues Ceballos, Dr. Dimitris Tsikritzis and Dr. Naoum Vaenas for their help. I would like to thank my PhD advisory committee, Prof. Soteris Kalogirou and Assoc. Prof. Tasos Georgiadis for their guidance and constructive feedback throughout the Thesis. I would also like to thank the external partners Prof. Nir Tessler, Prof. Gerasimos Armatas and Associate Professor Grigorios Itskos for the collaboration and assistance on various sections of the experimental work of this Thesis. Last but not least I would like to thank my family and friends for their continuous moral support over the years.

ABSTRACT

Organo-metal halide perovskite solar cells have been the center of attention in the photovoltaic research field over the last years as a strong candidate to replace the conventional Si-based technology. However complex device physics as well as intrinsic instability has left much to be desired by this technology. The focus of this thesis is to understand and improve the thermal stability of Hybrid Perovskite solar cells by interface engineering methods and development of high-performance electrodes.

Initially, the stability of p-i-n perovskite solar cells is studied under accelerated heat lifetime conditions (60 ^{o}C , 85^{o}C and N_2 atmosphere). By using a combination of buffer layer engineering, impedance spectroscopy and other characterization techniques, this Thesis confirmed that the interaction of the perovskite active layer with the top Al metal electrode through diffusion mechanisms is the major thermal degradation pathway for planar inverted perovskite photovoltaics (PVs) under 85^{o}C heat conditions. This Thesis has shown that by using thick solution processed fullerene buffer layer the perovskite active layer can be isolated from the top metal electrode and improve the lifetime performance of the inverted perovskite photovoltaics at 85 ^{o}C, to a detriment in solar cell device efficiency, however.

Furthermore, solution processed γ-Fe_2O_3 nanoparticles via solvothermal colloidal synthesis in conjunction with ligand-exchange method are used for interface top electrode modification in inverted (p-i-n) perovskite solar cells. In comparison to more conventional top electrodes such as $PC_{70}BM$/Al and $PC_{70}BM$/AZO/Al, this Thesis shows that incorporation of a γ-Fe_2O_3 provides an alternative solution processed top electrode ($PC_{70}BM/Fe_2O_3$/Al) that not only results in comparable power conversion efficiencies, but also improved thermal stability of inverted perovskite photovoltaics. The origin of improved thermal stability is attributed to a better γ-Fe_2O_3 interface with the top metal contact. The reduced charge trapped density of γ-Fe_2O_3/Al based interface improve the stability of inverted perovskite solar cells under accelerated heat lifetime conditions.

Following the above initial study of fullerene-based diffusion blocking layers, the usage of n-type doping is further explored to improve the PCE of p-i-n- inverted PSCs based on thick fullerene diffusion blocking layers while still retaining high thermal stability. The main issue that was identified in the previous work was the low conductivity of $PC_{70}BM$ which significantly limits the thickness of the films that can be used to achieve good thermal stability. In this work it is shown that utilizing N-DMBI as the n-type dopant for $PC_{70}BM$ and applying the just enough doping principle we can increase the PCE of inverted PSCs with thick (200 nm) $PC_{70}BM$ diffusion blocking layer from 7.84 to 13.1 % via doping with 0.3 % w.t. N-DMBI. Doping with N-DMBI significantly increases the conductivity of $PC_{70}BM$ and reduces the series resistance (R_S) of inverted p-i-n PSCs. Importantly, just enough N-DMBI doped thick $PC_{70}BM$ based devices retain a high thermal stability at 60 ^{o}C of up to 1000 h without sacrificing their photovoltaic (PV) parameters and PCE.

Finally, the hysteresis and stability issue that inverted PSCs using Cu:NiOx often exhibit is tackled. It has been reported that PSCs using Cu:NiO_X as hole transporting layer (HTL) often exhibit stability issues and in some cases J/V hysteresis. A β-alanine surface treatment process on Cu:NiOx HTL that provides J/V hysteresis-free, highly efficient, and thermally stable inverted PSCs is developed. The improved device performance due to β-alanine-treated Cu:NiOx HTL is attributed to the formation of intimate Cu:NiOx/perovskite interface and reduced charge trap density in the bulk perovskite active layer. The β-alanine surface treatment process on Cu:NiOx HTL eliminates major thermal degradation mechanisms, providing improved lifetime and performance under accelerated heat lifetime conditions. By using the proposed surface treatment, optimized devices with high PCE (up to 15.51 %) and up to 1000h lifetime under accelerated heat lifetime conditions (60 ^{o}C, N_2) are presented.

Keywords: Perovskite Photovoltaics, thermal stability, impedance spectroscopy, interfaces, electrodes, p-i-n (inverted) device structure hybrid Perovskite Solar Cells.

TABLE OF CONTENTS

LIST OF TABLES

LIST OF FIGURES

LIST OF ABBREVIATIONS

CUT	Cyprus University of Technology
MEP	Molecular Electronics and Photonics
PV	Photovoltaic
E_c	Conduction band
E_v	Valence band
E_f	Fermi level
E_g	Bandgap
Si	Silicon
AM	Air mass
NREL	National Renewable Energy Laboratory
MOSFET	Metal oxide semiconductor field effect transistor
GaAs	Gallium Arsenide
CIGS	Copper Indium Gallium Selenide
CdTe	Cadmium Telluride
OPV	Organic Photovoltaic
DSC	Dye sensitized solar cell
PSC	Perovskite solar cell
MAPI	Methylammonium lead iodide
TCO	Transparent conductive oxide
FTO	Fluorene Tin Oxide
ITO	Indium Tin Oxide
ETL	Electron Transporting layer
HTL	Hole Transporting Layer
MA	Methylammonium

FA	Formamidinium
Cs	Cesium
$CaTiO_3$	Calcium Titanate
Pb	Lead
I	Iodide
Br	Bromide
Cl	Chloride
Al	Aluminium
Cu	Copper
Ag	Silver
Au	Gold
Cr	Chromium
HOMO	Highest Occupied Molecular Orbital
LUMO	Lowest Unoccupied Molecular Orbital
V_{oc}	Open Circuit Voltage
J_{sc}	Short Circuit Current
FF	Fill Factor
PCE	Power Conversion Efficiency
HI	Hydrogen iodide
PbI_2	Lead iodide
ISOS	International Summit on Organic Photovoltaics Stability
CuSCN	Copper thyocynate
Ta-WOx	Tantalum doped tungsten oxide
Spiro-MeOTAD	2,2',7,7'-Tetrakis[N,N-di(4-methoxyphenyl)amino]-9,9'-spirobifluorene

PCBM	[6,6]-phenyl-C_{61}-butyric acid methyl ester
PEDOT:PSS	poly(3,4-ethylenedioxythiophene) polystyrene sulfonate
Sn	Tin
SCN	Thiocynate
PEA	Phenylethylammonium
BA	Butylammonium
Li-TFSi	lithium bis(trifluoromethanesulfonyl)imide
TTF-1	tetrathiafulvalene
P3HT	Poly(3-hexylthiophene-2,5-diyl)
PTAA	Polytriarylamine
SWNT	Single well nanotube
RGO	Reduced graphene oxide
Sb_2S_3	Antimony sulfide
DMSO	Dimethyl sulfoxide
GBL	γ-butyrolactone
MAI	Methylammonium iodide
NP	Nanoparticle
R_S	Series resistance
R_{SH}	Shunt resistance
ECM	Equivalent circuit model
BP	Benzophenone
N-DMBI	4-(2, 3-Dihydro-1, 3-dimethyl-1*H*-benzimidazol-2-yl)-*N*, *N*-dimethylbenzenamine (N-DMBI)
BCP	Bathocuproine

1 INTRODUCTORY REMARKS

1.1 Research motivation

The increasing worldwide energy consumption has led to the rise of photovoltaic technology over the years, spanning over several generations of solar cells. Although several advancements and breakthroughs have been made to Si-based photovoltaics, the high cost as well as complex fabrication has led researchers to expand the scope of photovoltaics beyond Si and search for new materials. One of the most novel and attractive research fields over the last years have been Perovskite solar cells. Combining the advantages offered by solution processed techniques such as low fabrication cost and flexibility with high efficiencies, Perovskite solar cells have proven to be a strong candidate with high potential as a replacement for Si technology. However complex device physics, toxicity and intrinsic instability has hindered the advancement of this photovoltaic technology towards commercialization. Motivated by the enormous potential as well as plethora of problems that wait to be resolved, this work is dedicated towards the understanding of physics as well as improving the overall performance of Perovskite solar cells by implementation of novel electrodes for the devices.

1.2 Research objectives

The main objective of this work is to enhance the performance of Perovskite solar cell via the implementation of novel electrodes. Therefore, the main experimental part of this work was conducted by following the next two objectives:

Objective 1

Stability was reported in the literature to be one of the main hindrances of Perovskite solar cells towards commercialization. The intrinsic stability of the Perovskite crystal has proven to be poor in a variety of environmental conditions such as heat. The focus of this objective is to understand the major degradation pathway of perovskite solar cells under accelerated heat conditions and inert atmosphere as well as to tackle it by tuning the existing structure of a reference device.

Objective 2

The second objective is a natural continuation of the first objective. In detail, after identifying the major degradation pathway of Perovskite solar cell under accelerated heat conditions, electrode engineering should be performed to introduce novel ideas in the existing device structure to improve the overall performance of the devices. The new electrodes should have appropriate properties as to not compromise the overall efficiency of the device to a large degree while simultaneously offering improvements towards the stability of the device, effectively striking a good balance between efficiency and stability

1.3 Research methodology

The overall basis of this research is focused on purely experimental work through the fabrication of Perovskite solar cells in the MEP laboratory using solution processed techniques. The research was initially conducted using a pre-existing reference device of the general structure ITO/PEDOT:PSS/$CH_3NH_3PbI_3$/$PC_{70}BM$/AZO/Al which was developed in house and has proven to be a reliable baseline for comparisons. Tuning of the reference was conducted and studied using a variety of deposition and characterization techniques to achieve PSCs with a good balance between efficiency and stability under accelerated heat lifetime conditions under inert atmosphere.

2 THEORETICAL FRAMEWORK

2.1 Solar energy and photovoltaics

2.1.1 The rise of solar energy

Without a doubt oil and fossil fuels have revolutionized the way humanity has covered its energy needs over the centuries. With a plethora of applications and energy needs coverage such as transportation and heating, oil and fossil fuels have been the predominant means for covering our energy needs over the years. Although the advantages seemed to be many, the repercussions are also severe and are shown to worsen every year. Fossil fuels are a finite source of energy on earth and its rabid consumption over the centuries has rendered their supplies dangerously low over the last years as it can be seen in Figure 2-1.

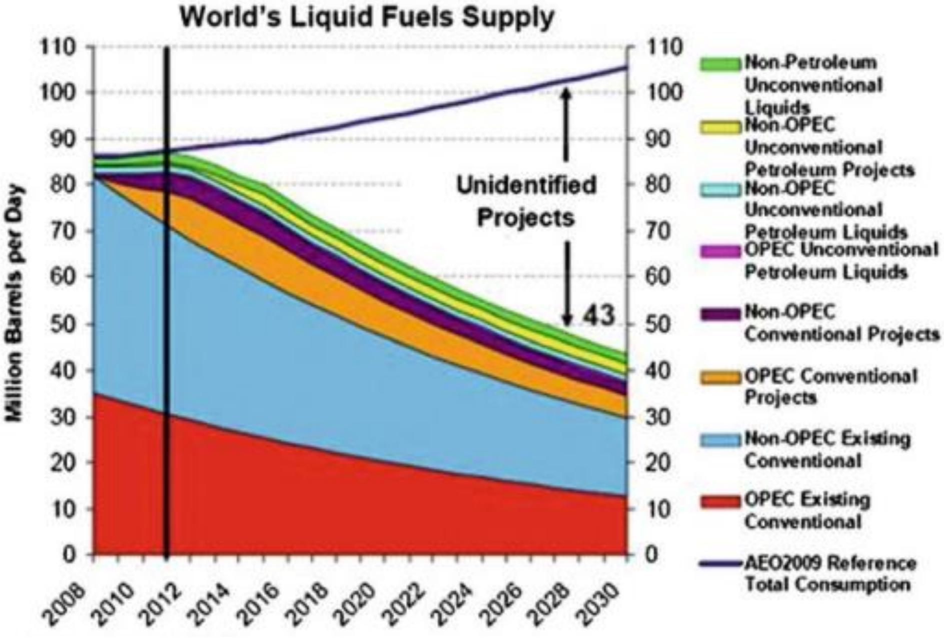

Figure 2-1: World's liquid fuel supply projection[1]

The thinning of the supply of fossil fuels has caused problems to surface. The most obvious problem is the rising of oil and natural gas prices due to the high demand and lower supply. This issue is made even worse due to morality issues such as war in countries with high oil supplies, particularly in the Middle East.

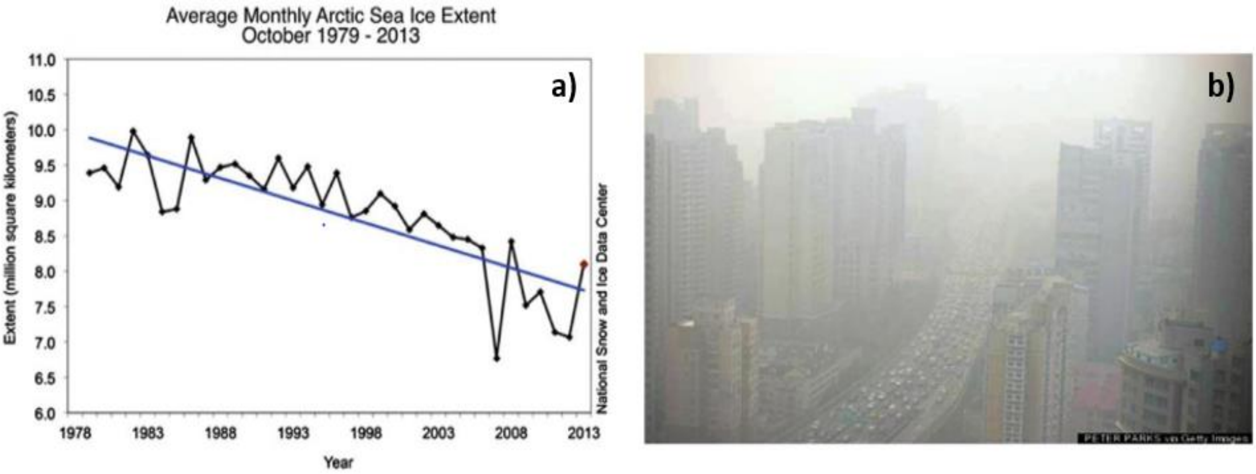

Figure 2-2: a) Extent of arctic ice meltdown, b) Photo of Shanghai in 2013. [1]

Another major issue that rose from the fossil fuels and oil is the heavy taxing these energy sources have caused to the planet. Atmospheric pollution that led to the green-house effect has caused the Earth’s temperature to rise continuously over the last years, which led to the melting of arctic ice (Figure 2-2a) thus endangering several ecosystems. Furthermore, atmospheric pollution has been so severe in several cities (Figure 2-2b) that will undoubtedly have huge impacts in human health. Due to the issues previously mentioned, research has been pushed towards the field of green energy. In its broader context, green energy refers to the utilization of energy from renewable energy sources such as wind power, solar energy, hydropower, geothermal energy and bioenergy.

Amongst the renewable energy sources previously mentioned, solar energy has been the most popular. The sun is estimated to supply the Earth with 167 000 TW of power every day. A percentage is lost by reflection back to space while another portion is absorbed by the oceans to stabilize the ecosystem. On average, the usual energy consumption each day is estimated to be ~ 20 TW. [2] As it can be seen, theoretically the sun provides more than enough power to cover the average energy needs of humans each day.

Harvesting of solar energy and the concept of photovoltaics has been a main goal of scientists and can be historically traced back to two centuries ago. The origin of the photovoltaic effect was first discovered by Becquerel in 1840 by placing silver chloride in an acidic solution, which upon illumination produced voltage through the connected platinum electrodes.[3] The increase in conductivity of selenium was observed in 1873 by the electrical engineer Willoubhy Smith and the flow of electricity upon illumination was later proved by the British scientists William Grylls Adams and Richard Evans Day. [3] The first working photovoltaic cell was developed by Charles Fritts in 1883 by incorporating selenium in between an iron plate and a semi-transparent gold electrode. Fritts was also the first to connect several selenium modules together to make the very first photovoltaic array. In 1922 Einstein was awarded a Nobel prize which among others was dedicated to his discovery of the law of photoelectric effect. A breakthrough was the discovery of the basis of modern solar cells, which is the P-N junction, in 1946 by Russel Shoemaker Ohl. Drawing from the p-n junction theory, Daryl Chapin, Calvin Fuller and Gerald Pearson, scientists working for the Bell Laboratories have fabricated a functioning solar cell with 6% efficiency in 1954 paving the way for a new era of modern technology and energy harvesting.

2.1.2 Conventional photovoltaic physics

As previously mentioned, the most basic form of a solar cell is based on a P-N-junction. To understand the principles behind the operation of conventional solar cells, some basic concepts of semiconductor physics should be introduced. In a semiconductor, the valence band (E_v) is defined as the highest energy level occupied by electrons, conduction band (E_c) is the lowest energy level not occupied by electrons and the band gap (E_g) is the energy difference between E_c and E_v, or in other words the energy needed for an electron to get excited from E_v to E_c.

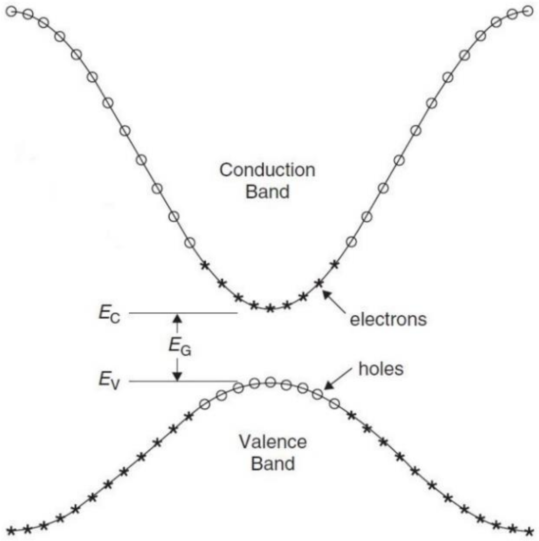

Figure 2-3: Energy band diagram of a semiconductor [4]

A particularly important concept of semiconductors is also the Fermi level (E_f), which is defined as the ratio of filled energy states with electrons compared to the available energy states. In general, energy states below E_f are filled with electrons. In intrinsic (undoped) semiconductors the number of electrons in E_c and holes in E_v are equal and E_f lies in the middle of E_g. To form a p-n junction, we first must have two doped semiconductors, n-type and p-type. In the case of Si, n-type doping is usually achieved by introducing impurities, such as phosphorus that function as electron donors, and therefore introduce electrons to E_c. Subsequently, E_f shifts towards E_c. The opposite happens when we introduce impurities that function as electron acceptors, such as boron. Electrons are extracted from E_v, thus introducing excess holes, resulting in p-type doping. A p-n junction is formed when an n-type semiconductor and a p-type semiconductor come in contact as shown in Figure 2-4.

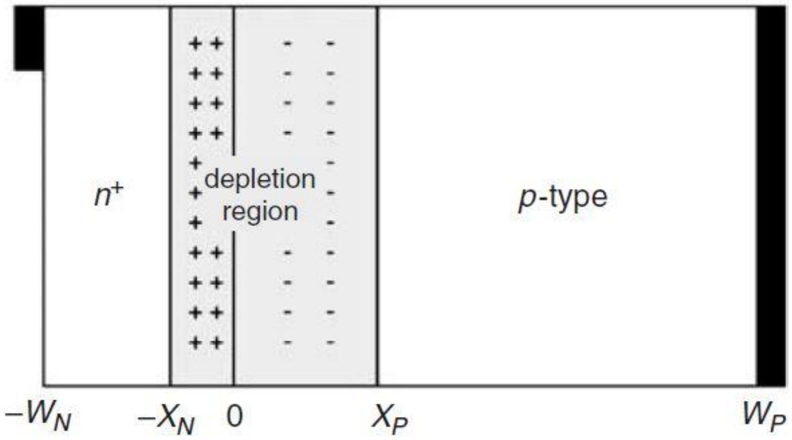

Figure 2-4: Schematic of a p-n junction depicting the depletion region.[4]

At equilibrium, E_f for both n-type and p-type semiconductors are aligned. Since we introduce a region with excess electrons via the n-type semiconductors and a region with excess holes via the p-type semiconductor, carrier movement is firstly governed by diffusion. In detail, electrons diffuse from the n-type region towards the p-type region and holes diffuse from the p-type region towards the n-type region. As a result, positive charge starts to build towards the n-type region and negative charge builds towards the p-type region, which forms an electric field with direction towards the positive charge that started to build in the n-type region. This electric field causes electron drift in the opposite direction of the field (from the p-type region to the n-type region) and holes drift from the n-type region towards the p-type region. At thermal equilibrium, the diffusion and drift of carriers balance each other, effectively forming the depletion region, which is completely depleted of holes and electrons and is the transition region between n-type and p-type regions. The electric field of the junction arising from the exposed positive and negative charges results in an electrostatic potential difference called the built-in voltage (V_{bi}).

Sun has a surface temperature of ~5762K and it can be approximated as a radiating black body. Photons that have sufficient energy greater than Eg can generate an electron-hole pair. The radiation intensity that hits the Earth's atmosphere is 1.353 kW/m^2. [5] The spectral distribution is known as the air mass zero (AM0) radiation spectrum and the air mass number is given by Equation (1) where θ is the angle of incidence. A widely used standard is AM1.5 with $\theta=48.2^o$ [5]

$$AM=1/\cos(\theta)$$

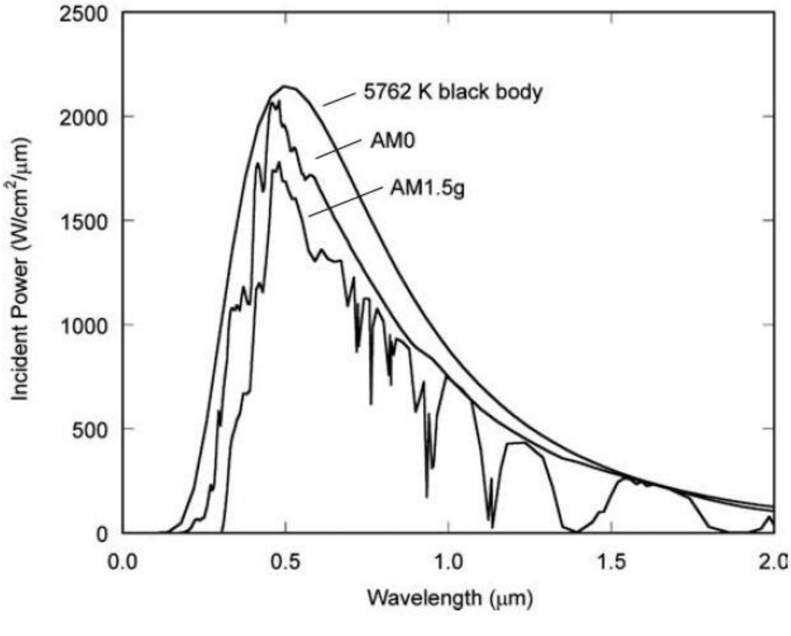

Figure 2-5: Radiation spectrum of a black body at 5780K in AM0 and AM1.5. [4]

When photons have sufficient energy (greater than E_g). Electrons can be excited from E_v to E_c. The photo-generated carriers (electrons and holes) are swept by the built-in electric field of the p-n- junction and can now move across the junction. By connecting an external load, the photo-generated carriers can be collected and utilized for power. This process is shown in Figure 2-6.

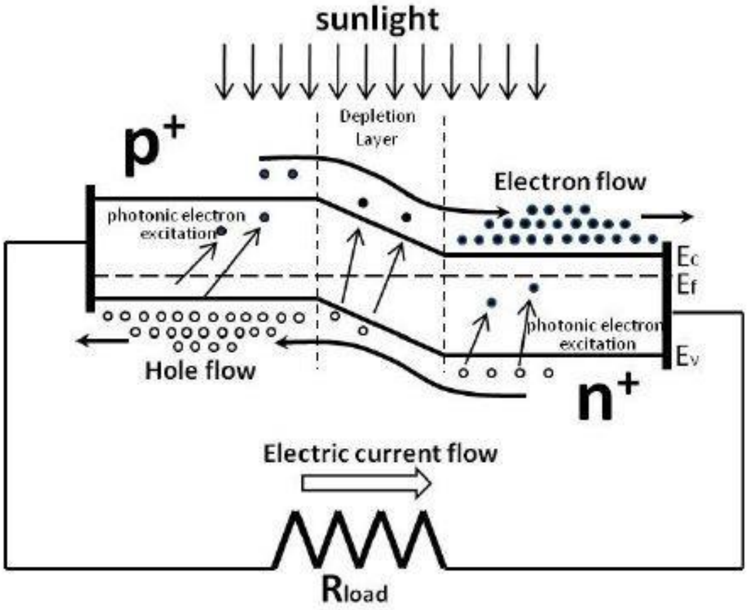

Figure 2-6: Working principle of a simple p-n junction solar cell [6]

2.1.3 Photovoltaic technologies

The photovoltaic technology has undergone tremendous advancements over the years incorporating different structures, each with its own achievements and challenges. A roadmap of the technology so far alongside the efficiencies achieved by each PV technology are shown in the chart in Figure 2-7 which was adopted by the National Renewable Energy Laboratory (NREL).[7]

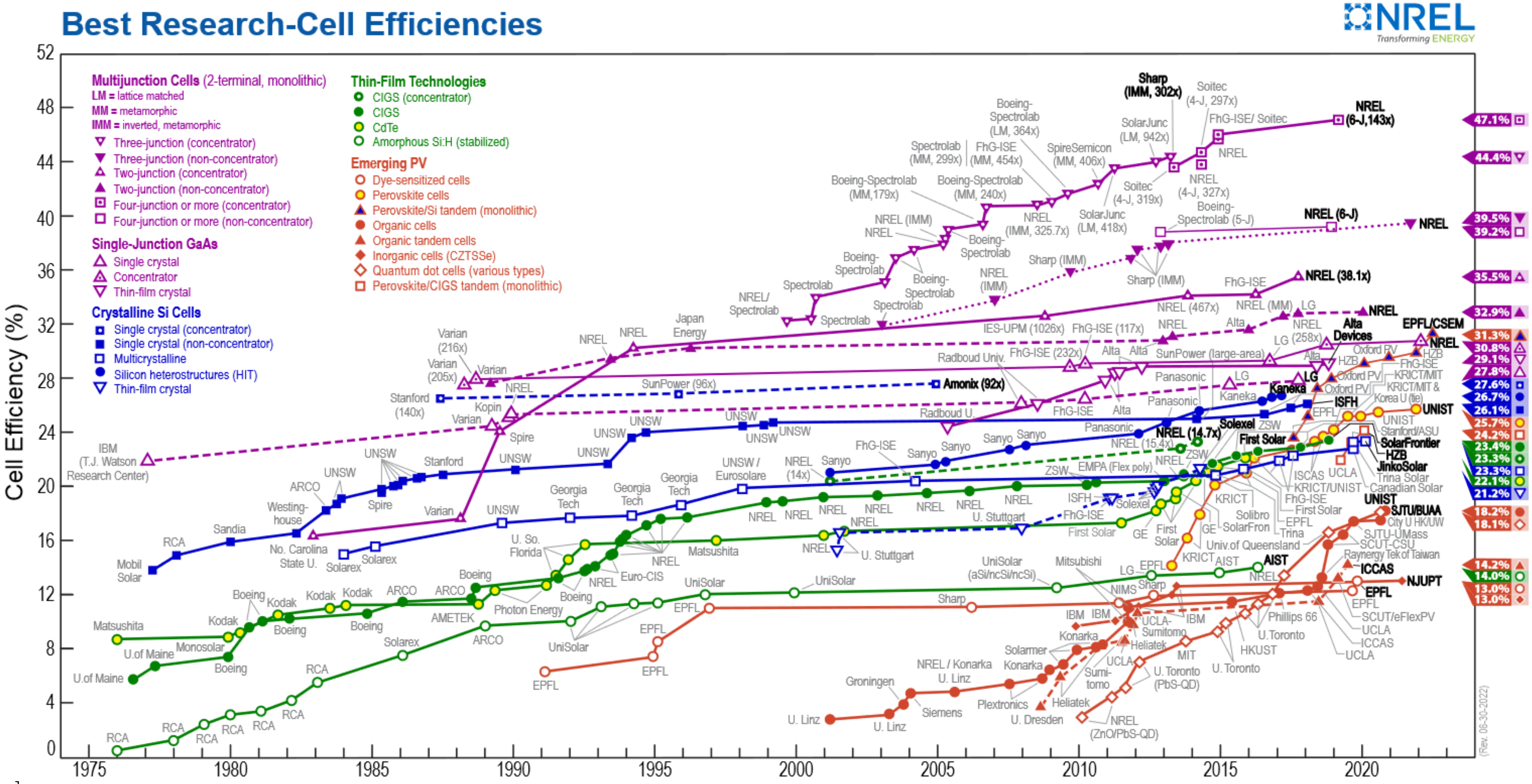

Figure 2-7: Illustration of various PV technologies and efficiencies adapted by National Renewable Energy Laboratory (NREL)

The

first generation involves thick crystalline Si films. This is no surprise since Si offers tremendous advantages such as very high abundance in the Earth [8], non-toxic nature and huge compatibility in a variety of industries such as integrated circuits, transistors, MOSFETs etc. [9] Monocrystalline silicon based films are cut from Si ingots that are grown from small monocrystalline seeds. They have achieved high efficiencies in the order of 24.4 %, they require however Si of very high purity and often high temperature fabrication techniques.[10] In order to combat this issue, polycrystalline silicon films were fabricated by random orientation of small Si crystals. Although the energy consumption of the fabrication methods was not as high, the efficiency is also lower at 19.9%. [11] GaAs is also a strong candidate of this generation due to its wide potential of design option and superior control over the generation and collection of electrons and holes, with efficiencies ranging from 18.4-28.8 %. [11]

In the second generation, the technology was focused on thin films with the aim to reduce the high fabrication costs of the first generation with a compromise to reduced quality and efficiency of cells. Noteworthy is amorphous silicon, although the absence of the crystalline structure hinders the lifetime of such devices.[12] Furthermore Coper indium gallium selenide (CIGS) and cadmium telluride (CdTe) cells have achieved efficiencies of 22.3 %[13] and 21 %[11] respectively.

The third generation is based on the idea of exceeding the Schockley-Queisser limit[14] and fabricate cells that are often based on organic components, thus utilizing solution-processed techniques, effectively reducing the fabrication costs even further as well as providing mechanical flexibility to the cells. Several technologies have already been incorporated, including dye sensitized solar cells (DSCs), organic photovoltaics (OPVs), quantum dot solar cells and perovskite solar cells (PSCs). Multi junction tandem cells are also included in this generation, utilizing semiconductors with different band gaps.

The fourth generation of PVs consists of novel ideas such as 2D graphene and its derivatives and carbon nanotubes. It combines the solution processed techniques of the third generation with nanomaterials to improve the charge dissociation and transport. [10]

2.2 Hybrid organic-inorganic Perovskite solar cells

2.2.1 Crystal structure

Organic-inorganic perovskite solar cells have been the center of attention for PV technologies over the last years. As previously mentioned, they belong in the family of 3rd generation of solar cells. Their name was originated from the mineral $CaTiO_3$ which was discovered in 1839 and is named after Count Lev Alekseevich Perovski. [15] The mineral forms a crystal structure consisting of TiO_6 octahedral, with the Ca occupying the central cavity of a single cell. Similar to the mineral, organic-inorganic perovskites adopt a very similar crystal structure which can be summarized by the formula ABX_3 where A is the organic cation, B is the metal ion and X is the halogen atom. A conventional perovskite structure would consist of the organic methylammonium cation CH_3NH^+ (MA), the metal element Pb^2 and the halogen I^-, which would form a perovskite with the formula, $CH_3NH_3PbI_3$, known as methylammonium lead iodide (MAPI). [16] Similar to the crystal structure of the mineral $CaTiO_3$, the crystal structure of MAPI adopts a crystal structure with BX_6 octahedral with A located in the cavity between 4 BX_6 as shown in Figure 2-8.

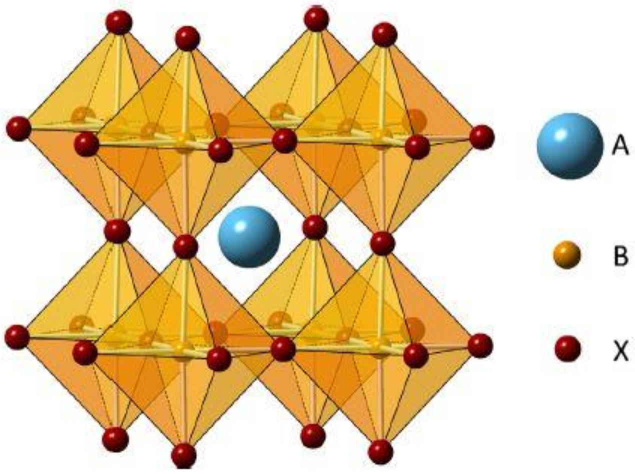

Figure 2-8: Representation of the perovskite crystal structure [17]

The crystal structure of the perovskite can be modified by introducing different ions with various ionic radii in the position of A, B or X which can severely affect the properties and stability of the perovskite crystal structure. The stability and distortion of the crystal structure can be described by taking into consideration the tolerance factor "t" which is calculated using equation (2), where R_a, R_b and R_x are the ionic radii of the corresponding ions.

$$t = (R_a+R_x)/\sqrt{2}\,(R_b+R_x) \quad (2)$$

Depending on the value of "t," the perovskite can exist in three different crystal phases: cubic, tetragonal and orthorhombic, as shown in Figure 2-9.

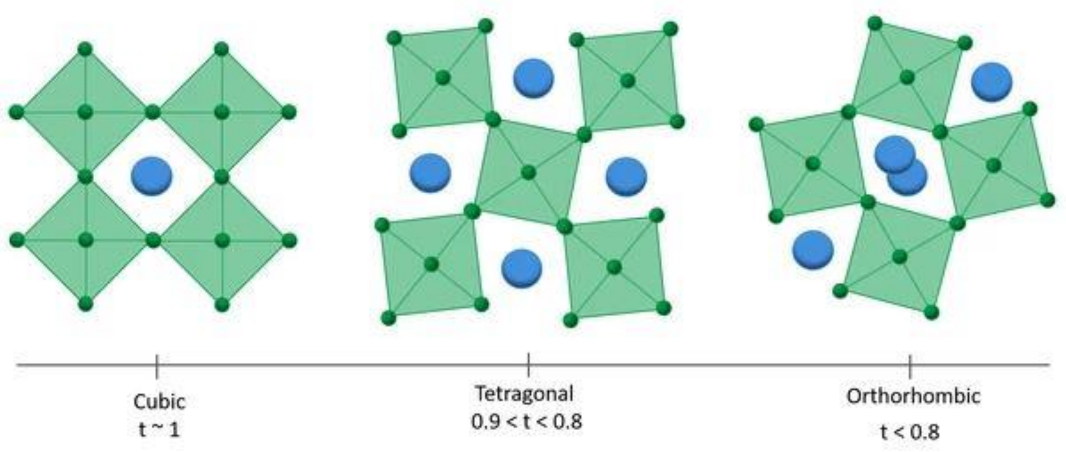

Figure 2-9: Perovskite crystal phases in regards to the tolerance factor. [18]

The first crystal phase that can exist in a perovskite crystal is the orthorhombic phase up to a temperature of T<165 K. [19] When the temperature exceeds 165 K, the cations are no longer in a fixed position and the crystal phase shifts towards the tetragonal orientation, which can be maintained in a temperature range of 165 K<T<327K. When T>327 K the crystal orientation shifts towards the most stable and usually favorable cubic phase. [20]

2.2.2 Working principles

Perovskite-based absorbers have been initially used as sensitizers for mesoporous TiO_2 in Dye sensitized solar cells, exhibiting a poor efficiency of 3.8% and stability due to the rapid degradation of MAPI from the liquid electrolyte. [21] The first properly functional solid state perovskite-based solar cell (PSC) utilizing an organic HTL and mesoporous architecture, which is later discussed in this report, exhibited an efficiency of 10.9 % as well as improved stability. [22] Although PSCs can be fabricated based on different architectures, which are later discussed in this report, they all share the same fundamental working principles and attributes that sets them apart from other PV technologies.

In its simplest form, PSC-based devices are fabricated using solution-processed techniques and incorporate a transparent conductive oxide (TCO), which is usually FTO or ITO, the metal electrode, the active layer absorber and the two charge selective contacts (HTL and ETL) as shown in Figure 2-10.

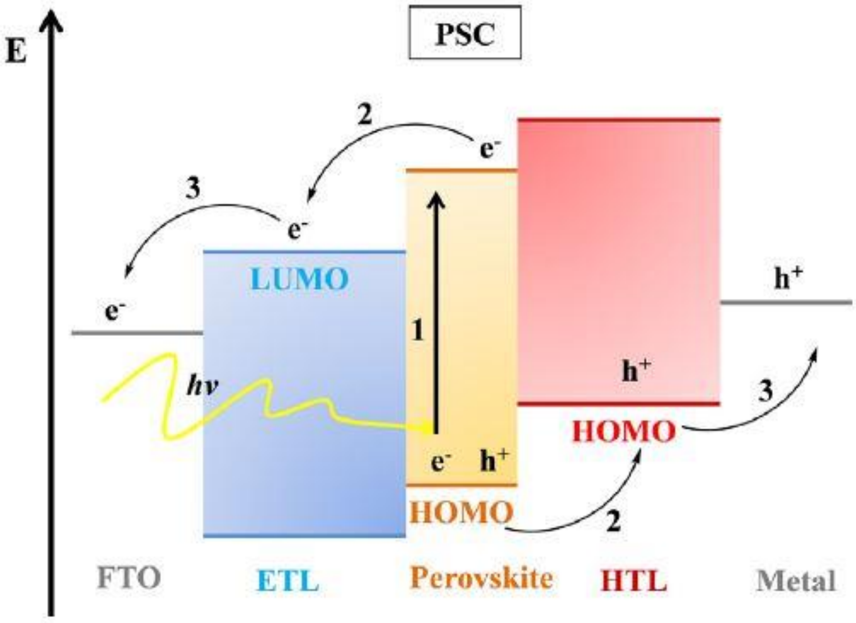

Figure 2-10: Energy level diagram showing charge generation and collection in PSCs [17]

As it can be seen form Figure 2-10, the perovskite active layer lies in between the ETL and HTL. When a photon has energy higher than E_g of the perovskite active layer, an electron-hole pair is formed, like the physics of conventional PVs. The electron is excited from the HOMO to the LUMO of the perovskite, leaving a free hole to the HOMO of the perovskite. As previously mentioned, the active layer is “sandwiched” between the ETL and HTL. The ETL is responsible for the efficient collection of electrons while the HTL for the efficient collection of holes. To have efficient collection of carriers in general, a layer should energetically favor the passage of a certain carrier type while simultaneously blocking the opposite carrier type. This is achieved by correct choice of layers in terms of type (n-type for ETL and p-type for HTL) while also having compatible energy levels or work functions with the HOMO and LUMO of the perovskite active layer. The performance of the PSC can be tuned by combining several materials when forming the ETL and HTL.

The hybrid organic-inorganic nature of PSCs gives a unique nature to this PV technology with its own set of advantages and disadvantages. Only Pb and the halogen ions contribute to the HOMO and LUMO of the active layer, while the organic cation only contributes to the crystal structure.[17] Thus by changing these ions, we have a high amount of tenability for the Eg of the active layer as well as the stability of the device.[23] In the case of the conventional MAPI, Eg=1.55 eV. MAPI also exhibits a large absorption coefficient in the visible range ($\sim 10^5$ cm^{-1}) [24] which ensures a generation of large number of photo-excited carriers even when using small thickness for the perovskite active layer. [25] A very attractive attribute of PSCs is the low exciton binding energy, in the range of a few meV [26] [27] which effectively ensures the formation of free charges while practically bypassing the exciton state, which is the bound state of an electron and a hole with electrostatic Coulomb forces, which leads to the high efficiencies reported for PSCs. Furthermore, the charge mobilities are remarkably high (8 $cm^2V^{-1}S^{-1}$) considering the solution processed nature of the materials used. The high charge mobility and low bimolecular recombination exhibited leads to charge diffusion lengths that can exceed 1μm. [28] Even though PSCs exhibit tremendous advantages they also suffer from sever drawbacks that set them back from commercialization. The biggest issue with PSCs is the poor stability under environmental conditions, especially humidity, which can distort the crystal structure and alter the photoactive properties of the devices. This concept is discussed in detail later in this report. Furthermore, in all the basic structures, metallic Pb is present in the crystal, which renders PSCs unsuited for commercialization due to its toxic nature. It is also worth mentioning that the fabrication conditions of PSCs are challenging to be controlled properly, which leads to poor reproducibility of devices.

2.2.3 Device structures

PSCs are usually fabricated following two common structures: a) mesoporous, b) planar. Two subsequent categories that can be adopted are normal and inverted structures depending on the position of the ETL and HTL accordingly (see Figure 2-11).

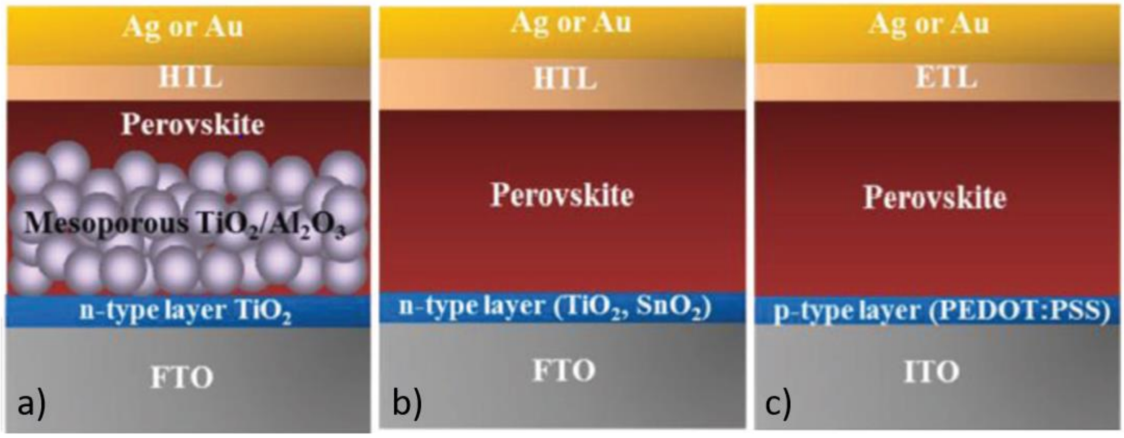

Figure 2-11: Perovskite solar cells architectures showing a) Mesoporous, b) planar normal, c) planar inverted structure.[16]

Mesoporous structures initially follow the conventional PSC device architecture, thus consisting of a TCO (FTO/ITO) and a compact ETL (usually TiO_2). The most interesting concept of this structure lies on the absorber, where a mesoporous oxide layer (TiO_2/Al_2O_3) lies between the ETL and HTL. This allows the perovskite crystals to adhere into the mesoporous oxide. The structure is followed by the HTL (usually spiro-MeOTAD), and metal electrode as described previously. Through the adhesion process of the perovskite crystals into the mesoporous oxide layer increased surface area is achieved for photo generation [29], thus favoring the PCE of the devices. The pore filling effect highly affects the performance of the device. [30] Although the incorporation of the mesoporous oxide layer allows PSC devices to achieve high PCEs with minimal hysteresis in the J/V plot, it also renders the deposition of the active layer relatively challenging. [31]

Compared to mesoporous structures, planar structures offer a much simpler structure, with the active layer being enclosed between the ETL an HTL forming two different interfaces accordingly. The simple architecture employed renders planar PSCs a more appropriate candidate for commercialization compared to mesoporous structures by providing compatibility with tandem technologies and large scale fabrication processes. [16] Planar perovskite solar cells can be divided into normal n-i-p structure, where the ETL lies on the bottom of the device and the HTL on top (Figure 2-11b) and inverted p-i-n structure where the HTL lies on the bottom of the device and the ETL on top (Figure 2-11c). Similar to mesoporous structures, n-i-p planar structures use the conventional TiO_2 as the ETL and spiro-MeOTAD as the HTL. Although planar n-i-p structures offer improvements in V_{oc} and J_{sc}, compared to mesoscopic structures, they also exhibit more severe hysteresis effects.[16] A hysteresis effect in PSCs is a serious issue exhibited by this technology and is closely related to the ionic-electronic conduction PSCs as well as dynamic trapping-detrapping of charges.[25] As we have previously introduced, halogen ions are usually present in the perovskite crystal. These halogens ions are quite mobile and can easily diffuse primarily across the grain boundaries of the perovskite. One of the most mobile ions is I^- due to its small activation energy (~0.29 eV), high concentration gradient (10^{15} cm^{-4}) and fast diffusion coefficient ($3.1x10^{-9}$ cm^2s^{-1}). [32] The diffusion of mobile ions is not only responsible for the hysteresis effects of PSCs but also a crucial factor contributing towards the poor stability. Inverted p-i-n structures usually utilize PEDOT:PSS as the HTL , although it has been recently replaced with inorganic layers that will be later discussed, and $PC_{60}BM$ as the ETL. It is worth noting that fullerene derivatives such as PC[60]BM not only serve as an ETL for p-i-n structures, but they also passivate the grain boundaries of PSCs, effectively improving the overall performance of the device. [33] Inverted p-i-n structures offer high PCE, flexibility, low temperature processing and negligible hysteresis effects.[16] Between the different architectures the highest certified PCE is achieved using a normal structure with a PCE of 25.5 %.[34] while recently tandem architectures with Si have reached certified PCE of 31.25%.[35]

2.2.4 Instability mechanisms

As previously mentioned in this report one of the major drawbacks in commercialization of PSCs is the poor stability that usually the devices exhibit. PSCs can rapidly degrade under environmental conditions such as humidity, light and heat. The inherent instability to moisture of the perovskite is particularly problematic since it can destroy the crystal structure and severely affect the device performance. The degradation mechanisms under moisture exposure of the conventional MAPI can be described by the following equations, which were adopted by Wang et. al.[36]

$$CH_3NH_3PbI_3\ (s) \longleftrightarrow PbI_2\ (s) + CH_3NH_3I\ (aq) \quad (3)$$

$$CH_3NH_3I\ (aq) \longleftrightarrow CH_3NH_2\ (aq) + HI\ (aq) \quad (4)$$

$$4HI\ (aq) + O_2\ (g) \longleftrightarrow 2I_2\ (s) + 2H_2O\ (I) \quad (5)$$

$$2HI\ (aq) \longleftrightarrow H_2\ (g) + I_2\ (s) \quad (6)$$

The hygroscopic nature of MA [37] causes the MAPI crystal structure to readily absorb water. The hydrogen bonds between organic and inorganic components of the perovskite crystal is therefore severely affected [38] and can cause the crystal structure to deteriorate. The first stage of decomposition is described by equation (3), where the loss of MA cation causes the crystal structure of MAPI to fail, resulting in the formation of PbI_2 and CH_3NH_3I. The formation of PbI_2 is very apparent from the color change of the perovskite film from shiny black to yellow. CH_3NH_3I can further decompose to CH_3NH_2 and HI described by equation (4). HI can either follow the reaction in equation (5) and react with oxygen, thus forming water that further promotes the decomposition of the perovskite crystal or the reaction in equation (6). [39] Improvement towards the humidity stability of PSCs has been reported through various methods such as incorporation of buffer layers or modification of the perovskite active layer that will be later discussed in this report. Shielding the perovskite active layer from humidity, and therefore, improvement in device lifetime has been reported through the usage of hydrophobic layers such as thiols [40] and inorganic bilayers like cerium oxide (CeOx)[41]. Recently a study has suggested that using long chain alkylammonium cation based 2D perovskites as an encapsulation method for 3D perovskite can substantially improve the moisture stability with the degradation starting a couple of minutes after the films were submerged in water for 5 minutes. [42]

The instability of PSCs under light exposure is only prevalent in the presence of atmospheric oxygen. The equations describing the degradation mechanism were adopted from Aristidou et. al.[43]

$$CH_3NH_3PbI_3 + \text{Light} \longrightarrow CH_3NH_3PbI_3{}^{*} \qquad (7)$$

$$CH_3NH_3PbI_3{}^{*} + O_2 \longrightarrow O_2^{-} \qquad (8)$$

$$CH_3NH_3PbI_3 + O_2^{-} \longrightarrow CH_3NH_2 + PbI_2 + ½I_2 + H_2O \; (9)$$

As indicated in equation (7) the perovskite undergoes a photo-excited state upon illumination, causing photo-generated electrons to occur. The photo-generated electrons can react with atmospheric oxygen to form superoxide (O_2^-) as shown in equation (8). O_2^- can in turn deprotonate the MA cation by reacting with the free H^+ of the cation. This has as a result the decomposition of the perovskite crystal, and formation of PbI_2 shown in equation (9). [44] Furthermore, TiO_2 that is often used in normal structures is inherently unstable to UV due to desorption of oxygen from the oxygen vacancies of TiO_2 induced by photo-generated holes. This has as a result the unoccupied deep surface traps that contribute to the instability of PSCs. [45] Several ideas have been proposed to improve the light stability of PSCs such as replacing the MA with a less acidic cation [46] such as formamidinium (FA). Replacing TiO_2 with other HTLs such as CuSCN [47] and Ta-WOx[36].

As previously stated in this report, temperature can have a significant effect on the perovskite crystal orientation and stability. It was reported that even at N_2 atmospheres the perovskite layer can decompose to PbI_2, with the atmosphere severely affecting the decomposition rate (ambient atmosphere being the most affecting). [48] The decomposition mechanism to PbI_2 is shown in equation (10), adopted by Wang et. al. [36]

$$CH_3NH_3PbI_3 + \text{heat} \longrightarrow Ch_3NH_2 + PbI_2 + HI \; (10)$$

Several attempts have been made to push improve the thermal stability of PSCs, however the research in this area is still quite scarce. By replacing the MA cation with FA the tolerance factor τ was closer to unity, thus giving the perovskite improved chemical stability under accelerated temperatures. [49] Furthermore, the commonly used spiro-

MeOTAD has been reported exhibits a state change at elevated temperatures, which reduces the hole mobility. These issues can be tackled by using the thermally stable NiO and PCBM materials as the HTL and ETL, respectively. [50] It was also reported that the perovskite active layer was damaged by the metal electrode interaction. It was inferred that temperatures as low as 70 °C can cause Au metal migration towards the active layer. The migration of Au can be blocked by incorporating a Cr interlayer between the Au metal electrode and HTL layer as reported. [51] Recently the thermal stability of PSCs was improved via passivation of surface traps on the active layer using the Lewis base triphenylphosphine (TPP), retaining 70% of the initial PCE under 85°C and 10% humidity. [52]

As we have previously stated, PSCs are mixed electronic/ionic conductors. The low ionic activation energies stated before can cause severe problems towards the overall stability of the devices. The diffusion of ions and particularly I^- can also be accelerated by conditions such as heat, bias and illumination. The major diffusive pathway for ions has been the grain boundaries of the perovskite active layer where they can easily reach the top electrode of the device and eventually reach the metal electrode. This can cause severe repercussions to the device due to the reactivity of metals with halogens, thus altering the energetic properties of the device and affect the device performance.

2.2.5 Active layer engineering

As it was previously mentioned in this report, PSCs have a crystal structure which is highly modifiable. Considering the ABX_3 abbreviation, organic cation A, metallic atom B and halogen X can be interchanged with several elements to influence the tolerance factor τ and Eg of the device, thus affecting both the stability and PCE. In recent works the replacement of MA with FA has been studied. There are a couple of attractive features FA can offer as a replacement of MA. FA can form stronger hydrogen bonds with the PbI_6 octahedral[53] and is a larger cation with a size of 2.53 Å compared to MA which is 2.17 Å. The bigger size of the cation pushes the tolerance factor to a value of τ=0.99 compared to τ=0.91, which allows the perovskite crystal to adopt a more stable cubic structure [54] while also expanding the lattice[55] and changing the octahedral angle. [56] FA can effectively decrease E_g from 1.59 eV to 1.49 eV [49] when it replaces MA, which enables more efficient photo-generation of charges. Furthermore, incorporation of FA has shown to improve the thermal stability of PSCs [23] as well as stability under light due to the less acidic nature of FA. [57] Unfortunately moisture stability of FA is inferior to MA [58] due to the tendency of FA to shift into β-phase (yellow) from α-phase (black) even at room temperature as well as the tendency to decompose into ammonia. [59] In order to stabilize the black phase of FA, Cs was introduced into the crystal lattice. This has shown to improve both the humidity and thermal stability [60] of PSCs as well as under continuous illumination.[61] The current state of the art for A cation is achieved by incorporating triple cation (MA/FA/Cs) [62] and quadruple cation (MA/FA/Cs/Rb) formulations in order to combine the different advantages of each formulation, effectively achieving PCE~20 % and good overall stability. [31]

Apart from the A site cation, efforts were done to replace Pb from the B site with a less toxic alternative. So far lead-free PSCs were fabricated by replacing Pb with Sn. However due to the tendency of Sn^{2+} to be oxidized to the more stable Sn^{4+} [63] the stability of PSCs incorporating Sn is a lot inferior to the ones with Pb. [64 ,65].

The halogen X site of the perovskite ABX_3 crystal structure can also be modified to alter the overall performance of PSCs. Br^- and Cl^- have been incorporated to replace the more conventional I^- due to their smaller ionic radius. [66] The humidity stability of PSCs was shown to be improved from the incorporation of both Br^- and Cl^- due to the crystal shift from tetragonal to cubic phase. [54,67] Incorporation of Cl^- was also shown to improve the perovskite film crystallinity and coverage. [68] Chemical stability of the perovskite crystal was also was also achieved by the incorporation of pseudo-halogen ions such as SCN^-, which was reported to form strong hydrogen bonds with MA^+ and strong ionic interaction with Pb^{2+}, thus offering better humidity and thermal stability.[69]

A more novel approach towards the modification of the perovskite active layer is the concept of 2D perovskite. This is achieved by the insertion of large cations such as phenylethylammonium (PEA^+) and butilammonium (BA^+) into the perovskite crystal, as shown in Figure 2-12.

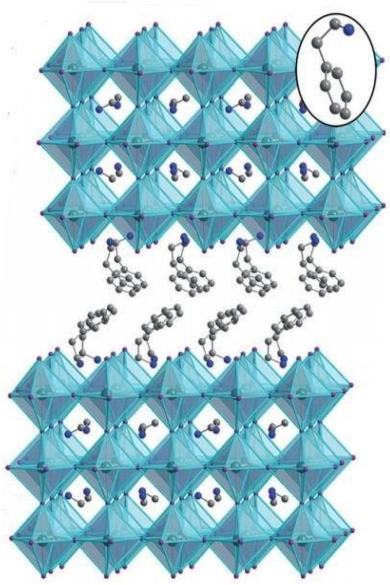

Figure 2-12: Schematic of a 2D perovskite with the inset showing a PEA^+ cation. [70]

A 2D structure is achieved due to the controlled dimensionality of the perovskite crystal initiated by the PEA^+ cation. [71] Although the 2D perovskite approach offers the possibility of fabricating films with high compactness and thus offering improved stability [72], the PCE of the devices is reduced due to an increase of Eg to ~2.1 eV compared to ~1.5 eV which is usually offered by conventional 3D perovskites. [16]

Another method to improve the crystallinity and mechanical stability of PSCs is via the use of additives. In general, additives form ion bonds with uncoordinated Pb^{2+} and hydrogen bonds between the additive, cation and halogen. Thus, iodide vacancies and other defect traps can be passivated and the performance of PSCs can be improved. [73] A recent approach was to incorporate n-propylammonium chloride (PACl) instead of methylammonium chloride (MACl) as an additive for $FAPbI_3$ based PSCs. Improved PCE was achieved due to the grain boundaries passivation by the PACl due to its large ionic size.[74]

2.2.6 Electrodes engineering

As previously described charge selective contacts are vital to ensure efficient performance for PSCs. A variety of HTLs have been recently used, which apart from carrier selectivity also affect the morphology of the perovskite active layer if they are used in p-i-n inverted structures. A variety of materials have already been incorporated as HTLs. Small molecules, such as the popular spiro-MeOTAD offer high purity and reproducibility.[75] Although high PCEs have been reported with spiro-MeOTAD, usually doping with Li-TFSi is an essential step to improve hole mobility and suppress charge recombination.[76] The hygroscopic nature of Li-TFSi has unfortunately hindered prolonged usage of this dopant due to poor moisture instability.[38] Thus doping free HTLs have been recently incorporated such as TTF-1 [38]. A popular alternative to small molecules is conductive polymers, such as the widely used PEDOT:PSS [77], which unfortunately due to its hygroscopic nature is very limiting in terms of offering good stability, especially under humidity exposure.[78] PEDOT:PSS can be replace by P3HT [79] and more recently by PTAA [80] which has also reported one of the highest PCEs (22.1%) for PSCs.[81] Due to their low cost, high chemical stability and good hole mobility, inorganic HTLs have also been successfully incorporated. A few examples include NiOx,[82, 83] CuO,[84] CuSCN [85] and the more recent $CuAlO_2$,[86] $CuGaO_2$[87] and $NiCo_2O_4$.[88, 89] One of the most novel technologies employed for PSCs is the incorporation of graphene-based HTLs which, although they have reported lower PCEs compared to other HTLs they show respectable advances towards the stability of PSCs. A few examples are single welled carbon nanotubes (SWNTs) embedded in an insulating polymer matrix which can effectively retard the ingress of moisture in the active layer as well as improved thermal stability[90] and reduced graphene oxide (RGO) which has shown improved conductivity and stability.[91]

One of the very first ETLs used in PSCs is TiO_2 as already mentioned. Even though TiO_2 offers a quite popular choice due to its favorable energy levels, and long electron lifetimes, [92,93] its inherent instability under UV exposure due to the electronic trap states has hindered it as sustainable choice for ETL. Modifications to TiO_2 such as doping with Al have shown to reduce the oxygen defects of TiO_2 and improve both PCE and stability. [94] Furthermore, Sb_2S_3 was reported as an efficient interlayer between TiO_2 and MAPI to improve the photo stability by isolating the two layers.[95] As a replacement to TiO_2, SnO_2 has shown excellent properties as an ETL due to its large Eg (~3.6 eV), high electron mobility [96]and improvements towards both humidity and thermal stability. [97] Fullerene and its derivatives have been one of the most popular choices as an ETL for p-i-n inverted structures. As we have previously mentioned, fullerenes such as PCBM can effectively passivate the grain boundaries of PSCs, thus effectively improving both PCE and stability. [36] Furthermore they offer favorable energy level alignment and good electron mobility which was reported to be further improved through doping with N-DPBI due to the reduced number of defect states.[98]

Metal electrodes also play an especially significant role towards the overall stability of PSCs. Common metal electrodes include Al, Ag, Au and Cu. Al is considered one of the least favorable choices due to the inherent instability from environmental conditions. Although Au is the most inherently stable from the metals mentioned above, its prohibitive cost renders it a non-practical choice for such applications. Furthermore Au has shown to be able to diffuse towards the perovskite active layer at temperatures as low as 70^oC. [51] Even though Ag is a much cheaper solution compared to Au, it is quite reactive with halide ions such as I^- and Cl^- which can quite easily diffuse through the grain boundaries of the perovskite crystal and corrode the metal electrode. [16] Recently, Cu was shown to be a very attractive candidate since it is less reactive with halide ions compared to Al and Ag, with PSCs reaching PCE=20% and retaining almost 98% of the PCE even after 816h under ambient conditions. [99] Stability of over 2000h was also reported in un-encapsulated PSCs in the dark under ambient conditions by utilizing a low temperature carbon electrode. [100] A figure summarizing the most popular electrodes and active layers for PSCs is shown in Figure 2-13 which was adopted by Chueh et. al. [33] Carbon electrodes have been recently explored as an alternative to metal electrodes as well. By optimizing the thickness of carbon electrode to balance its flexibility and conductivity, a recent study has reported PSCs with PCE=20.04 % and excellent stability. [101]

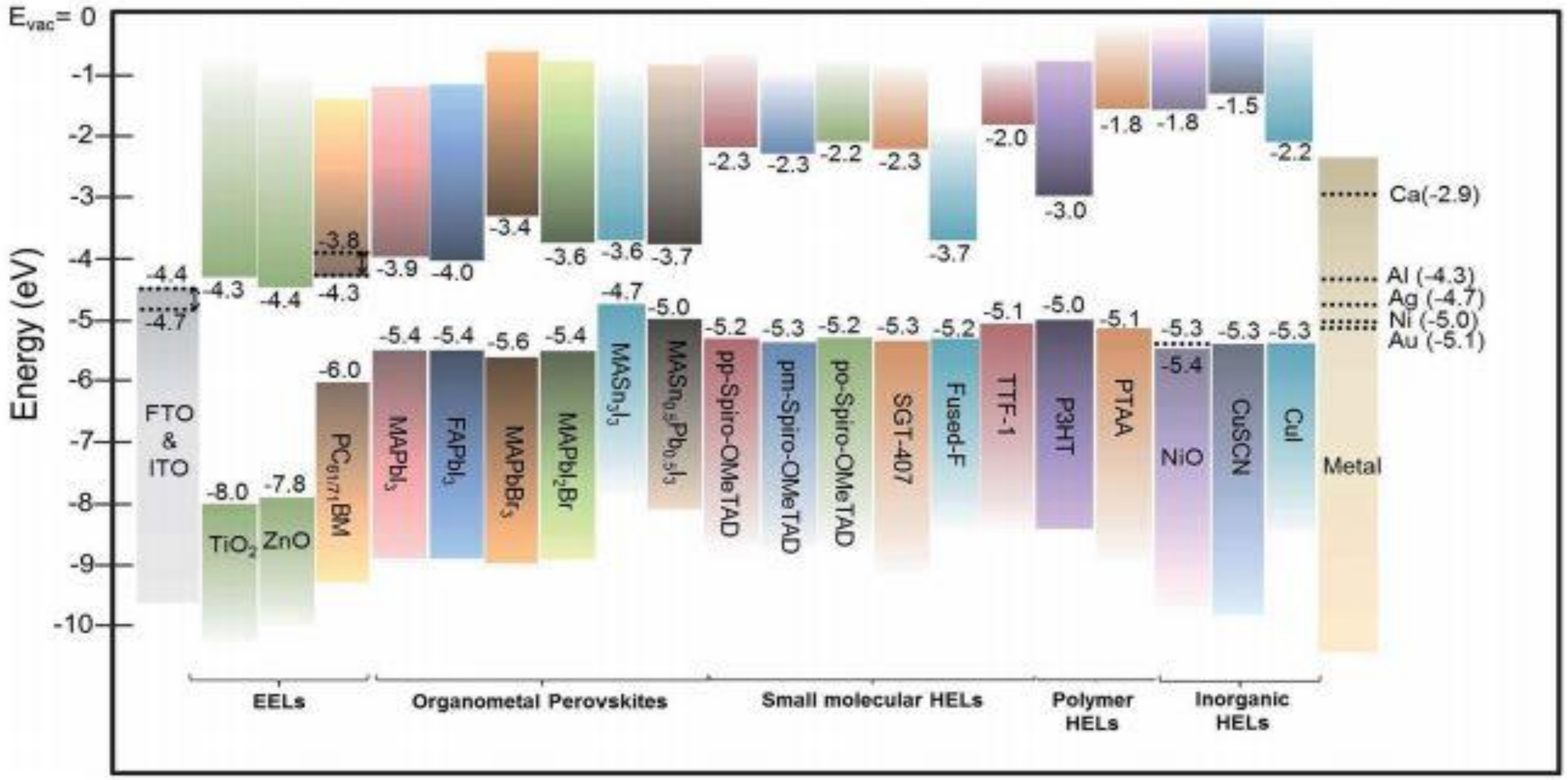

Figure 2-13: Schematic of energy level diagram of various active layers, ETLs and HTLs used in PSCs

3 MATERIALS AND METHODS

3.1 Materials

3.1.1 Substrates

ITO patterned soda lime glass purchased from Psiotec Ltd. were used as substrates for device fabrication. The specific parameters of the substrates are as follows: 14.8 x 14.8mm dimensions, 1.1 mm glass thickness, ITO sheet resistance 4-5 Ω/sq, ITO thickness 200-300 nm, ITO transmittance >85 % in the visible light spectrum. The schematic of the ITO pattern as well as the device active area are shown in Figure 3-1.

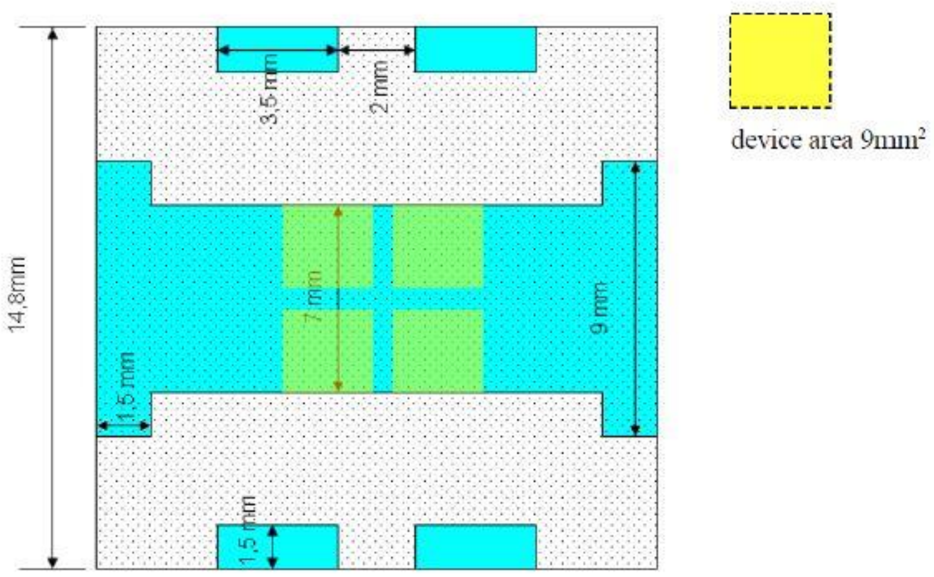

Figure 3-1: ITO pattern schematic on top of soda lime glass showing the device area (Yellow squares)

3.1.2 HTL precursors

- PEDOT:PSS Al4083, purchased from Clevios
- Nickel (II) hexahydrate (>98.5 %), purchased from Sigma-Aldrich
- Copper (II) nitrate trihydrate (99 %), purchased from Sigma-Aldrich
- Acetylacetone (≥99 %), purchased from Sigma-Aldrich
- β-alanine (99 %), purchased from Sigma-Aldrich
- 2-methoxyethanol anhydrous (99.8 %), purchased from Sigma-Aldrich

3.1.3 ETL precursors

- $PC_{70}BM$>99 %, purchased from Solenne BV
- Aluminium doped zinc oxide (2.5 wt%, Al:ZnO in 2-propanol) (AZO), purchased from Avantama (former Nanograde)
- Chlorobenzene anhydrous 99.8% (CB), purchased from Sigma-Aldrich
- Iron (III) chloride hexahydrate ($FeCl_3.6H_2O$, ≥97%)
- Oleylamine (85%), purchased from Sigma-Aldrich
- Sodium oleate (80%), purchased from Sigma-Aldrich
- Oleyl alcohol (85%), purchased from Sigma-Aldrich
- Diphenyl ether (99%), purchased from Sigma-Aldrich
- *N*,*N*-dimethylformamide (DMF, 99.9%), purchased from Sigma-Aldrich
- Acetone
- Acetonitrile (99.9%), purchased from Sigma-Aldrich
- Hexane (95%), purchased from Sigma-Aldrich
- Toluene (99.7%), purchased from Sigma-Aldrich
- Absolute ethanol (98%), purchased from Sigma-Aldrich
- 4-(2,3-Dihydro-1,3-dimethyl-1*H*-benzimidazol-2-yl)-*N*, *N*-dimethylbenzenamine (98 %), purchased from Sigma-Aldrich
- Nitrosonium tetrafluoroborate ($NOBF_4$, 97%), purchased from Acros Organics
- Bathocuproin (98 %), purchased from Alfa Aesar

3.1.4 Active layer precursors

The precursors for the perovskite active layer were:

- Methylammonium iodide 99%, purchased from Greatcell Solar
- Lead (II) iodide, 99.999%, purchased from Alfa Aesar
- γ-butyrolactone, purchased from Sigma-Aldrich
- Dimethyl sulfoxide anhydrous 99.9 % (DMSO), purchased from Sigma-Aldrich
- I201 perovskite ink (for Nitrogen processing), purchased form Ossila Ltd.

3.1.5 Metallization and encapsulation

The following materials were used for metallization and encapsulation:

- Aluminium cylindrical pellets 99.999%, purchased from GoodFellow
- Copper cylindrical pellets 99.9999%, purchased from Kurt Lesker
- E131 UV curable epoxy, purchased form Ossila Ltd.

3.2 Processing techniques

3.2.1 Spin coating

Spin coating is a widely used deposition technique in the field of solution processed electronics. The substrate is kept at a fixed position in the middle of a chuck with the help of a vacuum. The chuck alongside the substrate is then spun with a fixed rotational speed and the required solution is dispensed on the rotating substrate either prior (static) or while (dynamic) the substrate is spinning. The rotation causes radial liquid flow, while the air flow facilitates the evaporation of the solvent, thus resulting in the formation of a homogeneous film on the substrate. The spin coating process is shown in Figure 3-2. The parameters that can affect the film thickness are rotational speed, rotation time, solvent drying kinetics and concentration of the solution.

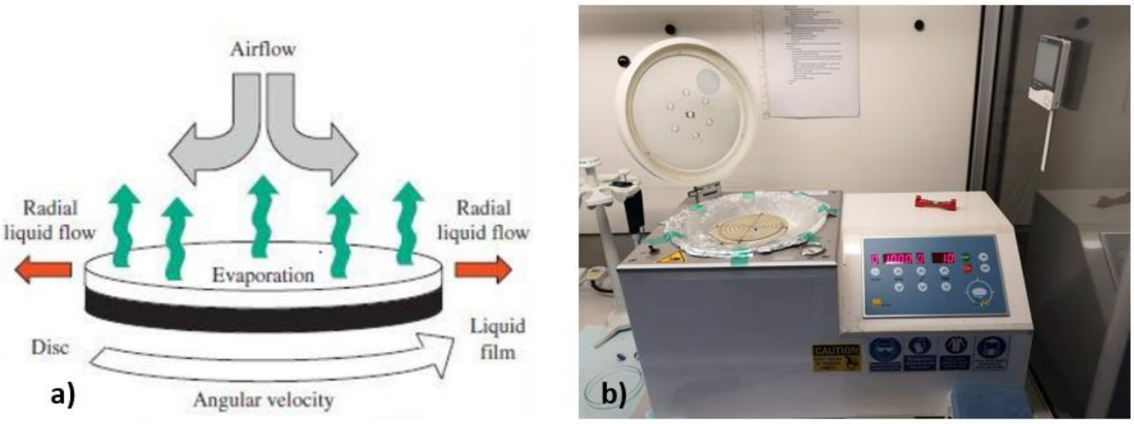

Figure 3-2: a) Spin coater schematic, b) spin coater system installed in MEP labs [102]

3.2.2 Doctor blade

Like the spin coating technique, Doctor Blade offers an alternative deposition technique that also has the advantage of being up scalable. A solution is place between a metal blade and the substrate that we wish to coat. After a specific volume of solution is placed between the blade and the substrate, the blade is moved across a heating plate and passes on top of the substrate, thus coating it and forming the film. The parameters that can affect the thickness of the film are blade height, blade moving speed, temperature of the hot plate and concentration of the solution. The Doctor Blade process is shown in the schematic of Figure 3-3.

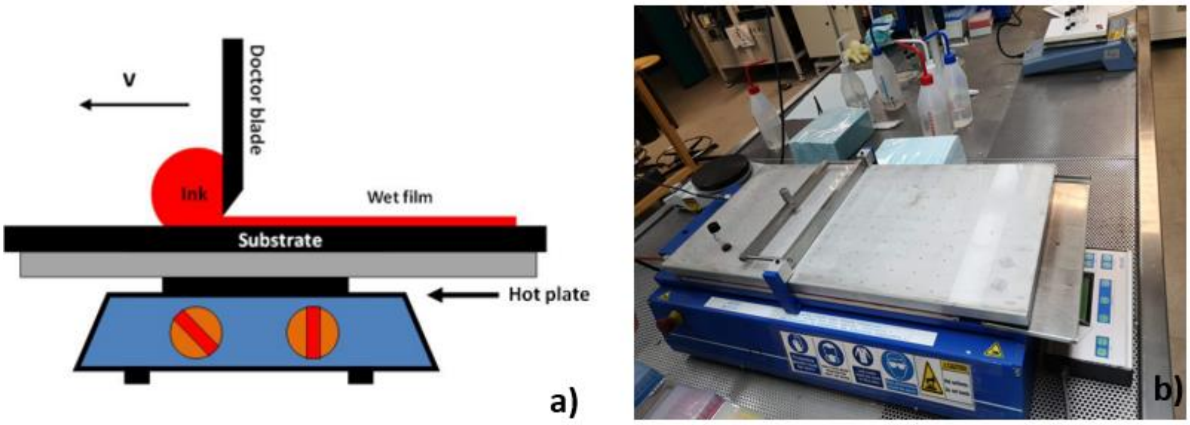

Figure 3-3: a) Schematic of Dr. Blade, b) Dr. Blade system installed in MEP labs [103]

3.2.3 Thermal evaporation

In thermal evaporation the material to be deposited in the substrate is placed in a heated boat up to its boiling or sublimation point under vacuum (~10^{-6} mbar) to avoid contamination. Vapors are created from the material placed on the boat which condense in the surface of the substrates which are rotating via a holder. An oscillating quartz crystal is used to control the deposition rate and final film thickness. The schematic showing the working principle of thermal evaporation is shown in Figure 3-4.

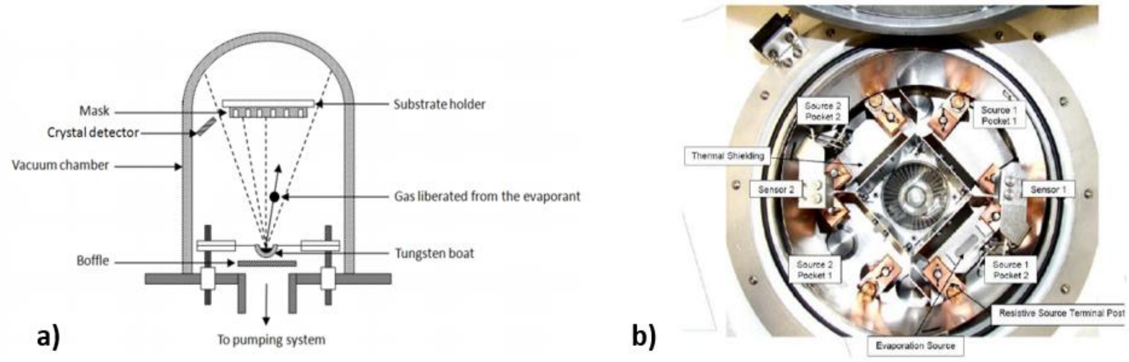

Figure 3-4: a) Schematic diagram of thermal evaporator b) thermal evaporator system installed in MEP labs [103]

3.3 Device fabrication

3.3.1 Substrate cleaning

The ITO coated substrates are thoroughly cleaned using acetone and isopropanol. The substrates are placed in an ultrasonic bath and undergo an additional cleaning step in the presence of acetone for 10 minutes, followed by ultrasonic bath sonication in isopropanol for an additional 10 minutes. The substrates are then dried using dry air and then placed at a hotplate at 120 ^{o}C for 2 minutes.

3.3.2 HTL deposition

PEDOT:PSS deposition: The PEDOT:PSS solution is filtered using a PVDF filter with 0.22 μm pore size and then stirred as described in the Materials section. The solution is then deposited on the substrates using the spin coating technique by placing 45 μL volume of solution dynamically in the spinning substrate at 6000 rpm for 30s. The films are then annealed on a hotplate at 150 ^{o}C for 10 minutes. Final film thickness is estimated at ~50 nm.

Cu:NiO$_x$ deposition: Combustion synthesis of Cu:NiO$_x$, 0.95 mmol of $Ni(NO_3)_2{\cdot}6H_2O$ and 0.05 mmol of $Cu(NO_3)_2{\cdot}3H_2O$ were dissolved in 2.5 mL 2-methoxyethanol. The solutions were stirred at 50 °C for 1 h., then, 0.1 mmol of acetylacetone was added to the solution, and the whole solution was left for further stirring for 1 h at room temperature. The Cu:NiOx films were coated using Doctor Blade with a blade speed of 5 mm/s and a plate temperature of 85 ^{o}C. The films were annealed at 300 ^{o}C on a hot plate for 1 h in ambient atmosphere

β-alanine deposition: Different concentrations of β-alanine (30, 10, 8 and 6 mg/ml) were prepared using deionized H_2O, and the pH was adjusted to 4.2 with 1M HNO_3. The solution was stirred at room temperature for 30 min. For the surface treatment, the β-alanine solution was drop-casted on the Cu:NiO_x films and were left to adhere for 5 min. Following that step, the spin coating process was initiated on the Cu:NiO_x layer at 6000 rpm for 40 sec. The β-alanine-treated films were annealed at 100 ^{o}C for 10 min.

3.3.3 Active layer deposition

$CH_3NH_3PbI_3$ formulation: The process is executed entirely inside a N_2 filled glovebox. A solvent of GBL:DMSO (7:3 M) is prepared. For the perovskite precursors MAI:PbI_2 (1:1) is prepared in a separate UV blocking vial. The final solution is used by using 1 ml of the prepared solvent in the MAI:PbI_2 mixture. The solution is left for stirring at 60 ^{o}C inside the glovebox for 1hour. The solution is then filtered using a PVDF filter with a pore size of 0.22 μm. The deposition of the perovskite is carried out via spin coating by statically dispensing 60 μL of solution. The coating is conducted in a 3-step process: step 1- 500 rpm for 5s, step 2- 1000 rpm for 45s, step 3 -5000 rpm for 45 s. After 20s have passed when step 3 was initiated, 0.5 ml of toluene are dropped in the spinning perovskite film to start the crystallization process. The perovskite films are then annealed at 100 ^{o}C for 10 minutes inside the glovebox. Final film thickness is estimated at ~300 nm.

$CH_3NH_3PbI_{3-x}Cl_x$ formulation: The I201 ink is heated on a hotplate at 70^{o}C for 2 hours inside a glovebox. The solution is left to cool down at room temperature prior to using it. The perovskite films are fabricated via spin coating using a solution volume of 30 μL dynamically dispensed at 4000 rpm for 30 s. The films are then annealed at 80 ^{o}C for 2 hours. The estimated film thickness is ~300 nm.

3.3.4 ETL deposition

$PC_{70}BM$ deposition for 70 nm film thickness: A solution of concentration 20 mg/ml by dissolving 20mg of $PC_{70}BM$ in 1ml of CB and was left overnight in a hotplate at 60 ^{o}C. The film was fabricated using spin coating by dropping 35 μL of the solution on top of the perovskite layer at a speed of 1000 rpm for 30s.

$PC_{70}BM$ deposition for 200 nm film thickness: A solution of concentration 50 mg/ml by dissolving 50mg of PCBM in 1ml of CB and was left overnight in a hotplate at 60 °C. The film was fabricated using spin coating by dropping 20 μL of the solution on top of the perovskite layer at a speed of 1000 rpm for 30s.

N-DMBI doped $PC_{70}BM$ film deposition: N-DMBI solutions of various concentrations to achieve the required doping concentrations were prepared in CB and left overnight under stirring and 60 °C. The solutions were then mixed with the $PC_{70}BM$ solution the next day. The film was fabricated using spin coating by dropping 20 μL of the solution on top of the perovskite layer at a speed of 1000 rpm for 30s.

AZO deposition: The AZO solution is stirred for ~1 hour. The deposition is conducted inside the glovebox by dropping 30 μL of the solution on top of the PCBM films at a speed of 1000 rpm for 30s, achieving a film thickness of 100 nm.

Synthesis of γ-Fe_2O_3 NPs: Iron oxide NPs with an average diameter of ~5 nm was prepared using the following method. $FeCl_3.6H_2O$ (5.4 g, 20 mmol) and sodium oleate (18.25 g, 60 mmol) were added to a mixture of ethanol (40 mL), deionized water (30 mL), and hexane (70 mL). The mixture was refluxed at 70 °C for 4 h, then the upper brown hexane solution containing iron–oleate complex was separated, washed three times with deionized water (50 mL), and dried under vacuum at 60 °C for 12 h, yielding a dark brown, oily iron oleate complex. Finally, iron oleate complex (10.8 g) was dissolved in 60 g of diphenyl ether with the addition of oleyl alcohol (19.4 g). Under N_2 flux, this mixture under stirring was heated to 105 °C at a ramp rate of 2 °C min^{-1} and kept for 10 min at this temperature to eliminate H_2O and adsorbed O_2. After that, the mixture was heated to 220 °C at a ramp rate of 2 °C min^{-1} and the reaction could proceed for 20 min at this temperature. The resulting black brown nanocrystal solution was cooled to room temperature naturally. Then, the Fe_2O_3 NPs were precipitated with 50 ml acetone followed by centrifugation at 14.500 rpm for 20 min and redispersed in hexane to form a stable colloidal solution (10 mg mL^{-1}).

Preparation of ligand-stripped γ-Fe_2O_3 NPs: The surface of Fe_2O_3 NPs was modified with $NOBF_4$ using a ligand-exchange reaction. Briefly, equal volumes (5 mL) of colloidal Fe_2O_3 NPs in hexane and 0.01 M $NOBF_4$ in acetonitrile were mixed and the resulting mixture was kept stirring at room temperature until the NPs were transferred to the acetonitrile phase (typically within ~1 h). The BF_4^- capped Fe_2O_3 NPs were then collected by precipitation with toluene followed by centrifugation, dried under vacuum at 40 ^oC for 12 h, and dispersed in ethanol to form a stable colloidal solution (5 mg mL^{-1}).

γ-Fe_2O_3 film deposition: The γ-Fe_2O_3 NPs dispersion (5 mg L^{-1} in ethanol) was dynamically spin coated at 3000 rpm for 30 s on top of the PC70BM films inside a glovebox to form a ~20 nm γ-Fe_2O_3 film.

BCP film deposition: BCP was deposited using thermal evaporation at a rate of ~0.2 Å using a shadow mask under a pressure of 10^- mbar. The final thickness of BCP electrode is estimated at 7 nm.

3.3.5 Metallization and encapsulation

Al evaporation: Al metal electrode is evaporated at a rate of ~2 Å using a shadow mask under a pressure of 10^- mbar. The final thickness of the Al metal electrode is 100 nm. The active area of the devices is defined using the shadow mask, thus achieving a device area of 0.9 mm^2.

Cu evaporation: Cu metal electrode is evaporated at a rate of ~2 Å using a shadow mask under a pressure of 10^- mbar. The final thickness of the Al metal electrode is 100 nm. The active area of the devices is defined using the shadow mask, thus achieving a device area of 0.9 mm^2.

Encapsulation: After evaporation, the encapsulation is performed using the E131 epoxy and a glass coverslip. The epoxy is placed in the middle of the substrate, ensuring coverage of the whole device area while avoiding direct contact of the epoxy with the contacts. The substrates are then exposed to UV irradiation of 365 nm inside the glovebox for 2 minutes to cure the epoxy.

3.4 Characterization techniques

3.4.1 J/V characteristics

To evaluate the performance of any solar cell the J/V characteristics are analyzed. The J/V plots were taken using a Botest LIV functionality test system with 10mV step size and 40 ms step time. As a light source a Newport solar simulator equipped with 150W Xe lamp was used, providing AM 1.5G and 100 W/cm^2 power as measured by a certified Oriel 91150 V calibration cell. Prior to each measurement a shadow mask was attached to the substrates to correctly define the 9 mm^2 device area. Several PV parameters can be extracted both from the JV plot as well as considering the equivalent circuit model for a solar cell, shown in Figure 3-5.

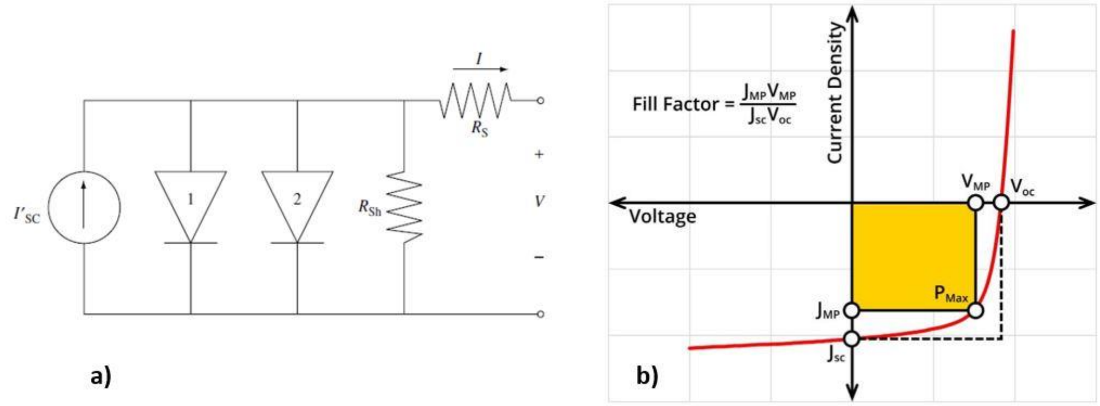

Figure 3-5: a) Equivalent circuit mode for solar cells [4] b) J/V plot of a solar cell [104]

Under dark, the solar cell effectively acts as a diode, which is denoted by the diode symbol in the ECM. The current source is used to model the photo-generated current of the solar cell when no external bias is applied (V=0) and is called J_{SC}. J_{SC} is usually affected by the absorption properties of the active layer, photo-generation as well as charge transport and extraction. Purely from an engineering point of view, the total current I produced by the solar cell is calculated using equation 11.

$$I_{pv}=I_{sc} - I_{d1} (e^{qV/kT} -1) - I_{d2} (e^{qV/2kT} -1) \qquad (11)$$

Id_1 and Id_2 denote the dark saturation currents flowing through diode 1 and diode 2, respectively. V is the applied voltage, T is the temperature, q is the elementary charge and k is the Boltzman's constant. Id_2 is the recombination current in the depletion region, which is usually very small and can be neglected. Id_1 is the recombination current due to bulk and surface recombination events. Under short circuit conditions (V=0) I_{d1} is also negligible and therefore the total current produced by the solar cell is I_{PV}=Isc. When an external bias is applied, I_{d1} starts to increase and contributes to I_{PV}. The bias value at which I_{d1} completely counteracts J_{SC}

, and therefore, the circuit reaches open circuit conditions (I=0) is called V_{OC}, which is given by equation (12).

$$V_{oc}=kT/q\ (I_{sc}/I_{d1}) \quad (12)$$

V_{oc} is primarily affected by the energy levels of both the active layer as well as the electrodes and charge carrier recombination rates. It is interesting to note that the solar cell has a specific voltage (V_{MP}) and current value (I_{MP}) that can operate under which produces maximum power (P_{MP}). This is denoted by the yellow square in Figure 3-5. In the case of a perfect diode, maximum power would be achieved under Isc and V_{OC}, which is never the case in a perfect world. The ratio between the power at V_{MP}, I_{MP} and V_{OC}, Isc is called FF and is given by equation (13), effectively showing how ideal the diode characteristic of the solar cell is, or as it is often called, the “squareness” of the J/V plot.

$$FF=V_{mp}I_{mp}/V_{oc}I_{sc} \quad (13)$$

One of the most important parameters of a solar is the PCE which gives the overall efficiency of the device and is shown in equation 14.

$$PCE=FFV_{oc}I_{sc}/P_{mp} = P_{in}/P_{mp} \quad (14)$$

P_{in} denotes the power of incident light and as it was previously described, a reference standard is using AM 1.5G, which corresponds to P_{in}= 100 W/m^2.

R_S denotes the series resistance, and it is affected by energetic barriers, at the bulk as well as at interfaces. It is also affected by the conductivity of the layers used. The value of R_S should preferably be small for efficient PV operation. R_{SH} denotes the shunt resistance, which is affected by alternate current pathways, leading to leakage current in the devices. The value of R_{SH} is preferably large for efficient PV operation.

3.4.2 Ultraviolet-Visible Spectrophotometry (UV Vis)

Uv-Vis is a particularly useful characterization technique that is usually employed for film characterization. We have used a Shimadzu Uv-visible spectrophotometer UV 2600/2700 equipped with a Xe lamp and an integrating sphere. The wavelength used was varied from 350-800 nm. In particular, the absorption, transmittance and reflectance of the films can be characterized. The intensity of the light is determined in each wavelength by the photodetector before and after the light interacts with the sample. The system used is shown in Figure 3-6.

Figure 3-6: Shimadzu UV 2600/2700 system installed in MEP labs

3.4.3 Impedance spectroscopy

Undoubtedly impedance spectroscopy is an enormously powerful characterization technique that can be used to identify physical mechanisms governing the operation of solar cell devices. Similar to resistance, impedance represents the ability to resist the flow of electrical current. However, resistance only applies for one circuit element, the resistor and is independent of frequency, whereas impedance applies to every circuit element and depends on frequency. A whole circuit can be characterized with one impedance value from the combination of the impedances of its elements. By applying an AC voltage bias to a circuit, the response is measured as an AC current signal and the impedance can be calculated using equation (15), which analogous to Ohm's law

$$Z(j\omega) = V(j\omega) / I(j\omega) \qquad (15)$$

Two of the most popular plots that can be extracted using impedance spectroscopy are: a) Nyquist plots that show a representation of real and imaginary part of the impedance in different frequencies b) Mott-Schottky plots that show how the capacitance of the device changes in terms of applied voltage at a fixed frequency. Typical Nyquist and Mott-Schottky plots can be seen in Figure 3-7.

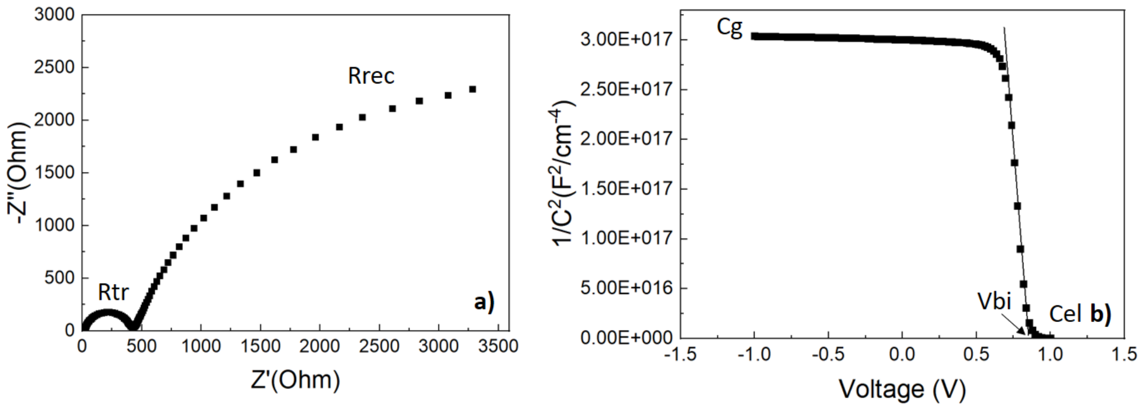

Figure 3-7: a) Typical Nyquist plot of PSC b) typical Mott-Schottky plot for PSC

For a typical Nyquist plot there are two frequency responses that can be observed in PSCs. The high frequency response (HFR) is attributed to charge transport resistance (R_{TR}) which is attributed to the charge transport in the device electrodes and can be affected by the conductivity of the electrodes. The low frequency response (LFR) is attributed to the charge recombination resistance (R_{REC}) and is affected by the charge accumulation due to both ionic and electronic accumulation in the electrodes as well as charge carrier recombination. In general, R_{TR} should be as small as possible, whereas R_{REC} should be as large as possible to ensure efficient devices.

Mott Schottky plots are based on the depletion approximation, where we consider that the capacitance in the space charge region is purely due to doping and there are no free charges. The capacitance in terms of voltage can be described using equation (16).

$$C^{-2}= 2 (V_{bi}-V)/q\varepsilon\varepsilon_0 N \quad (16)$$

It is interesting to note that in general this approximation does not hold true close to the metal contacts that charges tend to accumulate, thus the value of V_{BI} calculated from the Mott-Schottky analysis is not the true value of V_{BI} but can still be used for comparative studies. V_{BI} is calculated by the x-axis intercept of the slope in the Mott-Schottky plot. The slope is also inversely proportional to the doping density, N. Although perovskites are generally accepted as undoped materials, they can still exhibit unintentional doping due to ionic vacancies in the crystal structure. Under reverse bias a capacitive plateau is observed that is attributed to the geometric capacitance (C_g). C_g is affected by the polarizability of the perovskite active layer and is strongly associated with its dielectric response.

Impedance spectroscopy was used to assess the charge accumulation properties of HTLs in our previous work using capacitance-frequency (CF) plots. CF plots are a different representation of the Nyquist plots that indicate a representation of capacitance change with respect to frequency. Capacitance at HF (C_{BULK}) is related to the capacitive characteristics of the perovskite active layer, whereas capacitance at LF (C_{EL}) is related to charge accumulation at the interfaces, under illumination Using CF plots we have shown that capacitance at the interfaces of devices based on CuO is significantly reduced compared to Cu:NiOx and PEDOT:PSS, indicating more efficient charge extraction accompanied by improved PCE. [84]

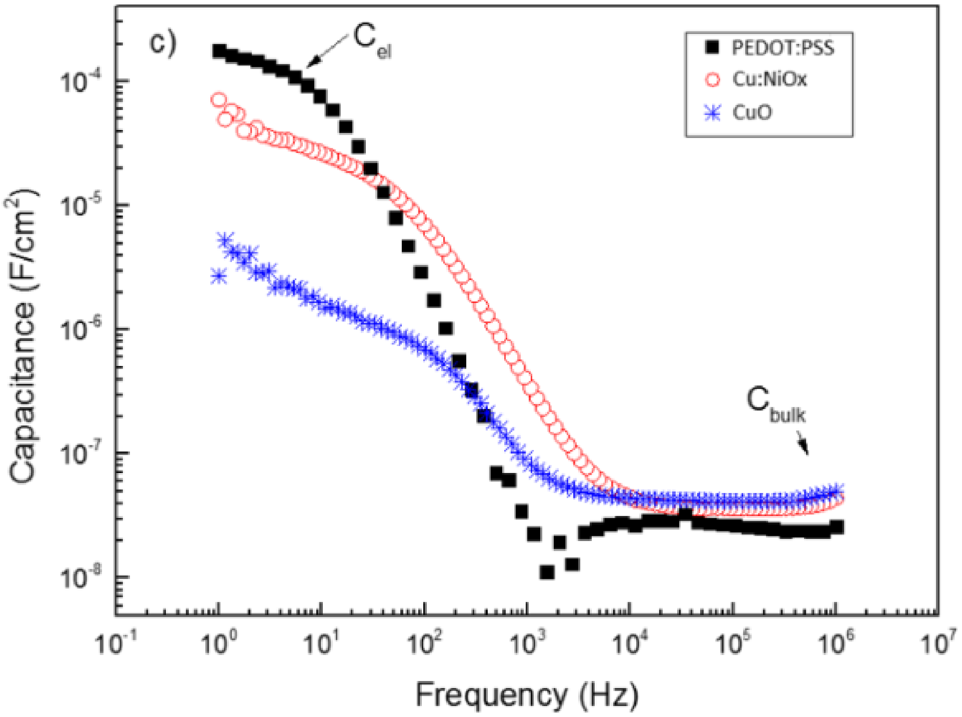

Figure 3-8: CF plot of perovskite devices based on PEDOT:PSS, Cu:NiOx and CuO HTL.

Impedance spectroscopy was performed using an Autolab PGSTAT 302N equipped with FRA32M module. To extract the Nyquist plots, the devices were illuminated using a white LED with 100 mw/cm^2 power. A small AC perturbation voltage of 10 mV was applied, and the current output was measured using a frequency range of 1 MHz to 1 Hz. The steady-state DC bias was kept at 0 V. The C–V measurements for the Mott–Schottky plots were performed under dark using a voltage range of -1 to 1 V and a steady frequency of 5 kHz.

3.4.4 Photocurrent Mapping (PCT)

PCT is a technique used to visualize the current distribution in a solar cell device. The system used is a Botest Photoelectric Test System – PCT 1 equipped with a 405 nm laser with 25 mW power. The laser beam is moved laterally on top of the sample by specially coated mirrors. The laser beam hits every pixel of the device, and photocurrent is generated. When no external bias is applied, the photocurrent detected represents the J_{SC} of the device in each pixel. By scanning the whole device area, a visual representation of the J_{SC} is achieved, where areas appearing with a bright red color indicate the highest J_{SC}, whereas areas with a blue color indicate very low or absence of J_{SC}. The system used is shown in Figure 3-8.

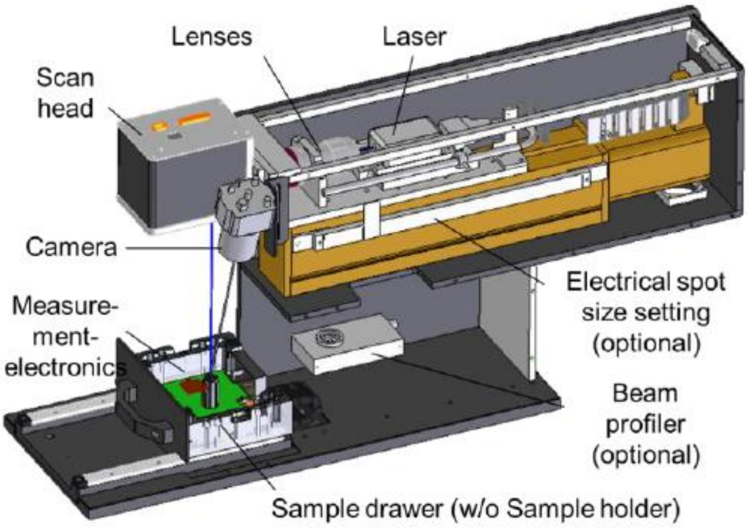

Figure 3-9: Photocurrent system schematic representation

3.4.5 Atomic Force Microscopy (AFM)

AFM is a form of surface probe microscopy (SPM) technique that can be used to characterize the morphology of films such as topography, roughness, compactness, grain size and grain boundaries. A Nanosurf easyScan 2 AFM was used. The measurements were performed in tapping mode using a Tap 190Al-G silicon tip with aluminium reflex coating, resonance frequency of 190 kHz, force constant 48N/m and an average tip radius ≤ 10 nm. The tips were purchased form Budget Sensors Company. A sharp tip is used to "sense" the surface of films while a feedback loop controls the position of the tip on the surface of the sample. The feedback loop identifies and adjusts the position of the tip using a laser beam that hits the top of the tip and then passes through a photodetector. The tip comes in very close contact with the film surface (1-10 nm) and measures interactions such as Coulomb and Van der Waal's forces. There are two main modes that can be used in AFM: a) contact mode, where the tip comes in very close contact with the surface of the film, b) tapping mode, where the tip is vibrating in a preset oscillating frequency and due to its non-destructive nature is used to characterize soft materials and give additional information such as grain size and grain boundaries. The AFM system used is shown in Figure 3-9.

Figure 3-10: **Nanosurf easyScan 2 AFM system installed in MEP labs**

3.4.6 Profilometer

The thickness of each device layer was determined using a Veeco Dektak 150 stylus profilometer. The films were mechanically scratched prior to the profilometer measurement to determine the thickness. The system uses a sharp tip that is passed along the surface of the film and over the scratched line that was mechanically induced in the film to determine the thickness. The system is shown in Figure 3-10.

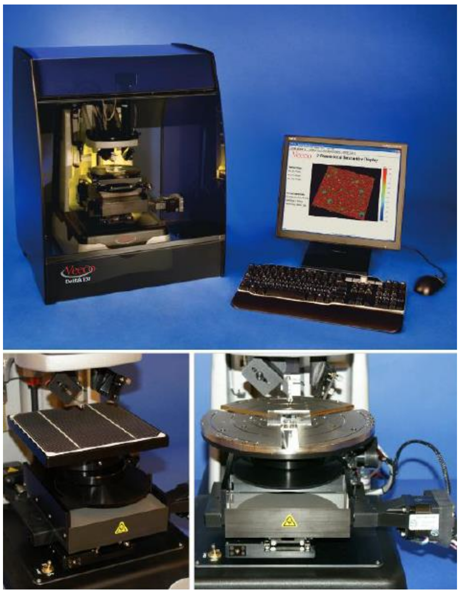

Figure 3-11: Veeco Dektak 150 stylus profilometer installed in MEP labs.

3.4.7 Photoluminescence Spectroscopy (PL)

PL measurements were performed using a Jasco FP-3800 spectrofluorometer. During the characterization, thin films were irradiated with high intensity light, higher than the band gap energy of the characterized semiconducting film. Via the irradiation process, photoexcitation of electrons from the valence band (E_V) to the conduction band (E_C) occurs. During the band to band (radiative) recombination of these electrons with holes the intensity and wavelength of the emitted light is recorded by a detector and the PL spectrum is plotted.

Figure 3-12: Picture of Jasco FP-3800 spectrofluorometer

4 EFFECT OF THE ETL ON THE LIFETIME PERFORMANCE OF P-I-N PEROVSKITE SOLAR CELLS UNDER ACCELERATED HEAT CONDITIONS

4.1 Abstract

In this work the major degradation pathway for p-i-n PSCs was confirmed under accelerated heat conditions (85 ^{o}C, N_2) for devices utilizing $CH_3NH_3PbI_3$ formulation. By utilizing two different thicknesses of $PC_{70}BM$ (70 and 200 nm respectively) and buffer layer engineering the interaction of Al metal electrode with the perovskite active layer via diffusion mechanisms is confirmed as the major degradation pathway and isolation of the two layer is the key for improved stability. However, the incorporation of thick $PC_{70}BM$ has a negative impact to the PCE. Following the above, the effect towards heat stability of three different ETLs ($PC_{70}BM$, $PC_{70}BM$/AZO and the novel $PC_{70}BM/\gamma\text{-}Fe_2O_3$) is studied. The best stability is observed by $PC_{70}BM/\gamma\text{-}Fe_2O_3$ due to improved V_{OC} stability, which is attributed to more intimate interface with the top electrode and reduced charge trap density as it was observed by impedance spectroscopy. The worst stability is observed in $PC_{70}BM$/AZO devices due to the basic nature of the residual –OH groups of the NPs, causing deprotonation of the MA^+, thus leading to the decomposition of the perovskite crystal. Finally, the efficiency-stability gap of devices that incorporated thick $PC_{70}BM$ is reduced by using a perovskite formulation which is optimized to work with large thicknesses of $PC_{70}BM$ and is based on $CH_3NH_3PbI_{3-x}Cl_x$. Using this approach, improved stability at ~1000h under accelerated heat conditions (60^{o}C, N_2) and a PCE ~10% is achieved.

4.2 $CH_3NH_3PbI_3$ film characterization

$CH_3NH_3PbI_3$ ($MAPbI_3$) has been previously reported to be mostly intrinsically stable at 85 °C under N_2 atmosphere by Conings et. al.[48] In order to confirm previous observations, ITO/PEDOT:PSS/$CH_3NH_3PbI_3$ films were annealed at 85 °C on a hotplate inside a N_2 filled glovebox in the dark for 96 hours. The XRD patterns of fresh and thermally annealed films are shown in Figure 4-1a. Similar to what has been previously reported in the literature, [105] the XRD patterns show no traces of PbI_2, judging by the absence of diffraction peaks at 12.7° and 38.7°. Although there is a peak at 52.4° which has been previously attributed to PbI_2 phase, the size of this peak does not change upon thermal treatment. This suggest that $CH_3NH_3PbI_3$ is intrinsically stable at temperatures to 85 °C under N_2, which is in agreement with previous studies. [48] The UV-Vis absorption spectra of fresh and aged perovskite films also remain quite unchanged and are similar to the ones reported by Conings *et.al* which further points towards the intrinsic stability of the perovskite film (Figure 4-1 b).

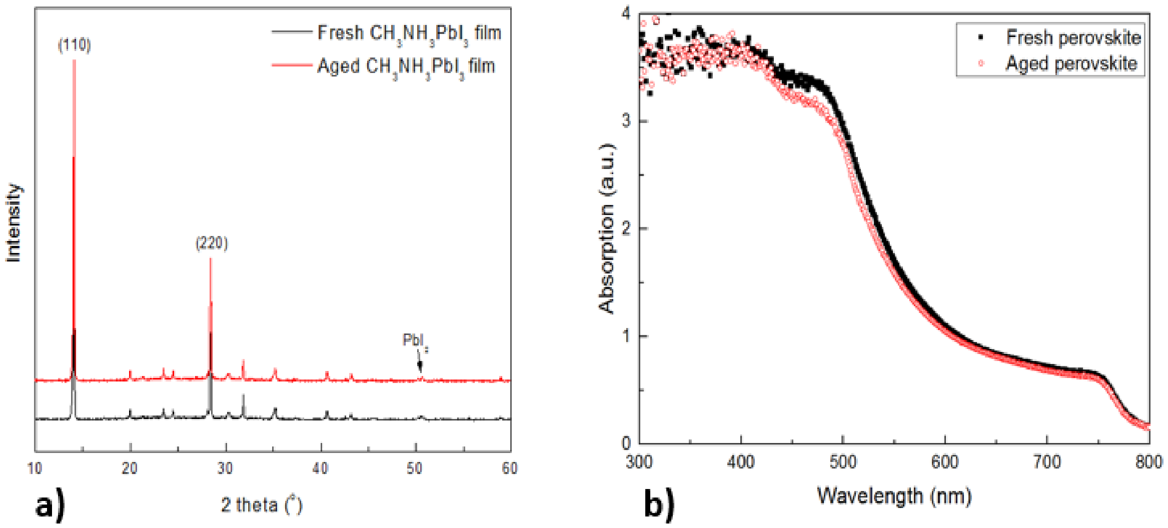

Figure 4-1: a) XRD spectra of fresh and aged perovskite films, b) Absorption spectra of fresh and aged perovskite films

4.3 Heat stability and characterization of $CH_3NH_3PbI_3$-based devices using different $PC_{70}BM$ thickness

Two different sets of p-i-n solar cells incorporating different fullerene thicknesses, i.e., $PC_{70}BM$ with ~70 nm (thin fullerene-based devices) and $PC_{70}BM$~200 nm (thick fullerene-based devices) film thickness are evaluated. The devices were encapsulated using a UV-curable encapsulation epoxy and a small glass slide as it was described in chapter 3.3.3 to avoid any ingress of moisture and then placed on a hotplate at 85 °C in a N_2-filled glovebox under dark. The devices were taken outside of the glovebox to measure the PV device performance parameters and undergo the characterization process. The devices were then placed back again inside the glovebox to continue the aging process. This procedure was repeated at 24h intervals for up to 168 h. The deterioration of the average normalized photovoltaic parameters from 8 devices from each device set was monitored over the course of 168 hours at 24-hour intervals and is shown in Figure 4-2.

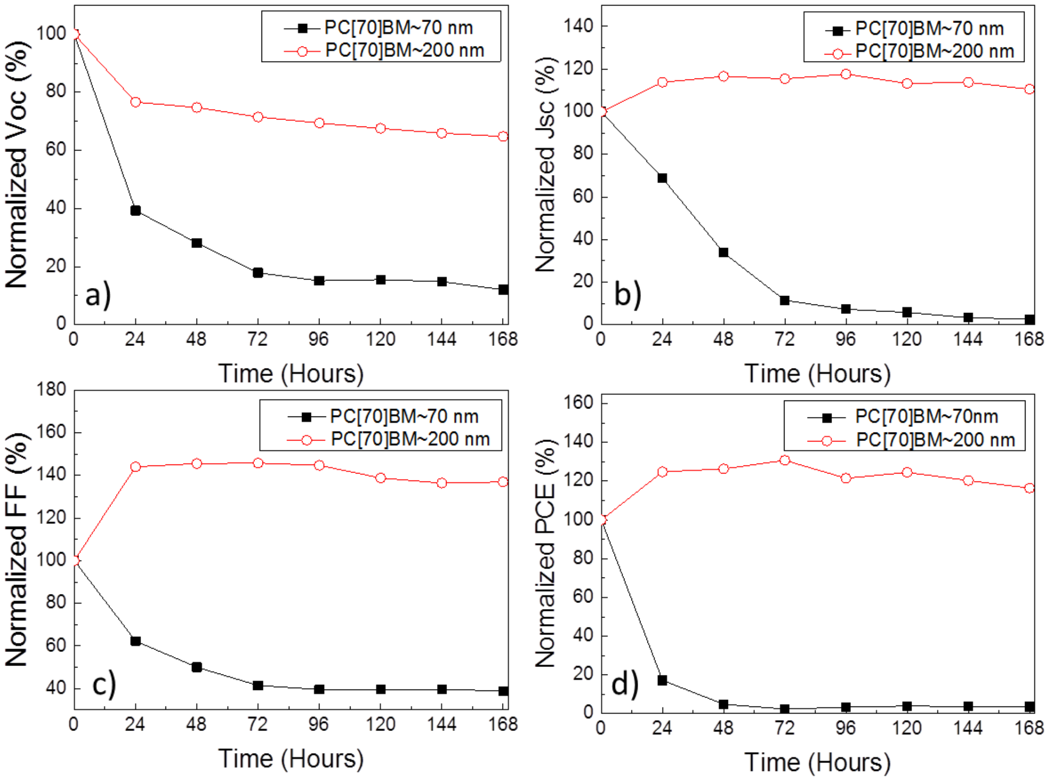

Figure 4-2: Normalized a) V_{oc}, b) J_{sc}, c) FF and d) PCE of $CH_3NH_3PbI_3$ based devices over 168 hours of heating at 85 °C using two different fullerene buffer layer thicknesses.

From Figure 4-2 there are striking differences between the two sets of devices. The thin-fullerene based device exhibits a very sharp drop to all their photovoltaic parameters only just after 24 hours of heating. The drop in photovoltaic parameters seems to stabilize at the 72-h mark. However, the device PCE has already dropped well below 20% by that point. On the other hand, thick-fullerene based device retains almost 100% of the PCE even after 168 hours of heating. Although there is a noticeable drop of the V_{OC} at ~80% at the first 24 hours, there is an equally increase in J_{SC} (115%), and especially FF (140%), for this device. Both the drop in V_{OC} and increase in J_{SC} and FF are stabilized after 24 hours, allowing the thick-fullerene based device to preserve its high PCE (~100 %) even after 168 hours of heating.

Representative devices from each device configuration were chosen for characterization. The representative devices yielded the following photovoltaic parameters: thin-fullerene based device (V_{oc}=0.91 V, J_{sc}=14.75 mA/cm^2, FF=79.2 %, PCE=10.64 %), thick-fullerene based device (V_{oc}=0.87 V, J_{sc}=10.57 mA/cm^2, FF=40.8 %, PCE=3.75 %). These measurements indicated a considerable decrease in FF when we increase the thickness of $PC_{70}BM$, due to the limited electrical conductivity of the material. [26] The purpose of this study was to identify the major degradation pathway of the $CH_3NH_3PbI_3$ formulation-based devices under accelerated heat conditions and to evaluate the effect of different fullerene thickness on the device lifetime performance. For the above reasons achieving the highest possible PCE for each device set was not within the targets of this experimental plan.

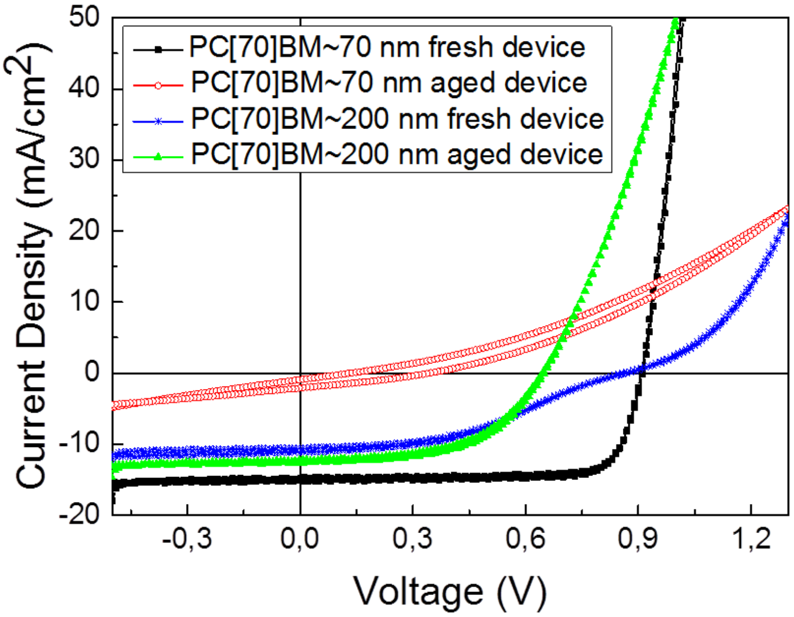

Figure 4-3: Illuminated J/V characteristic for fresh and aged $CH_3NH_3PbI_3$ based devices.

Figure 4-3 shows the illuminated J/V characteristic of fresh and aged devices after 96 hours of heating. The 96 hours mark was chosen as the point of degradation where all the characterization studies were performed on the examined samples. The reason for this choice was that at the 96 hours mark the decline of the photovoltaic parameters has been substantially reduced. As it can be seen from Figure 4-3, the shape of the J/V curve for thin-fullerene based devices is severely distorted after 96 hours of heating, which is consistent with the severe drop on photovoltaic parameters, as evident from Figure 4-2. Furthermore, significant signs of hysteresis start to appear within the device performance characteristics, which were absent from the fresh devices. Hysteresis in perovskite solar cells has been previously attributed, amongst other phenomena, to non-steady state capacitive currents resulting from electrode polarization. [25] Thus, the manifestation of hysteresis in the J/V plot could point to electrode degradation in the device, which prevents the efficient extraction of carriers. On the other hand, the thick-fullerene based devices do not exhibit any shape deterioration of the J/V plot or any hysteresis behavior after degradation. This correlates well with the stable performance of the thick-fullerene based devices, where the initial values of the photovoltaic parameters are mostly retained.

Furthermore, the J/V plots of thick-fullerene based devices show an S-shaped profile growth prior to the heating test, which completely disappears after 96 hours of annealing. An S-shape in the J/V curves has been previously attributed to poor charge extraction, which in our devices can be related with the large thickness of the $PC_{70}BM$ layer. [106] The absence of the S-shape after 96 hours heating could be a result of the light soaking effect from the constant light illumination during the characterization of the devices. It has been previously reported that this phenomenon is a result of the trap-assisted recombination of excitons [107], which can be strengthened due to the increase in trap density in the thick $PC_{70}BM$ film. The different J_{SC} behavior from both the lifetime plots and illuminated JV characteristics was also observed when we performed photocurrent testing (PCT) measurements. PCT is a very useful technique for degradation studies that has been previously used in organic photovoltaics (OPVs) as well [108] for the visualization of how the current intensity is distributed inside a device. As it was expected, the device incorporating thin $PC_{70}BM$ layer exhibited a severe loss to current intensity, whereas the device with thick $PC_{70}BM$ layer retained its current intensity to a good degree as shown in Figure 4-4.

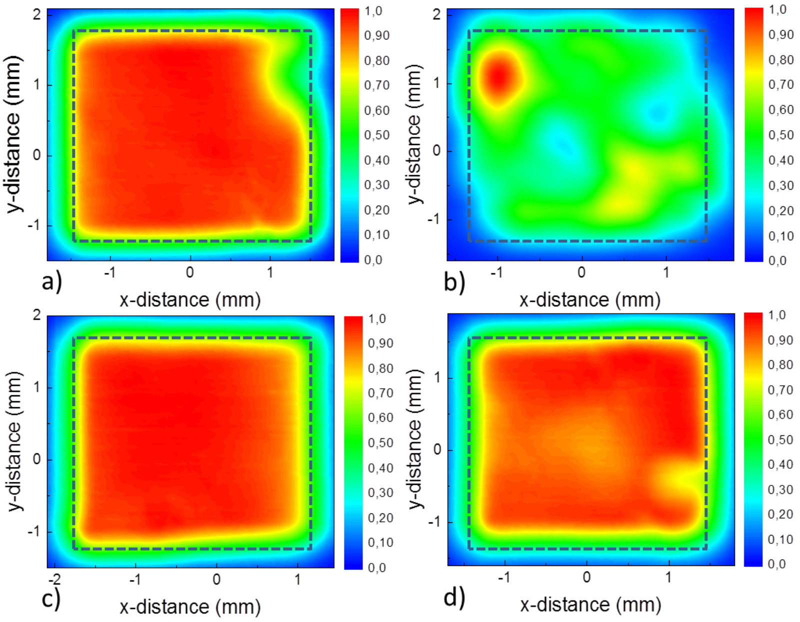

Figure 4-4: PCT mapping for: a) fresh thin fullerene-based devices b) aged thin fullerene-based devices c) fresh thick fullerene-based devices d) aged thick fullerene-based devices

Complementary to the previous characterization techniques, impedance spectroscopy was also used to provide insight on the physical processes occurring inside the device. [24]The impedance spectroscopy data were analyzed and represented using Nyquist as well as Mott-Schottky plots.

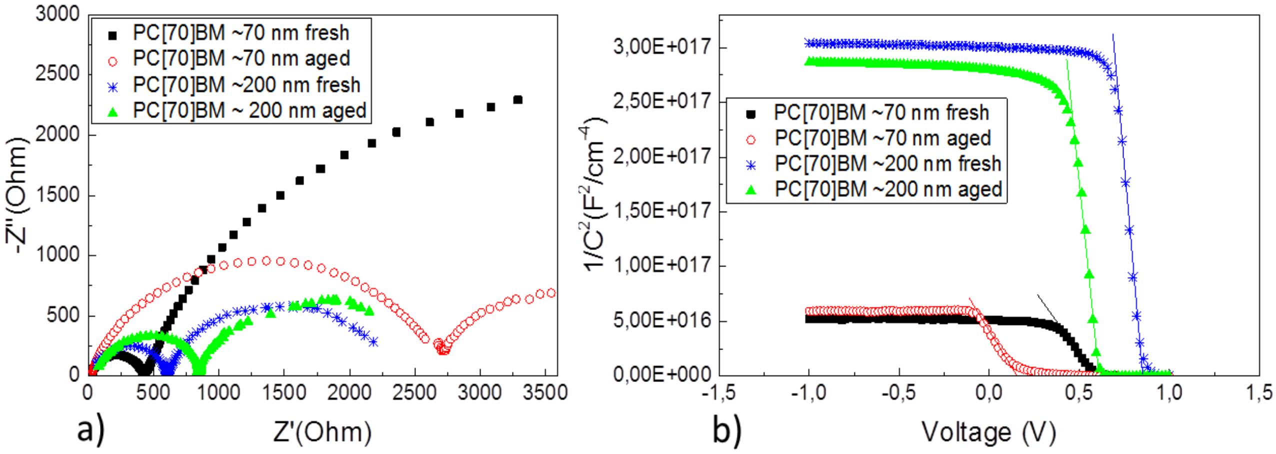

Figure 4-5: a) Nyquist plots, b) Mott-Schottky plots of representative devices

Figure 4-5a shows the standard shape of two frequency responses for perovskite solar cells (a high- and low-frequency feature). As described in chapter 3.4.3, the feature at high frequencies has been previously attributing to charge transport resistance (R_{TR}) of the hole transporting layers (HTLs) and electron transporting layers (ETLs) as well as their interface with the perovskite active layer. [109], [84] The low frequency feature has been attributed to the recombination resistance (R_{REC}) and ionic diffusion. [110] From the results in Figure 4a, a significant decrease in R_{REC} is observed between fresh and aged thin-fullerene based devices as well as an increase in R_{TR}. The increase to R_{TR} denotes that the ETL/HTL or their interface with the perovskite has been altered, making carrier movement inside the device more difficult. This in return results to a decrease of R_{REC} due to more frequent charge recombination events. The combination of increasing R_{TR} and decreasing R_{REC} is in good agreement with the decreased FF (~40%) noted for thin-fullerene based devices, highlighting the difficulty for carrier extraction. On the other hand, the R_{TR} for thick-based devices remain relatively unchanged, whereas a slight increase of the R_{REC} was observed which could be tied with the normalized FF increase.

Mott-Schottky analysis is often used for the differentiation of processes occurring at the active layer with the ones occurring at the interfaces and outer contacts of the device. [111] The capacitive plateau at negative voltages of Figure 4-5b provides information on the dielectric constant, which is an intrinsic property of the bulk material. A decrease in V_{BI} is observed (point of intersection of the slope with the x-axis) for both thin and thick fullerene-based devices, which denotes that the energy equilibration at the contacts has shifted. [111] More importantly, V_{BI} for thin-ETLs based devices has dropped by ~0.5 V whereas for thick-fullerene based devices only by ~0.25 V. This is in accordance with the more rapid decrease of normalized V_{OC} for the thin-ETLs based devices compared to the thick-fullerene based devices, where the V_{OC} drop is a lot less apparent and more stable.

4.4 Buffer layer device engineering

To try and isolate the effect of heat in each layer of the device, buffer layer engineering methods were used. This is a powerful technique, which was also previously used in organic photovoltaics (OPVs) [108] allowing us to study the effect of the PV parameters in a fabricated device using aged films at 85 °C for 96 hours, similar to the conditions used for device characterization. To achieve this goal, semi-finished device structures (4 device structures from each device set) were initially fabricated using semi- finished aged films of ITO/PEDOT:PSS/$CH_3NH_3PbI_3$ and semi-finished aged films of ITO/PEDOT:PSS/$CH_3NH_3PbI_3$/$PC_{70}BM$/AZO device structures at 85°C for 96 hours. The best performing photovoltaic parameters of the aged device structures completed with fresh $PC_{70}BM$/AZO/Al and Al respectively were compared with the values of fresh (not-degraded) reference devices. The results are shown in Table 4-1.

TABLE 4-1. Photovoltaic parameters for fresh reference and buffer layer engineered devices.

Device type	**V_{oc} (V)**	**J_{sc} (mA/cm^2)**	**FF (%)**	**PCE (%)**
Fresh reference device	0.91	14.75	79.2	10.64
Aged ITO/PEDOT:PSS/$CH_3NH_3PbI_3$ and fresh $PC_{70}BM$/AZO/Al	0.89	15.13	67.3	9.03
Aged ITO/PEDOT:PSS/$CH_3NH_3PbI_3$/$PC_{70}BM$/AZO and Fresh Al	0.84	16.43	73.2	10.10

From Table 4-1 aged device structures (ITO/PEDOT:PSS/$CH_3NH_3PbI_3$ and aged ITO/PEDOT:PSS/$CH_3NH_3PbI_3$/$PC_{70}BM$/AZO at 85 °C for 96 hours with fresh $PC_{70}BM$/AZO/Al and fresh Al retain their photovoltaic performance with minor losses compared to the fresh reference devices. This further highlight the intrinsic stability of $MAPbI_3$ and the significant role that the top electrode interaction with the perovskite active layer plays for the stability of the device. If we compare the device structures which were fabricated using aged $MAPbI_3$ with the aged devices of Figure 4-2, aging the $MAPbI_3$ doesn't play a significant role to the degradation of the device since at 96 hours the PCE drops below ~20% of its initial value, whereas the device structures (with aged active layer and fresh $PC_{70}BM$/AZO/Al) retained most of their initial PCE value. A similar behavior is observed when fresh Al was evaporated within an aged ITO/PEDOT:PSS/$CH_3NH_3PbI_3$/$PC_{70}BM$/AZO device structure. The resulting devices, like before, exhibit a very similar behavior comparable to our non-degraded fresh reference devices. From the above experimental buffer layer device engineering observations, we conclude that the devices degrade only upon the incorporation of Al during the thermal aging test and therefore the interaction of the perovskite active layer with the top metal electrode is the major degradation pathway for this type of device, whereas the perovskite itself or its interaction with any subsequent interlayers plays no significant role in the heat stability of the devices.

Two mechanisms are proposed that could be related to the degradation of the devices: i) migration of halide ions to the Al metal and ii) migration of Al atoms to the $MAPbI_3$. Both these mechanisms were also observed by Fang et. al where migration of I^- towards the Ag electrode as well as migration of Ag atoms into the $MAPbI_3$ manifested under ambient humidity and light soaking for 200h. [41] In particular, diffusion of I^- is common in such devices due to the small activation energy (~0.1 eV) [112] and high concentration gradient (10^{26} cm^{-4}) which is further accelerated at higher temperatures as we have already discussed. [113] Diffusion of I^- is often facilitated by the decomposition of the perovskite layer. During decomposition of the perovskite layer to lead iodide (PbI_2), methyl ammonium (MA) and hydrogen iodide (HI), MA and HI can escape the surface of the perovskite leaving behind iodide vacancies which promote the diffusion of I^- [113] . Metal ions have also been reported to migrate towards the perovskite under accelerated heat conditions. Domanski et. al have recently reported that upon heating at 70 ^{o}C, Au atoms can travel through spiro-MeOTAD HTL and migrate towards the perovskite layer, remarkably affecting the device performance. [51] The direct contact of the perovskite layer with metal electrodes like Ag has also been previously reported to be very damaging for the device performance even at ambient conditions [82] due to the chemical interaction between the two materials. Therefore, the isolation of these two layers is of utmost importance. Al and other commonly used electrode metals (Au, Ag and Ca) have been previously reported to penetrate fullerene layers even in the process of evaporation. This increases the probability of such metal and the perovskite layer to come in direct contact with each other chemically reacting. [114] This chemical reaction between the metal electrodes and perovskite leads to a change to the perovskite film color from dark brown to yellow due to the decomposition to PbI_2. [113] Figure 4-6 shows devices presented within this work: a) bottom side of fresh device stack, b) bottom side of thermally aged device stack of thin-$PC_{70}BM$ based devices, c) bottom side of thermally aged devices stack of thick-$PC_{70}BM$ based devices, d) the top side of fresh device stack, e) top side of thermally aged device stack of thin-$PC_{70}BM$ based devices, f) top side of thermally aged devices stack of thick-$PC_{70}BM$ based devices .

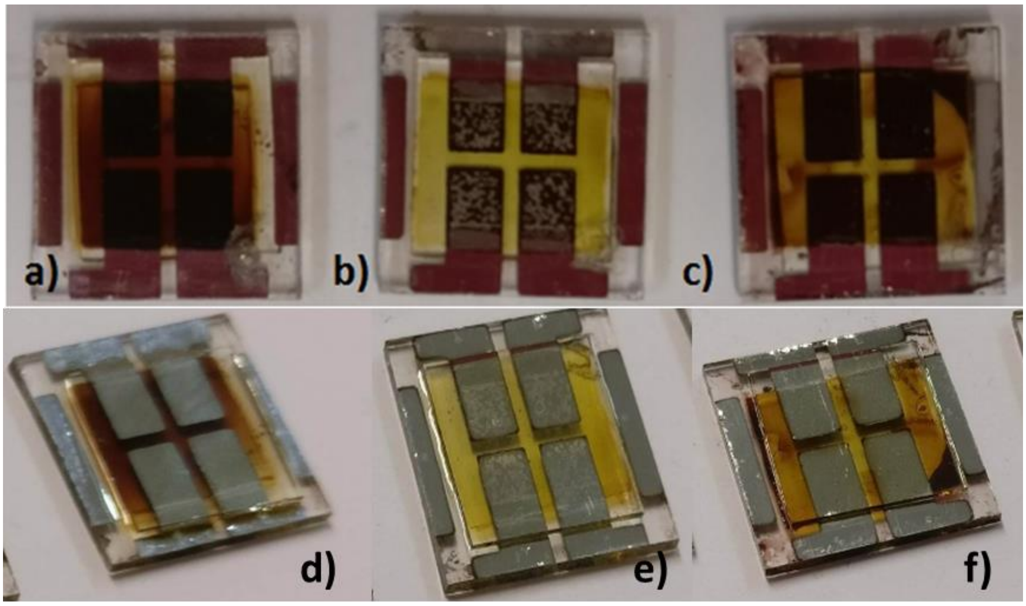

Figure 4-6: a) Bottom side of fresh device stack, b) bottom side of thermally aged device stack of thin-$PC_{70}BM$ based devices, c) bottom side of thermally aged devices stack of thick-$PC_{70}BM$ based devices, d) top side of fresh device stack, e) top side of thermally aged device stack of thin-$PC_{70}BM$ based devices, f) top side of thermally aged devices stack of thick-$PC_{70}BM$ based devices

From Figure 4-6a we can see that the perovskite film in thin-$PC_{70}BM$ based devices exhibited a color change from dark brown to yellow, indicating decomposition to PbI_2, upon thermally aging the whole device stack at 85°C and N_2 similar to previously reported observations. [113] On the contrary the perovskite retains its color at a respectable degree for devices incorporating thick $PC_{70}BM$ (Figure 4-6c). Furthermore metallic-like spots start to appear in the thin-$PC_{70}BM$ based devices located at the bottom side of the device which were absent from both the fresh and thick-$PC_{70}BM$ based devices. Since the ITO/PEDOT:PSS/$CH_3NH_3PbI_3$ film has shown non- detectable signs of decomposition from the XRD and absorption spectra measurements, the color change from dark brown to yellow upon aging alongside the Al electrode could be a result of Al diffusion towards the active layer. The top side of the thin $PC_{70}BM$ device also shows some change in the color of Al electrode where it became less shiny and whiter (Figure 4-6e). This is an indication of Al corrosion due to diffusion of I^- as previously reported. [113] Both the fresh (Figure 4-6 d) and aged thick-fullerene based devices (Figure 4-6f) do not show any apparent change in the Al electrode.

Recently reported time of flight secondary ion mass spectroscopy (ToF-SIMS) measurements have shown metal diffusion of air stable metal such as Au in a Cs containing $FA_{0.83}MA_{0.17}Pb(I_{0.83}Br_{0.17})_3$ formulation [51]. As already mentioned above, degradation due to diffusion of I^- is often a result of the intrinsic decomposition of the perovskite layer and introduction of iodine vacancies in the process. Even though decomposition of the perovskite layer was not detectable, in the process of characterization via XRD (from the introduction of PbI_2 peaks) [97] and reduction of the absorption spectra, [113] it can still be present but less evolved. [48] As it is reported in the buffer layer engineering section, aging the semi-finished ITO/PEDOT:PSS/$CH_3NH_3PbI_3$ and ITO/PEDOT:PSS/$CH_3NH_3PbI_3$/$PC_{70}BM$/AZO device stacks does not play a detrimental role to the PV parameters of the fabricated device. In a recent work Akbulatov et. al have shown that similar device structures of ITO/PEDOT:PSS/$CH_3NH_3PbI_3$/$PC_{60}BM$/Ag can easily degrade under open circuit conditions, constant illumination at70 mW/cm^2 and 60 ^oC thermal aging even in inert conditions [115]. Through ToF SIMS and theoretical calculations it was shown that the degradation had occurred through liberation of volatile MAI and formation of AgI in the Ag electrode. It was also reported through ToF SIMS that the Ag electrode showed some sign of penetration inside the $PC_{60}BM$ upon aging. [115] From the experiments so far, we have shown that thick fullerene-based buffer layers can be used to block diffusion and improve the thermal stability of inverted perovskite PVs.

4.5 Device Lifetime of devices based on $PC_{70}BM$, $PC_{70}BM$/AZO and $PC_{70}BM/\gamma\text{-}Fe_2O_3$ top electrodes

As previously mentioned, the main degradation pathway for p-i-n PSCs lies at the top electrode and is related to the interaction of the active layer with the Al metal electrode. To understand these results in more detail, we proceeded in studying the effect of three different ETLs ($PC_{70}BM$, $PC_{70}BM$/AZO and the novel $PC_{70}BM$/γFe2O3) in the lifetime performance of p-i-n PSCs. To prepare the $\gamma\text{-}Fe_2O_3$ solution we have used solvothermal colloidal synthesis in conjunction with ligand-exchange method to isolate uniform $\gamma\text{-}Fe_2O_3$ NPs well-dispersed in polar solvents. Using transmission electron microscopy (TEM) we have calculated the size of the $\gamma\text{-}Fe_2O_3$ to be ~5.5 nm. $\gamma\text{-}Fe_2O_3$ NPs were synthesized and characterized by Dr. Ioannis Papadas of the MEP group. Detailed NP synthesis as well as material characterization can be found in our recent submitted paper.[116] Thin films of γ-Fe_2O_3 NPs were spin casted next on top of $PC_{70}BM$ and quartz substrates using the spin coating technique. Figure 4-7 displays the surface topography of a 20 nm-tick film of γ-Fe_2O_3 NPs fabricated on top of $PC_{70}BM$ and quartz substrates, respectively, as obtained by AFM line scans. On top of $PC_{70}BM$ the surface roughness is ~5 nm, which is comparable with the roughness obtained by plain $PC_{70}BM$ as well as $PC_{70}BM$/AZO films. The γ-Fe_2O_3 film fabricated on quartz substrate exhibits a smooth and compact topography of only ~4.3 nm roughness. It should be stressed that the development of a low roughness layer is beneficial for the photovoltaic perovskite solar cells (PVSCs) performance.

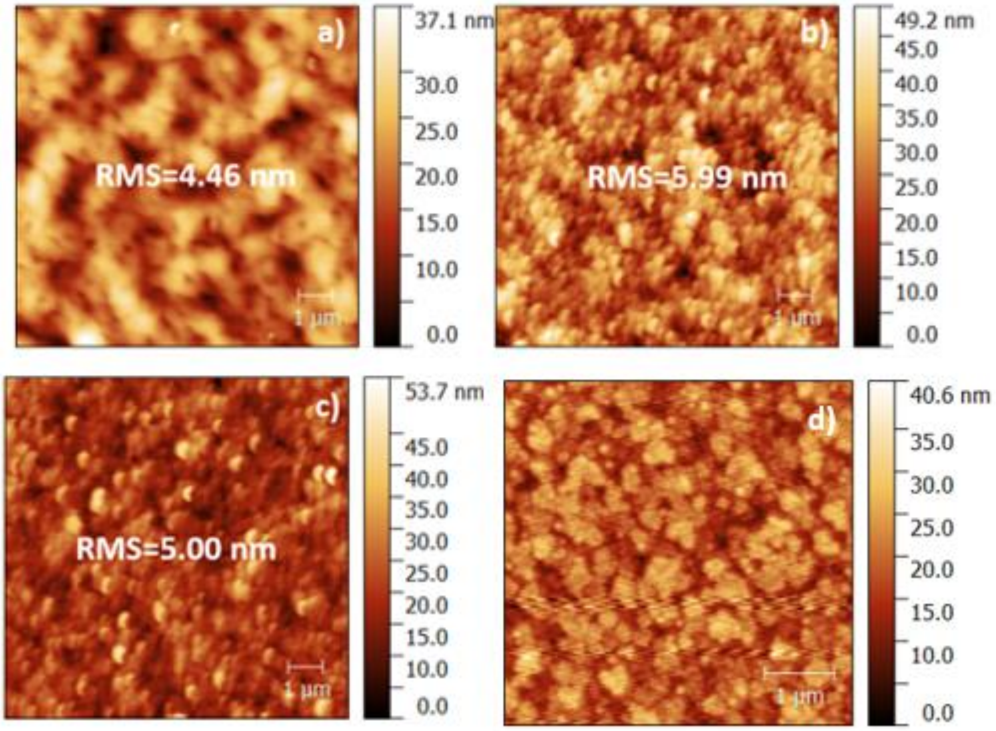

Figure 4-7: AFM data in 10x10 µm magnification for a) ITO/PEDOT:PSS/ $CH_3NH_3PbI_3/PC_{70}BM$, b)ITO/PEDOT:PSS/$CH_3NH_3PbI_3$/PC70BM/AZO c) ITO/PEDOT:PSS/ $CH_3NH_3PbI_3/PC_{70}BM$/γ-Fe_2O_3 films, d) AMF data in 5x5 µm magnification for γ-Fe_2O_3 film on quartz substrate

To test the effectiveness of γ-Fe_2O_3 nanoparticulated ETL for inverted structured PVSCs, completed devices were fabricated based on the general inverted device structure

ITO/PEDOT:PSS (~30 nm)/$CH_3NH_3PbI_3$ (~300 nm)/ETL/Al (~100 nm), where the three different ETLs under investigation were compared: $PC_{70}BM$ (~70 nm), $PC_{70}BM$/AZO (~40 nm) and $PC_{70}BM/Fe_2O_3$ (~20 nm). A schematic representation of the device structure is shown in Figure 4-8a. The use of γ-Fe_2O_3 in conjunction with $PC_{70}BM$ was found to have minor impact towards the PCE of p-i-n structured devices since the PCEs were comparable both to $PC_{70}BM$ as well as $PC_{70}BM$/AZO. This is further highlighted in the energy level diagram shown in Figure 4-8b, which is based on measured values of the literature.[117, 118] The representative values of PV parameters from a total of 10 devices from each structure, that described in detail above, are summarized in Table 4-2.

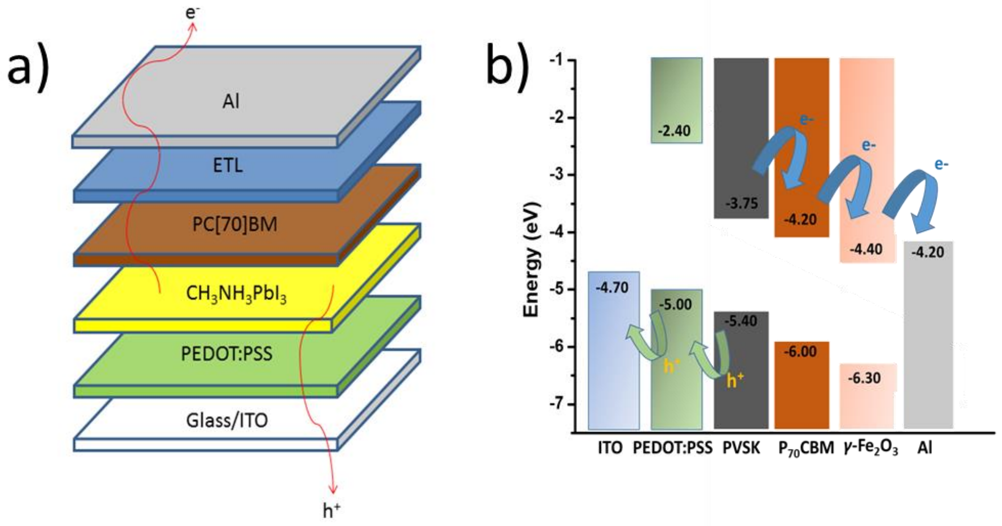

Figure 4-8. a) Schematic representation of the device structure used and b) the corresponding energy level diagram under study.

As previously noted, by using γ-Fe_2O_3 in conjunction with $PC_{70}BM$ as the ETL instead of plain $PC_{70}BM$ or $PC_{70}BM$/AZO appears to have no significant effect to the device PCE performance (only a slight drop in FF, from 75 to 70%, was observed). It is important to note that the focus of this work was to inspect the effect of γ-Fe_2O_3 as solution processed ETL in terms of stability of the inverted PVSCs and not achieving the highest possible PCE. For the same reasoning we chose to use widely used and understood materials such as PEDOT:PSS as the HTL and a basic perovskite $CH_3NH_3PbI_3$ formulation for the inverted PVSCs, despite the lower PCEs the device structure and perovskite formulation used within this work offers high reliability and reproducibility essential parameters for fabricated devices for lifetime studies. The experimental results presented were consistent on several experimental runs.

Table 4-2. Photovoltaic parameters for the three different device architectures.

Device architecture	V_{OC} (V)	J_{SC} (mA/cm^2)	FF (%)	PCE (%)
ITO/PEDOT:PSS/$CH_3NH_3PbI_3$/$PC_{70}BM$/Al	0.84	15.41	75	9.68
ITO/PEDOT:PSS/$CH_3NH_3PbI_3$/$PC_{70}BM$/γ-Fe_2O_3/Al	0.88	16.53	69.7	10.13
ITO/PEDOT:PSS/$CH_3NH_3PbI_3$/$PC_{70}BM$/AZO/Al	0.85	15.40	74.4	9.72

The effect of using a thin (~20 nm) γ-F_2O_3 based interfacial layer on the heat accelerated lifetime performance of inverted PVSCs is studied following the previous experiments. The accelerated heat lifetime performance of inverted PVSCs incorporating γ-Fe_2O_3 within the top electrode ($PC_{70}BM$/Fe_2O_3/Al) has been compared with the more conventional $PC_{70}BM$/Al and $PC_{70}BM$/AZO/Al inverted PVSCs top electrodes. The conditions for the lifetime experiments were 60 ^{0}C and N_2 atmosphere under dark for all PVSCs presented within the work. The normalized lifetime plots were constructed from the average PV parameters of 10 devices for each architecture and the results which are listed in Figure 4-9 where consistent on several lifetime runs under the conditions described within this work.

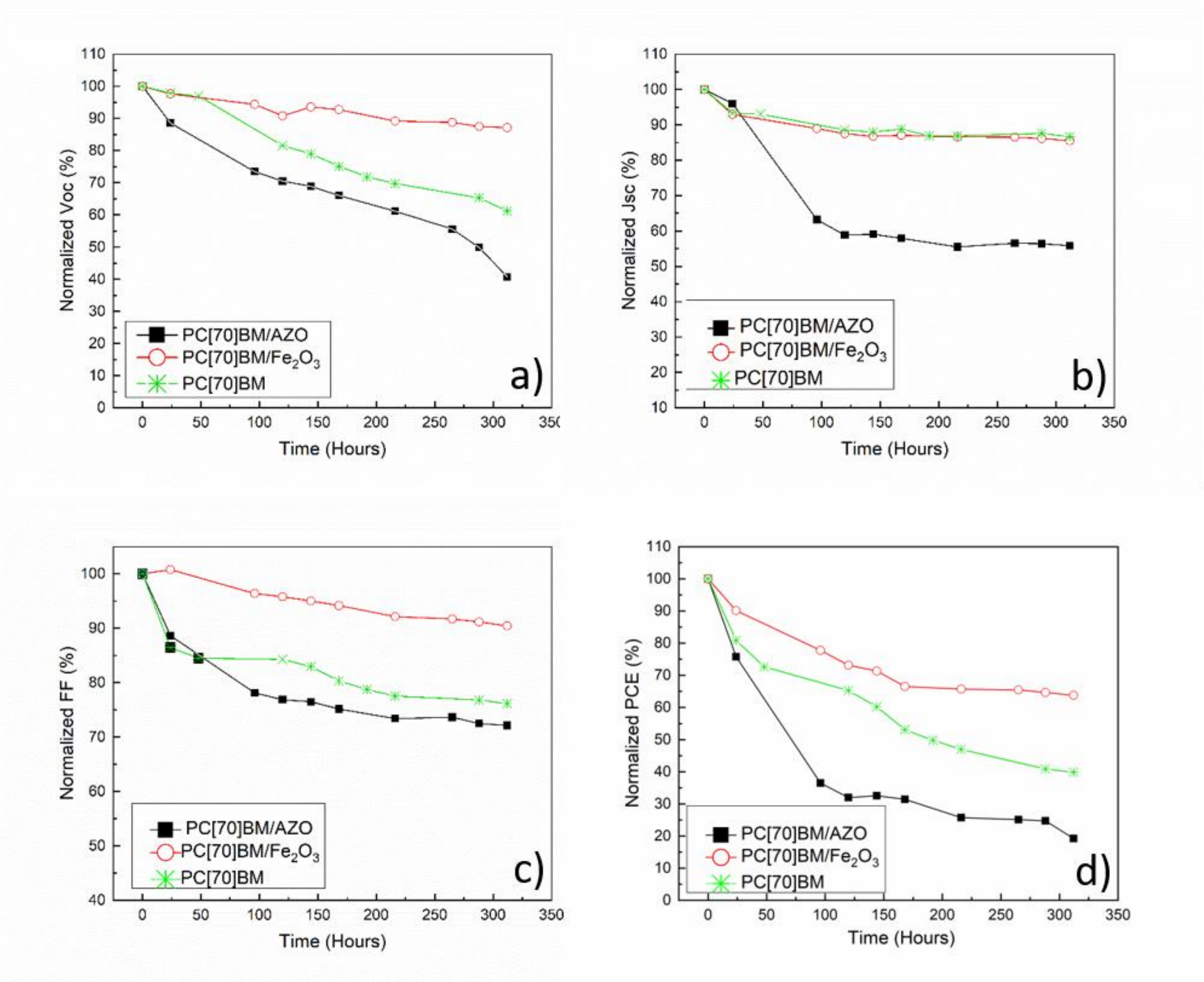

Figure 4-9. Normalized a) V_{OC}, b) Jsc, c) FF and d) PCE for three different ETLs.

From the lifetime plots there are some considerable differences between the behavior of the three different (top electrode) inverted PVSCs device architectures. The PV parameters of the PVSCs incorporating γ-Fe_2O_3 within the top electrode ($PC_{70}BM/Fe_2O_3/Al$) show considerable improvement in stability compared to devices based on $PC_{70}BM/Al$ and $PC_{70}BM/AZO/Al$ top electrode. Specifically, $PC_{70}BM/Fe_2O_3/Al$ based device has T_{80} (the time the PCE reached 80% of its initial fabrication value) at 100 hours of operation and has even retained 70% of their PCE after 300 hours of testing, whereas device with $PC_{70}BM/Al$ has T80 at 24 hours and the PCE settled at the lowest value of 40% of their original PCE when the aging test has reached

300 hours. The device with PC$_{70}$BM/AZO/Al has dropped to 70% at the first 24 hours of aging, reaching below 40% at the 100 hours mark and has settled even lower at 15% when the aging test has reached the 300 hours. Figure 4-9 shows that V_{OC} and J_{SC} in the PC$_{70}$BM/AZO/Al based inverted PVSCs shown the strongest drop under the heat accelerated lifetime condition presented within this work.

4.6 Device characterization of p-i-n perovskite solar cells incorporating PC$_{70}$BM, PC$_{70}$BM/AZO and PC$_{70}$BM/γ-Fe$_2$O$_3$ top electrode

Complementary to the heat accelerated lifetime test, we have conducted characterization studies on representative devices for the three device architectures at the 168 hours mark. This point for characterization is chosen since it lies in the middle of the aging test and thus it would ensure that the devices showed significant differences between them while still being eligible for testing and completely degraded from the aging test. In particular, the devices were characterized using illuminated and dark J-V measurements as well as Mott-Schottky analysis.

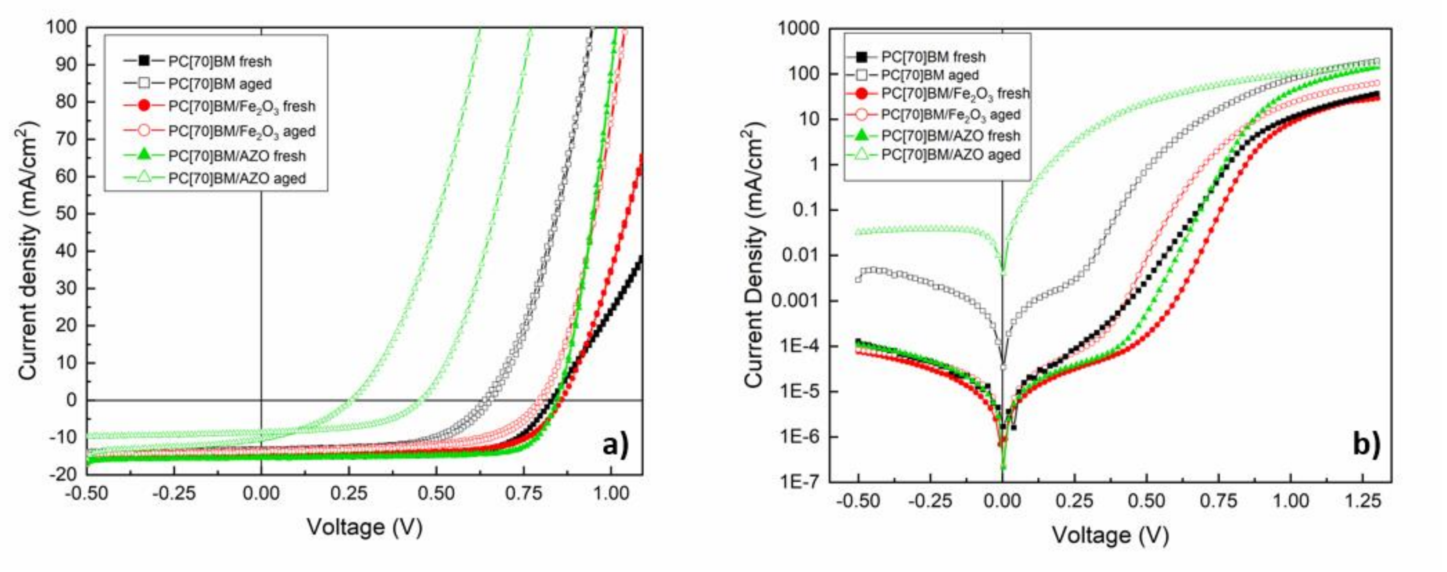

Figure 4-10. a) Illuminated J-V characteristics and b) dark J-V characteristics, respectively.

Figure 4-10a depicts the illuminated J-V characteristic for the three device architectures. The V_{OC} change with respect to aging is very clearly observed. In particular, the device based on $PC_{70}BM/AZO/Al$ shows a very sharp drop to V_{OC}, indicated by the shift of the J-V curve to the left. There is also a very significant sign of hysteresis in this device which could be attributed to charge traps or ion migration manifesting through the aging test. [25] Both inverted PVSCs architectures using $PC_{70}BM/Al$ and $PC_{70}BM/Fe_2O_3/Al$ show negligible signs of hysteresis. However, the devices without γ-Fe_2O_3 interface modification ($PC_{70}BM/Al$) show a significant drop to V_{OC} (although not as severe as in $PC_{70}BM/AZO/Al$ based inverted PVSCs), while inverted PVSCs using $PC_{70}BM/Fe_2O_3/Al$ provide clearly more stable V_{OC} values under heat accelerated lifetime conditions. Dark J-V plots are shown in Figure 4-10b. Devices with $PC_{70}BM/AZO/Al$ top electrode show significantly reduced parallel resistance (Rp) and increased leakage current after aging compared to the other two top electrode architectures under investigation. Furthermore, the diode characteristic is completely lost in devices with $PC_{70}BM/AZO/Al$ top electrode. In comparison, the device with $PC_{70}BM/Al$ has also shown a decrease to Rp and increase in leakage current, although not as severe as the $PC_{70}BM/AZO/Al$ based inverted PVSCs. Importantly, the inverted PVSCs with $PC_{70}BM/Fe_2O_3/Al$ top electrodes show almost no change after aging in regard to Rp and leakage current (a parameter which is shown the quality of the inverted PVSCs incorporating the proposed γ-Fe2O3 interface modification). Both devices with $PC_{70}BM$ and $PC_{70}BM/Fe_2O_3$ ETLs seem to retain the diode characteristic after aging. This trend follows the observation of V_{OC} drop, where devices with decreased Rp and increased leakage current also show a proportional drop to their V_{OC}.

Apart from the two degradation mechanisms that we have previously reported for p-i-n PSCs (diffusion of halide ions to the metal electrode and diffusion of metal atoms to the $CH_3NH_3PbI_3$), another major concern that has been recently placed is the negative effect that doping can have in the stability of PSCs. Recently a comprehensive study was performed by N. Tessler and Y. Vaynzof using a model solar cell system based on electron-ion conducting perovskite active layer. In that work it was shown that undoped charge selective layers (CSLs) can be used to significantly decrease the voltage drop across the perovskite active layer and therefore suppress the ion accumulation through the device, preventing hysteresis and degradation of perovskite solar cells.[47] In contrary using doped CSLs the potential drop across the perovskite active layer was reported to be significantly larger compared to undoped CSLs and therefore the suppression of ion accumulation is expected to be less efficient. [119]Although in this case we compare two ETLs that one is doped (AZO) and another that is undoped (Fe_2O_3), it is worth mentioning the role of the $PC_{70}BM$ passivation/buffer layer that lies between the AZO and the perovskite active layer. Since The $PC_{70}BM$ layer is inherently undoped, ion accumulation doping degradation issues related to AZO should not be dominant. [119] The fact that devices with AZO have shown the worst stability led us to search for a different explanation. The instability of AZO in p-i-n PSCs has also been previously reported by K. Brinkmann et. al [97] It is reported in several works that ZnO can negatively impact the stability of $CH_3NH_3PbI_3$ upon annealing through the deprotonation of MA^+ caused by residual OH^- on the ZnO nanoparticles surface that are often present. It was also reported that PCBM as a buffer layer can reduce, but not completely avoid this decomposition. [120], [121] This correlates with our observation from the lifetime plots in Figure 4-9b, showing a drop in J_{sc} for devices with AZO, pointing towards the degradation of the active layer whereas both $PC_{70}BM$ and $PC_{70}BM/Fe_2O_3$ show negligible drop to J_{sc}.

A crucial factor for the stability and the quality of halide perovskite crystallization is the acidic or basic character of the metal oxides, which are used as HTLs or ETLs in the perovskite solar cells (PVSCs). The acidic or basic nature of metal oxides depends on the corresponding isoelectric point (IEP). It has been observed that these hydroxyl groups on the interfaces of metal oxides with basic nature cause decomposition of the hybrid halide perovskite through the deprotonation of the methylamine, leading to PbI_2. This decomposition mechanism is not observed in more acidic metal oxides (such as TiO_2 and ITO). [122] In the literature, γ-Fe_2O_3 NPs interfaces are typically acidic (with isoelectric points in the range of 5.5−6.7), [123] whereas ZnO NPs interfaces tend to be more basic (with isoelectric points >8.7).[124] This suggests that deprotonation of the MA^+ (pKa of ∼10.6) by the ZnO surface may be a possible cause of the thermal decomposition, [125] in contrast with more acidic surface nature of γ-Fe_2O_3 NPs films which produce more thermally stable perovskite films.

Using Mott-Schottky analysis we have tried to understand why the incorporation of $PC_{70}BM/Fe_2O_3$ as the ETL has resulted in better stability compared to plain $PC_{70}BM$. Mott-Schottky analysis has been previously utilized for the quantification of charge traps in PSCs by studying response of charged carriers to the AC signal that is applied in the CV measurement. When using relatively high frequencies (HF) at ~100 kHz only free charges at the conduction band (Ec) can follow the AC voltage perturbation applied in CV measurements and can contribute to the EV_{BI} value. When the frequency is dropped to low frequencies (LF) at ~500 Hz we are effectively approaching DC conditions, where de-trapping of charges can occur and therefore contribute to EV_{BI} and as a result to V_{OC}. [126] Therefore, the presence of trapped charges can contribute to the overall EV_{BI} value, effectively altering it, depending on the frequency used for the Mott-Schottky analysis. [127] Using this information we have performed a comparative study where the EV_{BI} change between HF and LF was correlated with the population of traps inside freshly prepared devices. From Figures 4-11a and 4-11b we have used linear interpolation to extract the value of EV_{BI} from the point of intercept of the linear part in the Mott-Schottky plot with the x-axis. Some clear differences are observed in the values of EV_{BI} shown in Table 4-3. First by comparing the EV_{BI} drop of fresh devices incorporating plain $PC_{70}BM$ with $PC_{70}BM/Fe_2O_3$ and $PC_{70}BM/AZO$ we see that they exhibit the largest drop at 0.73 V compared to 0.40 V and 0.30 V for the $PC_{70}BM/Fe_2O_3$ and $PC_{70}BM/AZO$, respectively. This suggests that there is a larger population of charge traps in fresh devices with $PC_{70}BM$ compared to $PC_{70}BM/Fe_2O_3$ and $PC_{70}BM/AZO$.

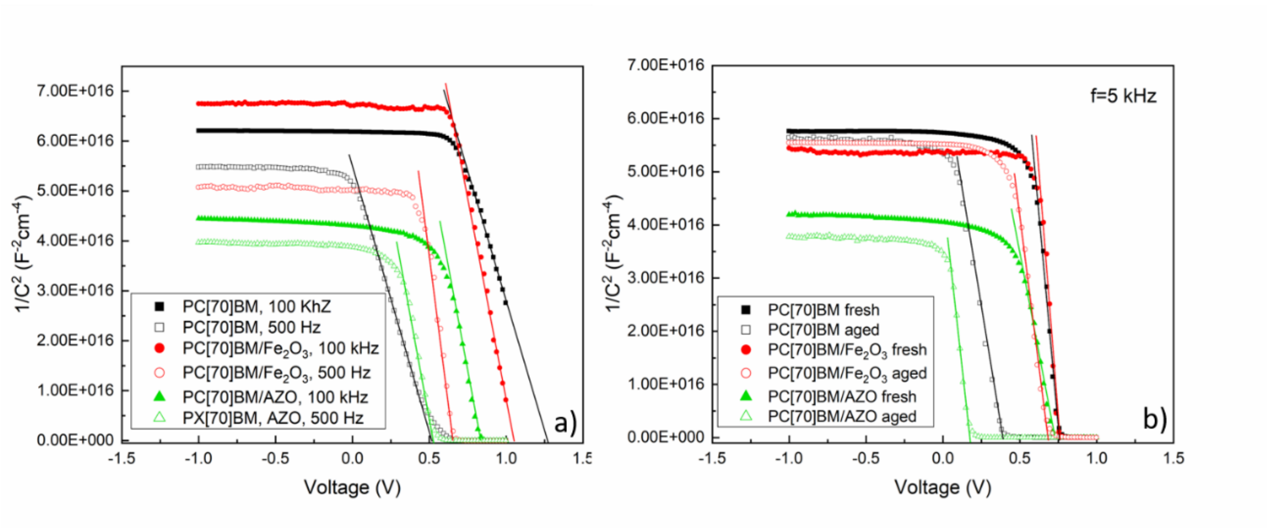

Figure 4-11. a) Mott Schottky plots of fresh devices at f=100 kHz and f=500 Hz and b) fresh and aged devices at f=5 kHz.

Since the only change in the device structure was in the top electrode, the hypothesis that the traps are present in the $PC_{70}BM$/Al interface is made and by incorporating either AZO or Fe_2O_3 we can fabricate a more efficient interface with the top metal contact. Identifying the exact nature and direct position of charge traps would require further complex characterization techniques and therefore was beyond the scope of this work. Charge traps were reported to negatively impact the stability of PSCs from the induction of local electric field. [128] Although AZO also seems to facilitate in the more efficient interface between the ETL and metal electrode like Fe_2O_3, the interaction of ZnO with $CH_3NH_3PbI_3$ yields the worst stability as we have previously stated. It is also worth stating that by using Fe_2O_3 on top of PC70BM any surface defects of inconsistent film coverage from the $PC_{70}BM$ film would be passivated from the Fe_2O_3 film, which would improve the stability of devices further.

Table 4-3. Extracted built in voltage (EV_{BI}) voltage drop between HF-LF of fresh devices and fresh-aged devices.

Device architecture	EV_{BI} drop between HF and LF of fresh devices (V)	EV_{BI} drop between fresh and aged devices (V)
ITO/PEDOT:PSS/$CH_3NH_3PbI_3$/$PC_{70}BM$/Al	0.73	0.39
ITO/PEDOT:PSS/$CH_3NH_3PbI_3$/$PC_{70}BM$/Fe_2O_3/Al	0.40	0.09
ITO/PEDOT:PSS/$CH_3NH_3PbI_3$/$PC_{70}BM$/AZO/Al	0.30	0.53

To evaluate the EV_{BI} drop between fresh and aged devices the frequency is kept constant at f = 5 kHz. When choosing an appropriate frequency for Mott-Schottky analysis it should usually coincide in the high frequency plateau of the relevant capacitance frequency (CF) plot. [129] It is also noted that at 5 kHz the EV_{BI} value for all three device architectures under investigation is similar, which agrees with their similar measured V_{OC} values. CF measurements were performed using this particular perovskite formulation, fabricating devices with the general structure ITO/PEDOT:PSS/$CH_3NH_3PbI_3$/$PC_{70}BM$/AZO/Al in our previous work and therefore 5 kHz is an appropriate choice for our particular measurements. [84] After aging, the trend in EV_{BI} drop at 5 KHz correlates well with the V_{OC} drop that we see in the lifetime plots from Figure 5-5a, where the smallest EV_{BI} drop is observed by devices incorporating $PC_{70}BM$/Fe_2O_3/Al at 0.09 V followed by $PC_{70}BM$/Al at 0.39 V, whereas the $PC_{70}BM$/AZO/Al devices exhibit the largest EV_{BI} drop at 0.53 V. Through the impedance spectroscopy measurements, the intimate interface of Fe_2O_3 with the top electrode is highlighted, resulting in decreased trap density and therefore improved stability under accelerated heat conditions, primarily due to the stable V_{OC} behavior.

4.7 Incorporation of Fullerene based diffusion blocking layer on $CH_3NH_3PbI_{3-x}Cl_x$ based devices to improve thermal stability.

As indicated above diffusion mechanisms are the dominant degradation pathway that affected the thermal stability of perovskite solar cells. Thus, incorporation of diffusion blocking layers within the device architecture is expected to improve lifetime performance. Using a 200 nm thick $PC_{70}BM$ diffusion blocking layer we were able to isolate the $CH_3NH_3PbI_3$ active layer from the metal electrode, a procedure that effectively improves the lifetime performance of device upon heating at 85 ^oC from 24 hours to over 168 hours. This improved stability, however, is attained at the cost of strong PCE reduction due to the thick $PC_{70}BM$ fullerene-based buffer layer used for the isolation of the perovskite active layer from the top metal electrode. To improve the stability of devices and reduce the observed efficiency-stability gap by incorporation of $PC_{70}BM$ diffusion blocking layer to inverted perovskite solar cells, the behavior of the proposed thick diffusion blocking layer is tested to devices with $CH_3NH_3PbI_{3-x}Cl_x$ as the active layer that are optimized to work effectively with thick PC70BM. Typically, devices based on $CH_3NH_3PbI_{3--x}Cl_x$ produce perovskite films with high roughness (Rms~12.45 nm) compared to the previously used $CH_3NH_3PbI_3$ formulation that produces films with relatively low roughness (Rms~4.21 nm), as shown in the AFM phase contrast measurements in Figure 4-12. The thicker $PC_{70}BM$ is therefore necessary to ensure uniform coverage of the rough perovskite films.

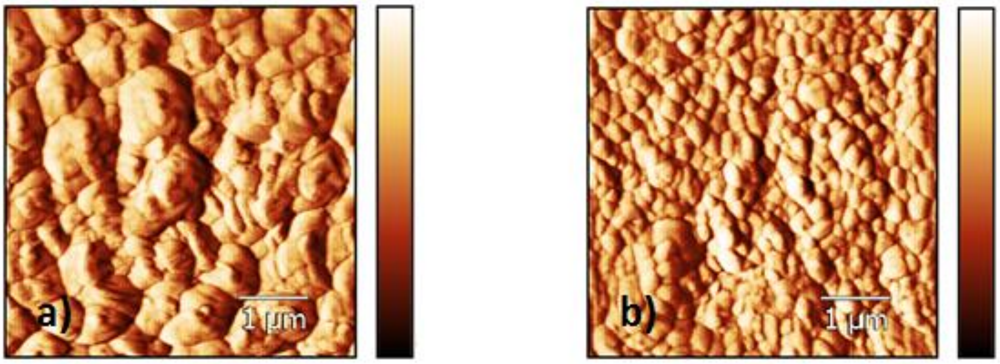

Figure 4-12: 5x5 µm AFM measurements for a) $CH_3NH_3PbI_{3-x}Cl_x$, b) $CH_3NH_3PbI_3$ perovskite films

The structure of the devices under study was based on the previously studied configuration of ITO/PEDOT:PSS/$CH_3NH_3PbI_3$/$PC_{70}BM$/AZO/Al. Since the fullerene diffusion blocking layer used was thick (200 nm) we decided to work to still incorporate AZO rather than Fe_2O_3 due to its higher conductivity. Furthermore, we also chose to incorporate AZO instead of plain $PC_{70}BM$ since $CH_3NH_3PbI_{3-x}Cl_x$ was previously reported to show improved PCE by the incorporation of AZO on top of the $PC_{70}BM$.[26]

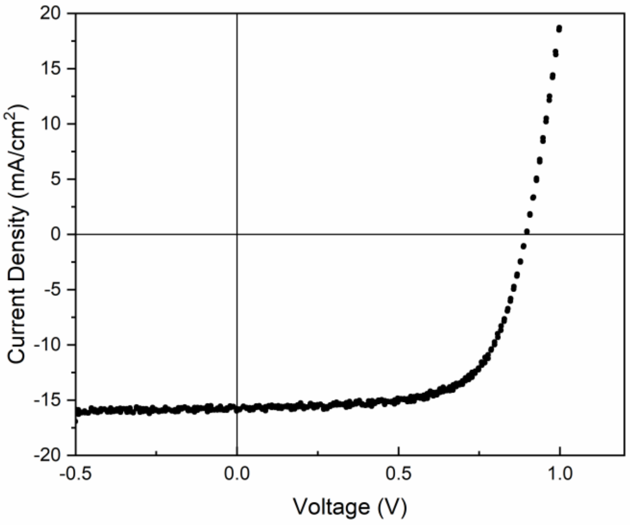

Figure 4-13: Illuminated J/V plot of the champion $CH_3NH_3PbI_{3-x}Cl_x$ based device using thick $PC_{70}BM$ diffusion blocking layer.

Using $CH_3NH_3PbI_{3-x}Cl_x$ and thick (200 nm) diffusion based $PC_{70}BM$ blocking layer have devices with V_{OC}=0.90 V, J_{SC}=15.79 mA/cm^2, FF= 66.8 % and PCE= 9.48 % are achieved which is shown in Figure 4-13.

The heat stability of these devices was evaluated and compared with the efficient $CH_3NH_3PbI_3$ based devices using optimized for efficiency thin (70 nm) fullerene electron transporting layer (ETL). The lifetime profile of the average normalized PV parameters from 8 devices of each device set is shown in Figure 4-14**.** It is observed that the devices which are based on $CH_3NH_3PbI_{3-x}Cl_x$ s with thick $PC_{70}BM$ show impressive heat stability even with the incorporation of AZO for up to 1000h. It has been reported that $CH_3NH_3PbI_{3-x}Cl_x$ exhibits better intrinsic stability over other perovskite formulations such as $CH_3NH_3PbCl_3$ and $CH_3NH_3PbI_{3.}$ [68] It is important to note that based on the experimental conditions used within this work we have not observed any major intrinsic degradation of the $CH_3NH_3PbI_3$ from the XRD and UV-Vis. Furthermore, it is shown using buffer layer device engineering experimental methods that using thermally aged $CH_3NH_3PbI_3$ and fresh top electrode yields almost no change to the efficiency parameters of the device compared to a fresh-reference device. Therefore, we believe that the improved stability of the $CH_3NH_3PbI_{3-x}Cl_x$ based devices is due to the incorporation of the thick $PC_{70}BM$ buffer layer that can be used to eliminate top electrode thermally activated degradation mechanisms of p-i-n inverted perovskite photovoltaics.

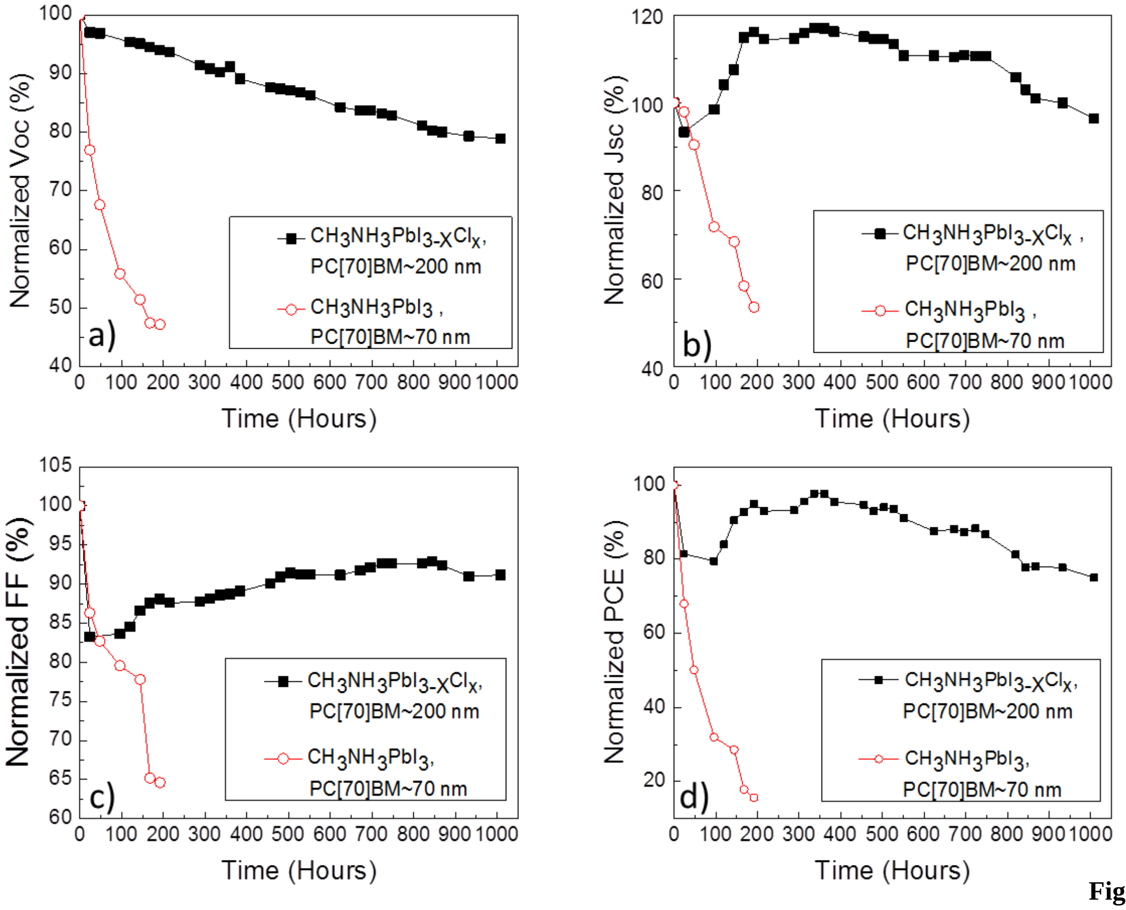

Figure 4-14: Normalized a) V_{OC}, b) J_{sc}, c) FF and d) PCE of $CH_3NH_3PbI_3$ and $CH_3NH_3PbI_{3-x}Cl_x$ based devices over 1000 hours of heating at 60 °C and N_2.

4.8 Summary

It is proposed that the interaction of the Al metal electrode with the perovskite active layer through diffusion mechanisms is the main thermal degradation mechanism for inverted perovskite solar cell. Using a 200 nm thick $PC_{70}BM$ ETL the $CH_3NH_3PbI_3$ active layer is isolated from the metal electrode, a procedure that effectively improves the lifetime device performance upon accelerating lifetime heating at 85 ^{o}C from 24 hours to over 168 hours. This improved stability however is attained at the cost of reduced PCE due to the thick $PC_{70}BM$ fullerene buffer layer used for the isolation of the $CH_3NH_3PbI_3$ active layer from the top Al metal electrode. It is shown that colloidal synthesized γ-Fe_2O_3 can be effectively used to provide solution processed nanoparticulate interfacial layer for the top electrode of inverted PVSCs. Inverted PVSCs with $PC_{70}BM/Fe_2O_3/Al$ top electrode yield comparable PCE value to the more conventional inverted PVSCs top electrodes such as $PC_{70}BM/Al$ and $PC_{70}BM/AZO/Al$. The proposed inverted PVSCs γ-Fe_2O_3 top electrode interface modification ($PC_{70}BM/Fe_2O_3/Al$) results in improved stability under accelerated heat conditions at 60 ^{o}C and N_2 atmosphere. On the contrary $PC_{70}BM/AZO/Al$ device has shown the worst stability due to the deprotonation of MA^+ induced by the basic nature of AZO compared to more acidic γ-Fe_2O_3 interface modification ($PC_{70}BM/\gamma$-Fe_2O_3/Al). Overall, $PC_{70}BM/\gamma$-Fe_2O_3/Al results in less population of charge traps that lie in the $PC_{70}BM/Al$ interface and, therefore, γ-Fe_2O_3 interface modification provides a better top electrode for inverted PVSCs. To reduce the efficiency–stability gap of perovskite photovoltaics, the proposed diffusion blocking layer is evaluated using $CH_3NH_3PbI_3$-xClx based devices that are optimized to work effectively with thick $PC_{70}BM$. A hysteresis free $CH_3NH_3PbI_{3-x}Cl_x$ inverted perovskite PVs with thick $PC_{70}BM$ diffusion blocking layer that exhibit PCE in the range of 10 % and thermal stability for over 1000 hours at 60 ^{o}C is presented.

5 HIGH PERFORMANCE INVERTED PEOVSKITE SOLAR CELLS INCORPORATING DOPED FULLERENE DIFFUSION BLOCKING LAYER

5.1 Abstract

Inverted p-i-n hybrid organic-inorganic perovskite solar cells (PSCs) often incorporate $PC_{70}BM$ as the electron transporting layer (ETL) which offers high performance top electrode electron carriers charge selectivity as well as passivation of the perovskite active layer grain boundaries. Thick fullerene diffusion blocking layers have been previously shown to be beneficial for the long-term thermal stability of p-i-n PSCs. However, the low conductivity of $PC_{70}BM$ significantly limits the thickness of $PC_{70}BM$ buffer layer for optimized PSCs performance. In this chapter it is shown that by applying the “just enough” doping principle we can increase the PCE of inverted PSCs devices with thick (200 nm) $PC_{70}BM$ diffusion blocking layer from 7.84 to 13.1 % via doping with 0.3 % w.t. N-DMBI. Most importantly, doped thick $PC_{70}BM$ based devices retain a high thermal stability at 60 ^{O}C of up to 1000 h without sacrificing their photovoltaic (PV) parameters and PCE.

5.2 Utilization of N-DMBI as n-type dopant for $PC_{70}BM$

In the previous chapter it is shown a simple yet effective method to improve the thermal stability of PSCs utilizing thick fullerene diffusion blocking layers. However, it is also observed that by increasing the thickness of the fullerene layers there is a dramatic drop of the FF and PCE due to the limited conductivity of $PC_{70}BM$ even if the stability is improved. Our previous findings on proposing thick fullerene diffusion blocking layers for long lived PSCs were also directly matched with the device simulations findings of Tessler *et.al.* [119] In their work they have successfully simulated ionic diffusion in PSCs and have also shown that by increasing the thickness of $PC_{70}BM$ from 50 to 200 nm the ionic diffusion as well as ionic accumulation at the contacts is decreased indicating that it will take more than 10 times longer to start observing some degradation by incorporating 200 nm fullerene based diffusion blocking layer within the inverted PSCs device structure.

Large scale ETL fabrication techniques such as Dr. Blade and roll-roll are often utilized for the fabrication of large scale PV devices. [130] Therefore utilizing thick ETL layers which are compatible with such techniques is desirable for the up-scalability of PSCs. Currently this is problematic when using $PC_{70}BM$ as the ETL for PSCs due to the limited conductivity of the fullerene based electronic material. One of the most well-known methods to improve the conductivity of $PC_{70}BM$ is via doping using n-type dopants such as 4-(2, 3-Dihydro-1, 3-dimethyl-1*H*-benzimidazol-2-yl)-*N*, *N*-dimethylbenzenamine (N-DMBI). N-DMBI was reported to increase the conductivity of PCBM by 4-6 orders of magnitude (from ~10^{-9} S/cm to $5x10^{-3}$ S/cm). [131] [132] [133] [134] It has also been shown that doped PCBM exhibits a decrease of the Fermi level (E_F) from 5.04 to 4.78 eV towards the lowest unoccupied molecular orbital (LUMO) which further highlights the n-type doping of the material. [134] Therefore, n-type doping of PCBM with N-DMBI has been shown to be an effective and beneficial way to increase the conductivity and efficiency of devices, which has been demonstrated in various applications such as organic photodiodes (OPDs) [131] and PSCs [133] [134]. It is important to note that doping should usually follow the “just enough” concept, meaning that it should not exceed an optimal value. It has been reported by Tessler *et.al* via simulations that when charge collection (CL) layers in PSCs are doped excessively they can promote ionic diffusion depending on the nature of the doping. In particular excessive p-type doping usually promotes the diffusion of cations whereas excessive n-type doping promotes the diffusion of anions [135], both of which are detrimental for the stability of PSCs.

5.3 Device structure and N-DMBI morphological characterization

The fabricated devices presented within this chapter were based on the p-i-n- inverted device structure of ITO/Cu:NiO$_X$/$CH_3NH_3PbI_3$/$PC_{70}BM$/BCP/Cu as shown in Figure 5-1a. The Cu:NiO$_X$ was coated using Dr. Blade coating followed by combustion synthesis. The perovskite active layer formulation was based on solvent-anti solvent recipe. The $PC_{70}BM$ was spin coated on the active layer followed by thermal evaporation of the BCP and Cu films. These fabrication steps are described in detail in Chapter 3-Materials and Methods. A schematic representation of the structure of N-DMBI and PCBM are shown in Figure 5-1b. The doping mechanism of N-DMBI follows the general consensus that the dopant functions as a hydride atom donor to the host material ($PC_{70}BM$) followed by an electron transfer step between the molecules of the host material [136] due to the natural affinity of $PC_{70}BM$ to undergo hydrogenation reactions with various hydrogen-atom donors. [137]

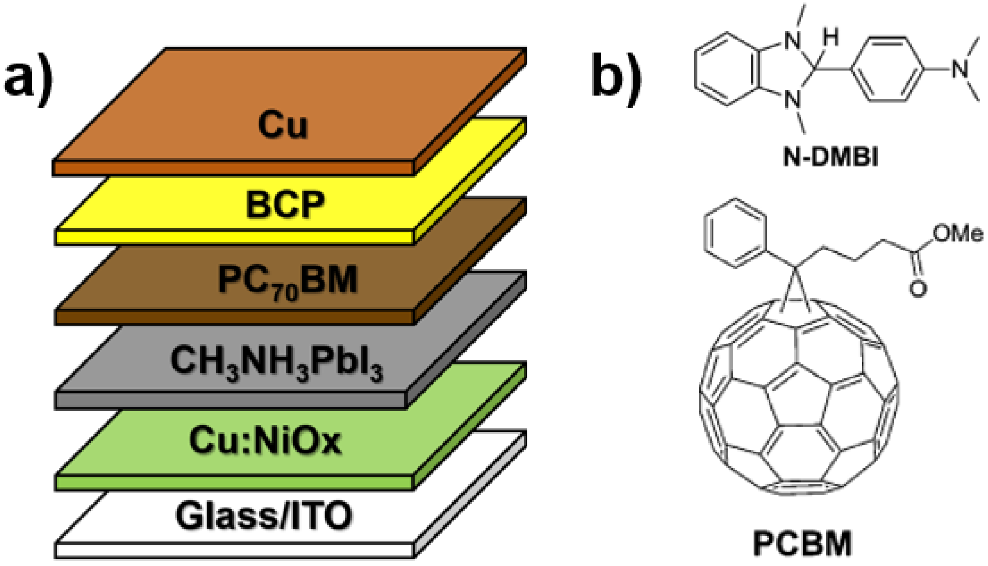

FIGURE 5-1: a) Device architecture, b) N-DMBI and PCBM schematic representation

ITO/$PC_{70}BM$ films are fabricated to evaluate any potential morphological changes to the $PC_{70}BM$ due to doping. From the AFM data (Figure 5-2) no apparent morphological changes are observed between ITO/PC$_{70}$BM un-doped and 0.3 % w.t. doped films (which is later shown to be the optimum doping concentration) while also having similar roughness values (1.34 nm for un-doped and 1.25 nm for doped films).

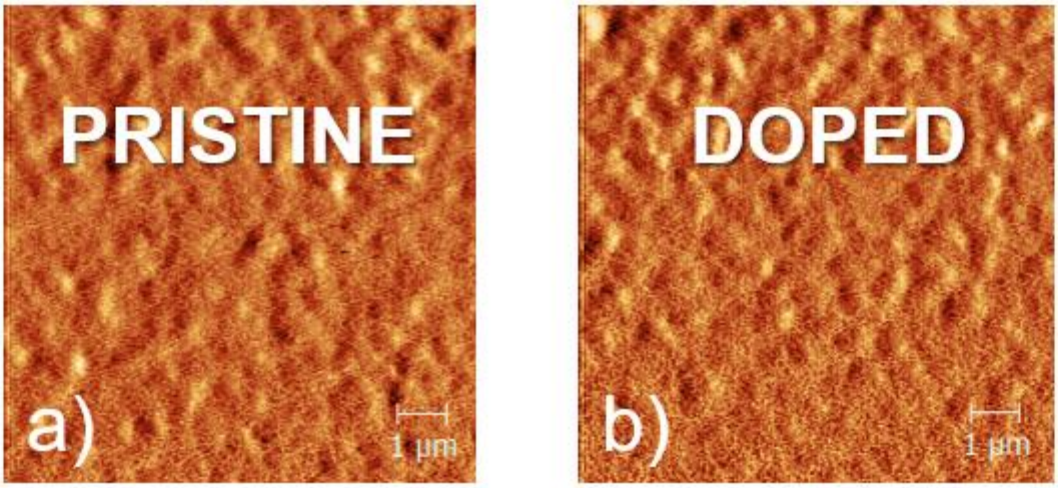

Figure 5-2: AFM measurements in phase contrast mode of a) ITO/PC$_{70}$BM pristine b) ITO/PC$_{70}$BM (0.3 % w.t. N-DMBI)

5.4 Device characterization and thermal stability of pristine and N-DMBI doped p-i-n PSCs

To evaluate the effect of doping in devices with thick (200 nm) PC$_{70}$BM ETLs we have characterized the light and dark J/V PV parameters using a calibrated Newport Solar simulator equipped with a Xe lamp, providing an AM1.5G spectrum at 100 mW/cm^2 as measured by a certified oriel 91,150 V calibration cell. A custom-made shadow mask was attached to each device prior to measurements to accurately define the corresponding device area (9 mm^2).

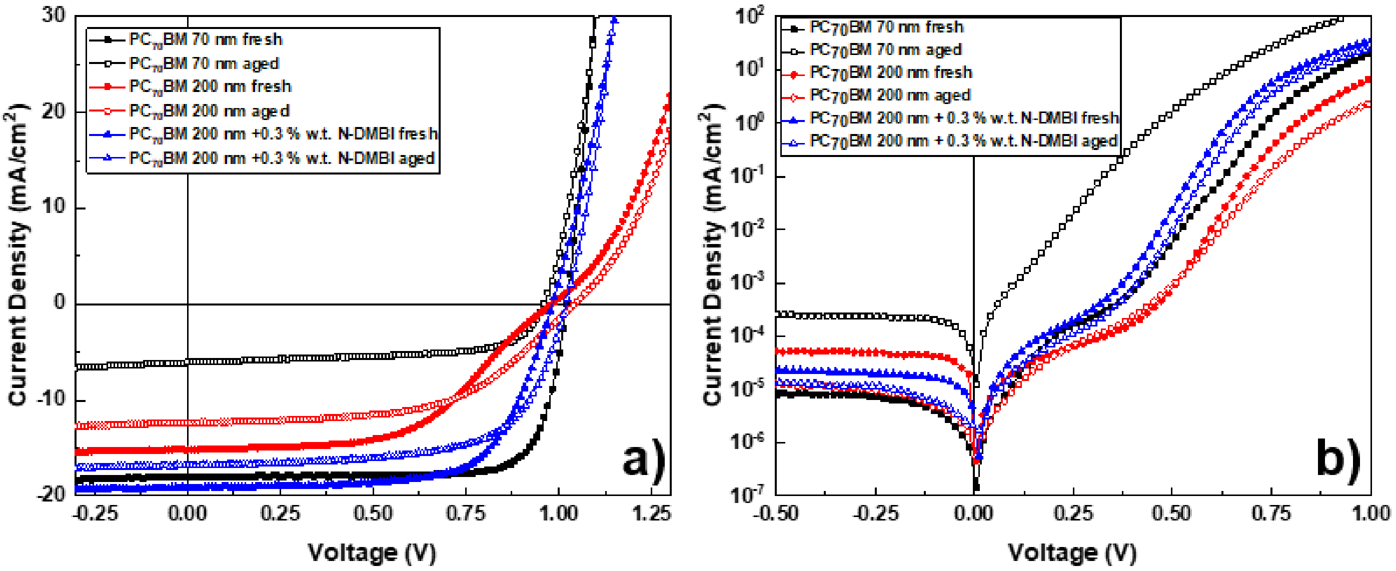

Figure 5-3: a) Light J/V plots b) dark J/V plots of fresh and aged devices based on un-doped and doped $PC_{70}BM$

Various N-DMBI doping concentrations (0.1, 0.3, 0.5 and 0.7 % w.t.) were evaluated to identify the optimum value for devices based on thick $PC_{70}BM$ ETLs. When we increase the thickness of $PF_{70}BM$ from 70 to 200 nm we see a decrease of V_{OC} from 1.02 to 0.98 V, J_{SC} from 18.04 to 15.2 mA/cm^2, FF from 78.5 to 52.5 % and PCE from 14.48 to 7.84 % (Table 5-1) which is a similar trend that we observed in the previous chapter. The experimental values of J_{SC} are in good agreement with the theoretically calculated J_{SC} values from the EQE data, which is <5 % in margin of error (Figure 5-4).

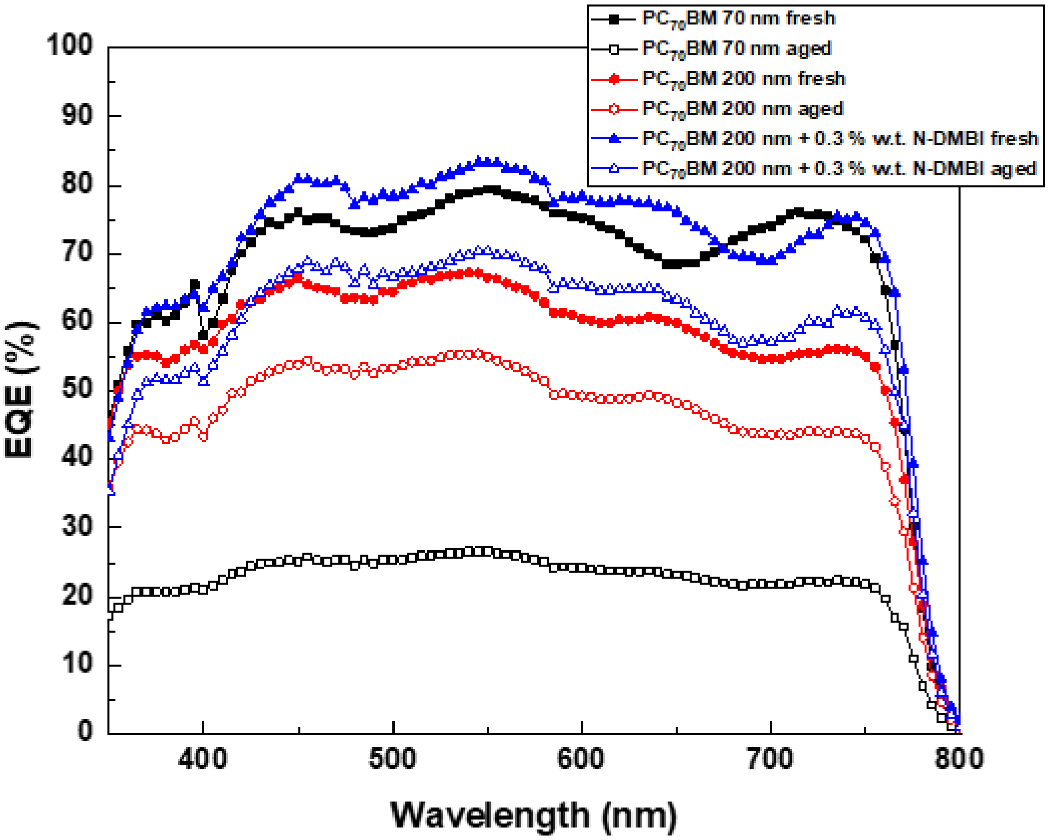

Figure 5-4: EQE data for thin (70 nm), thick (200 nm) and doped (0.3 % w.t. N-DMBI) fresh and aged devices

This is also shown in the light and dark J/V plots (Figure 5-3 a, b). An increase in R_S from 4.9 to 13.1 Ω and a decrease in R_{SH} from 53.1 to 41.7 kΩ which results in the decrease of J_{SC}, V_{OC} and FF respectively due to the limited conductivity of $PC_{70}BM$ is observed. This is further discussed in the impedance spectroscopy characterization. By introducing the optimum n-type doping concentration of N-DMBI (0.3 % w.t.) we managed to decrease the R_S from 13.1 to 1.5 Ω and increase R_{SH} from 41.7 to 50.2 kΩ which in return improve the J_{SC} from 15.2 to 19 mA/cm^2 , FF from 52.6 to 70.3 % and PCE from 7.84 to 13.1 % respectively. This improvement was reported in the literature to be due to the increase in conductivity and up-shift of E_F, leading to the enhancement of electron transporting properties of $PC_{70}BM$ and an increase of the photocurrent of the device. [133] [134] When the doping concentration is increased from 0.3 to 0.5 and especially 0.7 % w.t. we observe a drop in V_{OC} and FF, therefore the optimum doping concentration was identified to be 0.3 % w.t.

TABLE 5-1: PSCs PV parameters of pristine and N-DMBI doped devices

Device structure	V_{oc} (V)	J_{sc} (mA/cm^2)	FF (%)	PCE (%)
ITO/Cu:NiO$_X$/CH$_3$NH$_3$PbI$_3$/PC$_{70}$ BM (70 nm)/BCP/Cu	1.02	18.04	78.5	14.48
ITO/Cu:NiO$_X$/CH$_3$NH$_3$PbI$_3$/PC$_{70}$BM (200 nm)/BCP/Cu	0.98	15.2	52.6	7.84
ITO/Cu:NiO$_X$/CH$_3$NH$_3$PbI$_3$/PC$_{70}$BM (200 nm+0.1 % w.t. N-DMBI)/BCP/Cu	0.97	17.69	65.1	11.2
ITO/Cu:NiO$_X$/CH$_3$NH$_3$PbI$_3$/PC$_{70}$BM (200 nm+0.3 % w.t. N-DMBI)/BCP/Cu	**0.98**	**19**	**70.3**	**13.1**
ITO/Cu:NiO$_X$/CH$_3$NH$_3$PbI$_3$/PC$_{70}$BM (200 nm+0.5 % w.t. N-DMBI)/BCP/Cu	0.91	19.4	63	11.14
ITO/Cu:NiO$_X$/CH$_3$NH$_3$PbI$_3$/PC$_{70}$BM (200 nm+0.7 % w.t. N-DMBI)/BCP/Cu	0.90	17.83	58.5	9.45

Following the J/V characterization we have performed impedance spectroscopy measurements to get more insight on the charge dynamics of the device. The impedance spectroscopy was performed using a white LED light source and a frequency range of 1 Hz- 1 MHz.

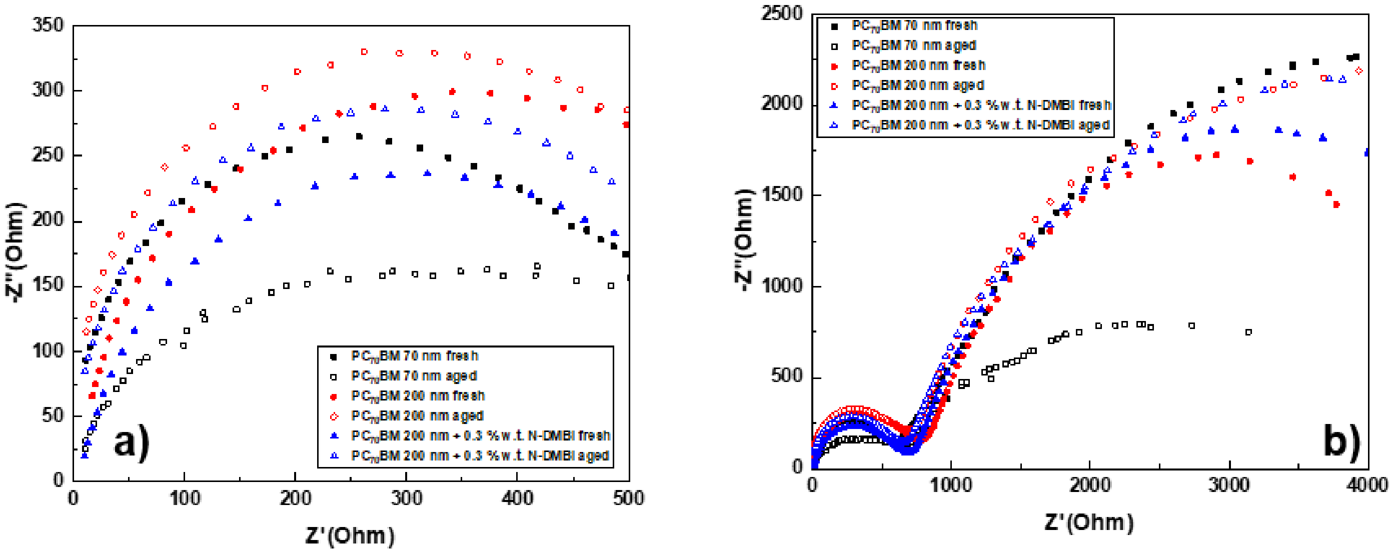

FIGURE 5-5: a) Nyquist plot in high frequency b) Nyquist plot in low frequency

Two distinct frequency responses in the Nyquist plots are observed, one at the high frequency (HF) range and one at low frequency (LF) range. It has been previously reported that the frequency response at HF is tied to the charge transport resistance (R_{TR})

of the device, whereas the LF response is tied to the charge recombination resistance (R_{REC}) of the device. [106 110] We see an increase in R_{TR} when we increase the thickness of $PC_{70}BM$ (FGI. 3a), which is in accordance with the increase of R_S from the dark J/V plots due to the limited conductivity of the material. Upon introducing 0.3 % w.t. N-DMBI we see a decrease in R_{TR} similar to the decrease of R_S. Increasing the thickness of $PC_{70}BM$ also reduces R_{REC} (Figure5-5b) which is in accordance with the decrease of R_{SH}. R_{REC} is tied to the charge accumulation under illumination at the electrodes of the device. Using thick $PC_{70}BM$ we introduce more charge recombination events in the ETL due to the increased trapping of the thick film and its limited conductivity. R_{REC} is substantially improved upon introducing 0.3 % w.t. N-DMBI, which can also be seen from the improvement of the FF, however it is still lower than the thin $PC_{70}BM$ based devices.

Following the characterization of 0.3 % w.t. N-DMBI based devices heat lifetime tests are performed (60 ^oC, N_2) to verify that the devices based on thick doped $PC_{70}BM$ ETL not only had improved PV parameters but also retained a high lifetime. The goal of this work was not to achieve the highest possible PCE, but to evaluate the application of thick fullerene diffusion blocking layers in conjunction with doping to achieve high stability while still retaining a good compromise between lifetime and PV performance.

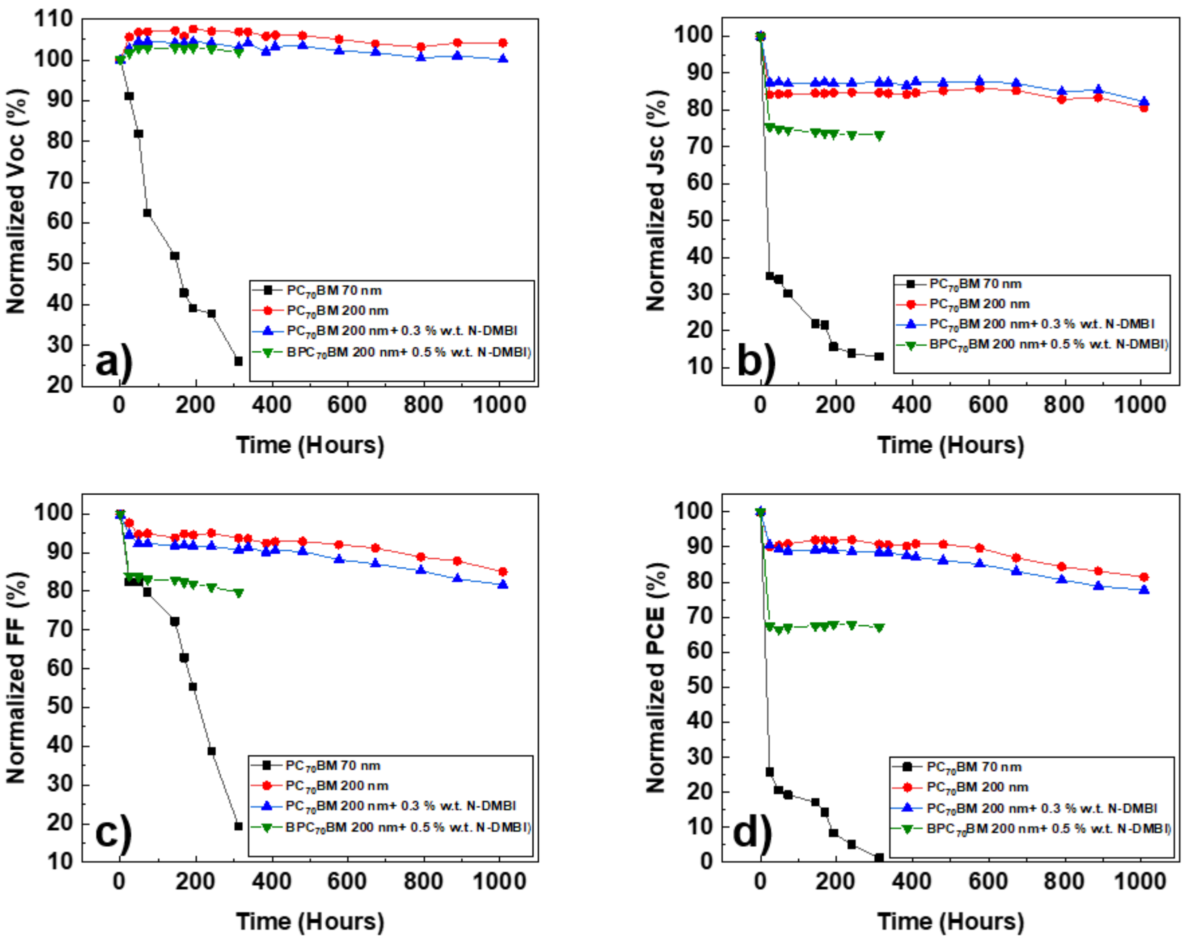

FIGURE 5-6: Normalized lifetime plots of a) V_{OC}, b) J_{SC}, c) FF and d) PCE after aging in 60 ^{O}C, N_2

From the lifetime plots of Figure 5-6 we see that our reference devices based on thin (70 nm) $PC_{70}BM$ ETL there is a rapid drop in all PV parameters even at the first 24 h of aging. This drop in PCE has been previously identified to be a result of ion diffusion (especially I-) towards the electrodes of the device. By increasing the thickness of $PC_{70}BM$ the lifetime is improved, by functioning as a thick diffusion blocking layer, achieving T_{80} at 1000 h, however as discussed previously in this report, this comes to an expense to the PCE of the device due to the limited conductivity of $PC_{70}BM$. Using 0.3 % w.t. N-DMBI doped devices we report improved lifetime while still retaining a good PCE. It is important to note that when the doping was increased from 0.3 to 0.5 % w.t. N-DMBI there is also a drop in lifetime. Following the discussion of the “just enough” doping mentioned previously in this report as well as the simulations performed by Tessler et. al we believe that by using 0.5 % w.t. N-DMBI we promote the I- diffusion and accumulation towards the metal electrode (following the n-type doping-anion correlation previously discussed), thus decreasing the stability of the device as well. This further highlights the importance of just enough doping concept. To visualize the trend of J_{SC} lifetime we have performed photocurrent (PCT) measurements for all the devices evaluated. The results are presented in Figure 5-7.

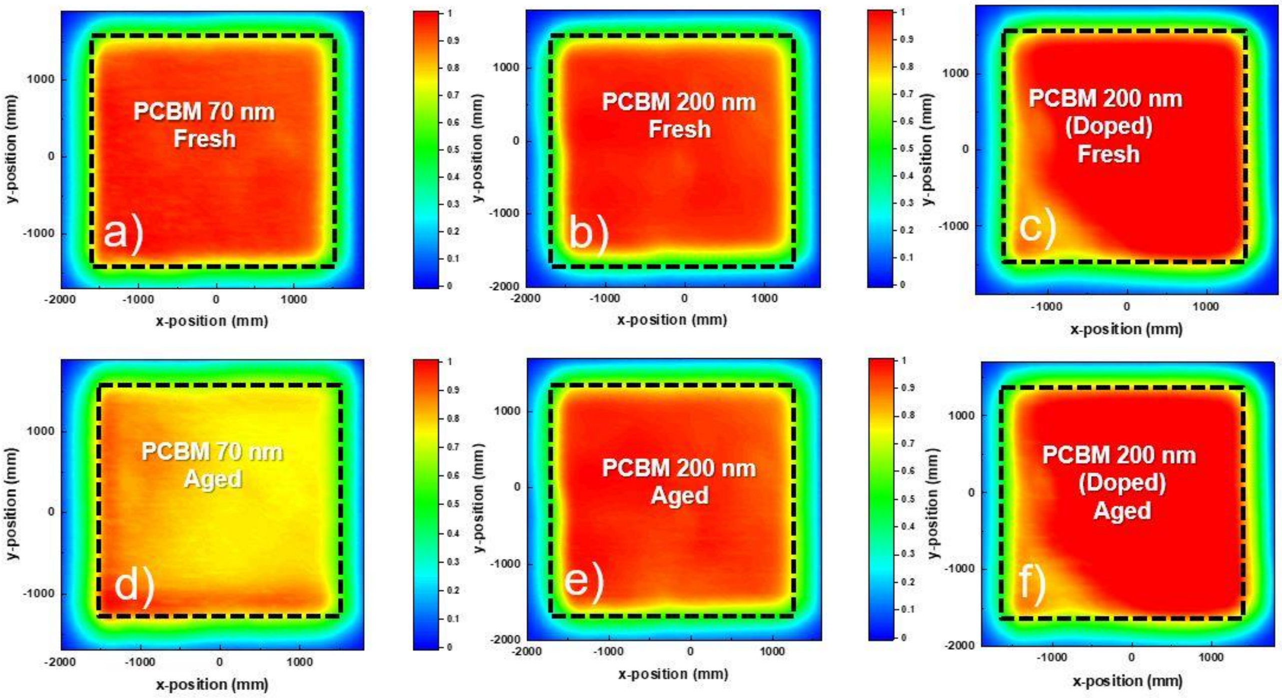

Figure 5-7: PCT data of $PC_{70}BM$ based devices: a) 70 nm fresh, b) 200 nm fresh, c) 200 nm 0.3 % w.t. N-DMBI fresh, d) 70 nm aged, e) 200 nm aged and f) 200 nm 0.3 % N-DMBI aged

As it is shown, the trend of J_{SC} closely follows the PCT data. It is important to note that there is a slight increase in V_{OC} upon aging for the devices based on thick (200 nm) for both doped and un-doped $PC_{70}BM$ based devices. It has been previously reported that heat treatment can promote $PC_{70}BM$ diffusion towards the grain boundaries of the perovskite active layer, assisting in their passivation. [138] Intentional doping of the perovskite active layer with $PC_{70}BM$ has been reported to improve the PV parameters of PSCs [139] and we believe that in our case a similar mechanism can happen due a combination of large $PC_{70}BM$ thickness and its promoted diffusion due to the accelerated heat tests. This is further highlighted by the increase in R_{SH} from the dark J/V plots and R_{REC} from the Nyquist plots, which point towards reduced charge recombination, which can happen upon grain boundary passivation.

5.5 Summary

It is shown that thick $PC_{70}BM$ ETLs can be successfully utilized as diffusion blocking layers for p-i-n inverted PSCs. By utilizing an optimal n-type doping concentration of 0.3 % w.t. N-DMBI in conjunction with thick (200 nm) $PC_{70}BM$ ETLs highly stable (T_{80}=1000 h under 60 ^{O}C, N_2) devices are achieved while still retaining good PCE at 13.1 %. By increasing the doping from 0.3 to 0.5 % w.t. we observe a drop in lifetime which was correlated with the promotion of I^- diffusion towards the metal electrode following the observations from the simulations by Tessler *et. al.* Retaining a good PCE was mainly a result of improved J_{SC} and FF due to the improvement of the $PC_{70}BM$ conductivity, which resulted in a decrease of R_S from 13.1 to 1.5 Ω and increase of R_{SH} from 41.7 to 50.2 kΩ. Utilizing thick $PC_{70}BM$ ETLs while still retaining a good compromise between lifetime and PCE is important for the up-scalability of p-i-n- inverted PSCs and just-enough doping is essential to retain this balance. The proposed method of incorporating N-DMBI doped thick fullerene diffusion blocking layer within the inverted PVSK device architecture can be in practice easily applied to roll to roll printing manufacturing process providing a simple device engineering route for achieving high performance PSCs.

6 SURFACE TREATMENT OF Cu:NiO$_x$ HOLE-TRANSPORTING LAYER USING β-ALANINE FOR HYSTERESIS-FREE AND THERMALLY STABLE INVERTED PEROVSKITE SOLAR CELLS

6.1 Abstract

Inverted perovskite solar cells (PSCs) using Cu:NiOx hole transporting layer (HTL) often exhibit stability issues and in some cases J/V hysteresis. In this chapter a β-alanine surface treatment process on Cu:NiOx HTL is developed that provides J/V hysteresis-free, highly efficient, and thermally stable inverted PSCs. The improved device performance due to β-alanine-treated Cu:NiOx HTL is attributed to the formation of intimate Cu:NiOx/perovskite interface and reduced charge trap density in the bulk perovskite active layer. The β-alanine surface treatment process on Cu:NiOx HTL eliminates major thermal degradation mechanisms, providing 40 times increased lifetime performance under accelerated heat lifetime conditions. By using the proposed surface treatment, optimized devices are reported with high PCE (up to 15.51 %) and up to 1000h lifetime under accelerated heat lifetime conditions (60 ^{o}C, N_2).

6.2 Cu:NiO$_x$ performance inconsistencies and metal oxide amino acid surface treatment

Although NiOx has been widely used as an effective HTL in terms of both PCE and stability, its behavior has also been reported to be inconsistent. In particular, the stability and performance of NiOx based devices can vary based on the deposition methods of the NiOx films. For instance, PSCs based on combustion synthesis (CS)of NiOx films have been reported to exhibit better ambient stability compared to their sol-gel counterparts due to better interface with the perovskite as well as better perovskite film quality [140]. A more recent approach for Cu:NiOx synthesis incorporates a sol-gel approach with various organic solvents in order to avoid toxic catalysts. [141] Another factor that can negatively impact the stability of PSCs is the presence of organic ligands on the surface of nanoparticle suspensions of NiOx [142]. Even by solely considering the nature of NiOx films, the situation is not straightforward. The PCE of NiOx-based PSCs was reported to have a large variation between 8% and 20 % even in cases where similar synthesis and deposition methods of NiOx have been used [141]. Furthermore, hysteresis effects have also been observed. It has been reported in the literature that such effects can manifest due to the composition of NiOx, which consists of NiO and Ni_2O_3, from which NiO is known to have strong dipole moment [143]. This can cause device limitations due to the appearance of surface dipoles in NiOx, which can attract perovskite precursor ions (e.g., $CH_3NH_3^+$, I^- and Pb^{2+}) during the crystallization process and induce ionic vacancies and defects in the perovskite crystal. This is particularly apparent if NiOx is used as a HTL for inverted p-i-n PVSCs, because it acts as the underlayer and will affect the crystallization process of the perovskite [141]. Metal oxides interact with atmospheric oxygen, especially when photoexcited by UV light. Different from most organic semiconductors, which will become oxidized, metal oxides can catalyze oxidative decomposition of other organic materials which come in contact with. Oxygen is readily adsorbed at oxygen vacancies in metal oxides, from where it can form reactive superoxide species upon UV light exposure. [45]. These superoxide species will oxidize most materials they come in contact with, including metal halide perovskites.

Amino acids have been used before in the field of PSCs either as cross-linkers [144] or anchoring groups [145] due to their unique structure ($^{-}$HOOC-R-NH_3^+). In terms of cross-linking, their structure allows them to form hydrogen bonds between the cations and halogen ions of the perovskite crystal, thus improving its properties.[144] Furthermore, they can be adsorbed in the surface of metal oxides through their $COOH^-$ group, leaving their NH_3^+ group exposed, which in return can contribute to the crystallization process of the perovskite. [145] A common amino acid is β-alanine, which has been previously used in the form of β-alanine-HI salt, acting as an anchoring group on the surface of porous TiO_2, improving the PCE of normal-structured PSCs [145]. β-Alanine has also been used as an additive to PEDOT:PSS in order to reconstruct the distribution of $–SO_3^-$ and $–SO_3H$, thus improving charge transport and collection as well as its hydrophobicity [146].

In this chapter a β-alanine based surface treatment for Cu:NiOx HTLs is developed for the inverted (p-i-n) PVSCs device structure. Due to a combination of more intimate Cu:NiOx/Perovskite interface and passivation of oxygen vacancies is achieved, reducing charge trap density both at the interface as well as in the bulk perovskite layer. Using the proposed β-alanine surface treatment significantly reduced the hysteresis of Cu:NiOx-based PVSCs is achieved and a champion PCE of 15.51 % is reported while also improving stability from 24 h to 1000 h under accelerated heat conditions in inert atmosphere (60 ^{o}C, N_2).

6.3 Cu:NiO$_x$ film characterization utilizing β-alanine surface treatment

To study the effect of β-alanine-treated Cu:NiOx on the performance of p-i-n PSCs an initial study was performed on both the film properties of Cu:NiOx and Cu:NiOx/β-alanine as well as the perovskite film crystallized on top of Cu:NiOx and Cu:NiOx accordingly.

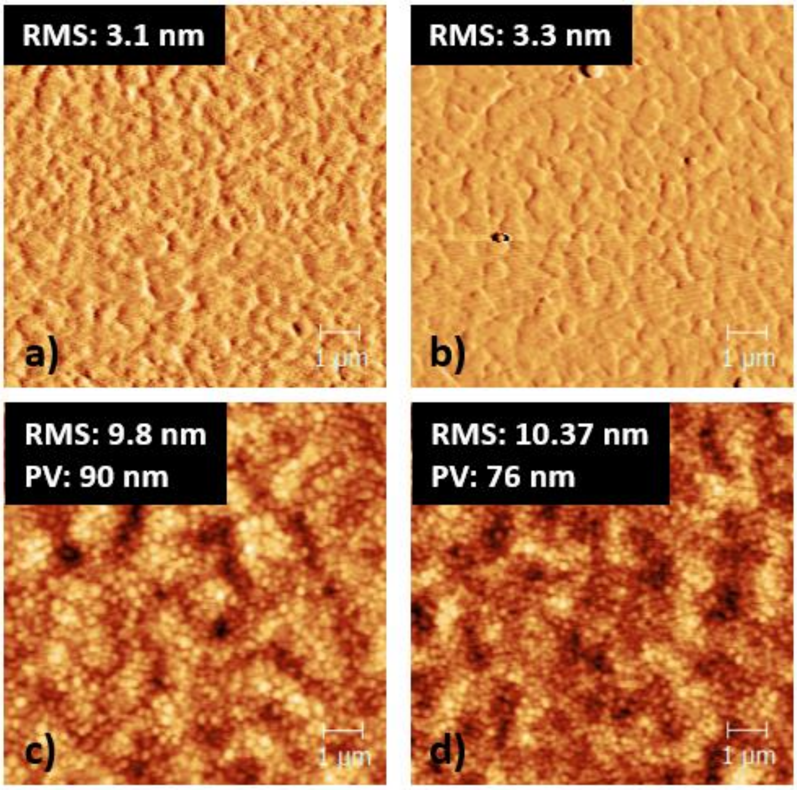

Figure 6-1. AFM images of a) phase contrast of quartz/Cu:NiOx, b) phase contrast of quartz/Cu:NiOx/β-alanine, c) topography of ITO/Cu:NiOx/Perovskite and d) topography of ITO/Cu:NiOx/β-alanine/Perovskite.

Figure 6-1. shows the AFM data as well as the calculated roughness (RMS) and peak to valley (P-V) of the films. Initially, the RMS of both Cu:NiOx and Cu:NiOx/β-alanine on quartz are calculated and have shown similar values at ~3 nm. It is also worth noting that when the perovskite film is coated on top of ITO/Cu:NiOx and ITO/Cu:NiOx/β-alanine it has similar RMS of ~10 nm. This indicates that β-alanine surface treatment does not introduce any extra roughness to the Cu:NiOx film. Although the RMS of the perovskite film is very similar, there is a distinguishable difference in P-V. In detail, P-V is decreased from 90 to 76 nm when the perovskite film is crystallized on top of ITO/Cu:NiOx/β-alanine compared to ITO/Cu:NiOx. P-V is defined as the distance between the highest peak and the lowest valley of a topographical image and is desirable to be as low as possible in order to ensure compact, smooth and pinhole free films [147].The phase contrast data of ITO/Cu:NiOx/Pvsk and ITO/Cu:NiOx/β-alanine/Pvsk is shown in FIG. S1.

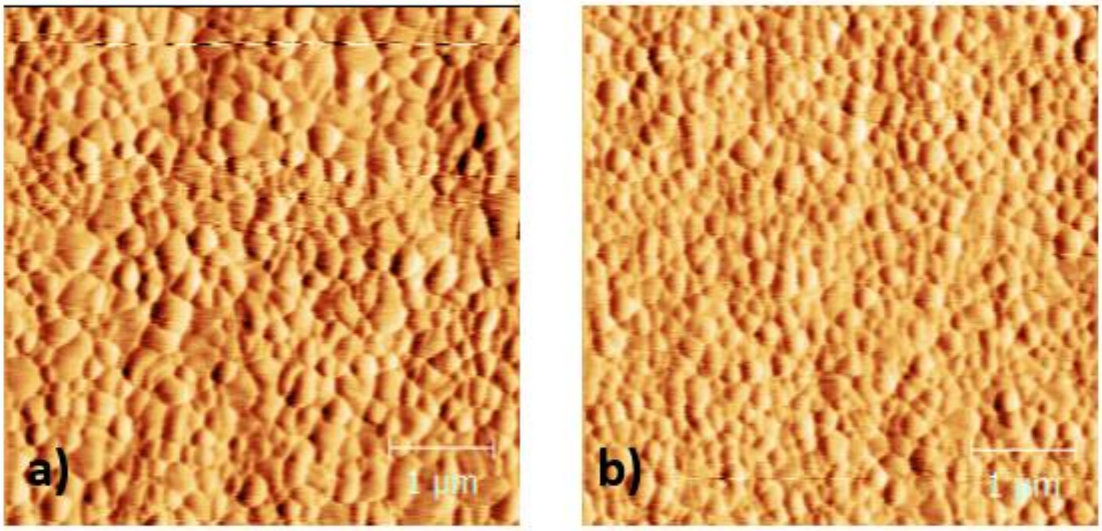

Figure 6-2: AFM measurements in phase contrast of a) ITO/Cu:NiOx/Pvsk, b) ITO/Cu:NiOx/βalanine/Pvsk

From Figure 6-1c,d and Figure 6-2 a similar morphology of the crystallized perovskite between pristine and alanine treated Cu:NiOx is reported. Although wetting properties in some cases influence the performance of interfaces, negligible difference in the contact angle measurements of pristine Cu:NiOx and alanine-treated Cu:NiOx was observed as shown in Figure 6-3, indicating that wetting properties by the proposed surface treatment remain unaffected.

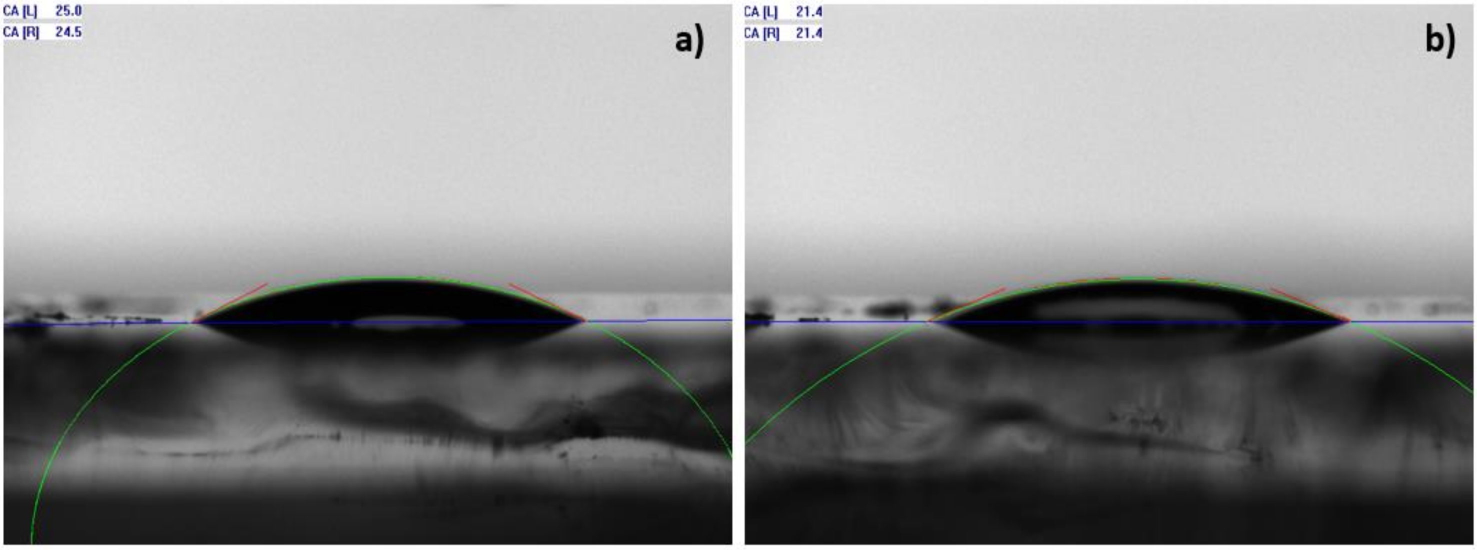

Figure 6-3: Contact angle film measurements of a) Cu:NiOx, b) Cu:NiOx/alanine using γ-butyrolactone:DMSO (7:3) for the perovskite solvent.

Furthermore, having a bottom electrode with high transparency to ensure efficient light transmission towards the active layer for the generation of carriers is required. Considering these requirements, we have also performed transmittance and absorption measurements in ITO/Cu:NiOx, ITO/Cu:NiOx/β-alanine, ITO/Cu:NiOx/Pvsk and ITO/Cu:NiOx/β-alanine/Pvsk films.

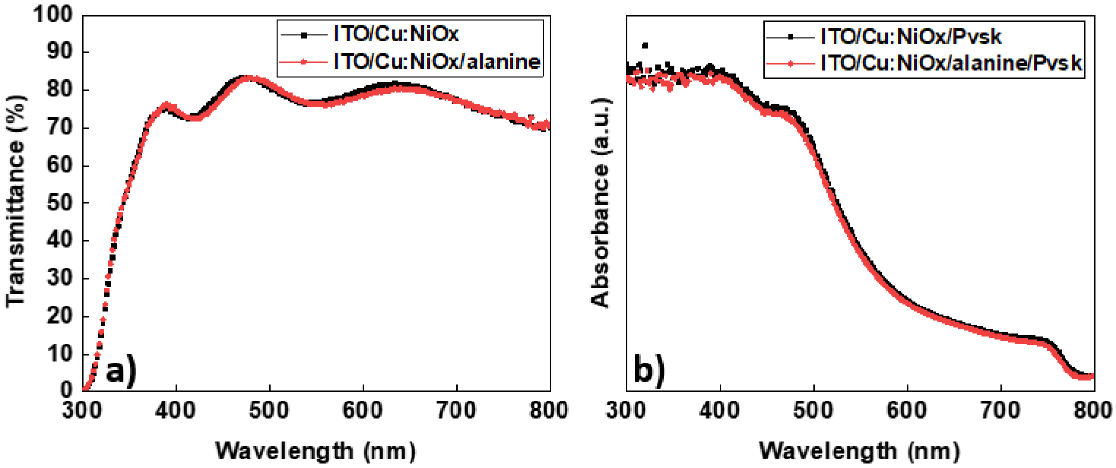

Figure 6-4: a) Transmittance spectra of ITO/Cu:NiOx , ITO/Cu:NiOx/alanine and b) Absorbance spectra ITO/Cu:NiOx/Pvsk, ITO/Cu:NiOx/β-alanine/Pvsk.

The plots shown in Figure 6-4 indicate that there are no significant differences between either the transmittance of ITO/Cu:NiOx and ITO/Cu:NiOx/β-alanine or the absorption of the perovskite active layer, crystallized on top of the two aforementioned films. Following the AFM measurements, contact angle measurements, absorption measurements and photoluminescence (PL) spectroscopy was performed, using an excitation wavelength of 500 nm, to determine the charge carrier recombination characteristics of both Cu:NiOx and β-alanine-surface treated Cu:NiOx as well as the perovskite active layer crystallized in the two different films. The absorption spectra shown in Figure 6-5a show very similar characteristics and we can therefore deduce that the band gap (Eg) of Cu:NiOx does not change significantly upon β-alanine treatment. Equally interesting observations are indicated in Figure 6-4b. ITO/Pvsk exhibits a large peak at 760 nm as expected. Since the HTL is absent, very poor quenching is observed due to the poor carrier extraction and more frequent recombination events. Upon using Cu:NiOx we immediately observe an improvement to PL quenching of more than 90 %, indicating a great reduction in the band-to-band charge recombination and a better hole carrier selectivity. Upon β-alanine-treatment of the Cu:NiOx the PL quenching is improved even further (95 % quenching) pointing to even more efficient charge collection and an efficient suppression of the electron-hole recombination. The reported experimental results provide indication that charge traps lying in the Cu:NiOx/Pvsk interface are passivated upon treatment with β-alanine. Similar PL quenching behavior was also reported by Shih et. al. [148]. In their work, which studied the effect of surface treatment using several amino acids including β-alanine on TiO2, they attributed this observation to the preferential, perpendicular, orientation of the (110) plane of the MAPI crystallites towards the amino acid treated surface. This was observed using grazing-incidence wide-angle X-ray scattering of thin $CH_3NH_3PbI_3$ perovskite films.[148] This results to a more intimate interface of the metal oxide with MAPI, reducing the charge trap density of the metal oxide/MAPI interface. We hypothesize that we observe a similar behavior for the alanine treatment of Cu:NiOx. Furthermore Shih et.al have also performed UPS measurements and have shown that the E_{WF} of TiO_2 upon alanine treatment remains essentially the same. [148] Based on their results we do not expect a considerable shift to the E_{WF} of Cu:NiOx either upon alanine treatment. Finally, the conductivity values of pristine Cu:NiOx and alanine treated Cu:NiOx films were measured using a four point probe system and no considerable change is observed

(Cu:NiOx: 4.7 x 10-3 S/cm, Cu:NiOx/alanine 3.5 x 10-3 S/cm) in good agreement with the values reported in the literature. [149] The similar conductivity values of Cu:NiOx and alanine treated Cu:NiOx indicated that non-intentional doping effects are unlikely by the proposed surface treatment.

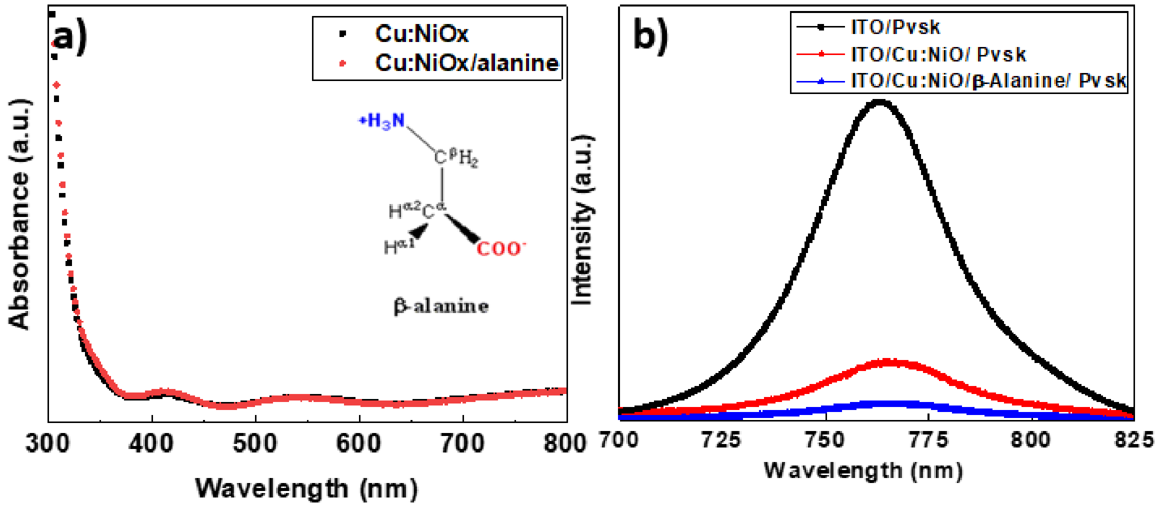

Figure 6-5. a) Absorption spectra of ITO/Cu:NiOx, ITO/Cu:NiOx/β-alanine and β-alanine structure used (inset figure) b) PL spectra of ITO/Pvsk, ITO/Cu:NiOx/Pvsk, ITO/Cu:NiOx/β-alanine/Pvsk.

6.4 Device characterization and thermal stability utilizing β-alanine surface treatment

Following the film characterization, full PSC devices are fabricated based on two different HTLs, pristine Cu:NiOx and β-alanine-treated Cu:NiOx. Two different thicknesses of Cu:NiOx were evaluated (20 and 40 nm) as well as three different concentrations of β-alanine solutions (30, 10 and 6 mg/mL). The perovskite active layer used was based on a $CH_3NH_3PbI_3$ (MAPI) formulation, detailed in the materials and methods section. The main device structure used was ITO/Cu:NiOx (40nm)/$CH_3NH_3PbI_3$ (300 nm)/$PC_{70}BM$ (70 nm)/BCP (7 nm)/Cu (80 nm). The thickness of each layer was measured using a profilometer. The PV device parameters are shown in Table 6-1. Standard deviation (SD) of the PCE is shown in Figure 6-6.

Table 6-1. PSCs PV parameters

Device architecture	**V_{oc} (V)**	**J_{sc} (mA/cm^2)**	**FF (%)**	**PCE (%)**
ITO/Cu:NiOx (40 nm)/$CH_3NH_3PbI_3$/PC_{70} BM/BCP/Cu	0.94	16.05	81.6	12.31
ITO/Cu:NiOx(40 nm)/β-alanine (30 mg/mL)/$CH_3NH_3PbI_3$/$PC_{70}BM$/BCP/Cu	1.05	14.54	48.4	7.40
ITO/Cu:NiOx (40 nm)/β-alanine (10 mg/mL)/$CH_3NH_3PbI_3$/$PC_{70}BM$/BCP/Cu	1.07	17.68	70.2	13.31
ITO/Cu:NiOx (40 nm)/β-alanine (6 mg/mL)/$CH_3NH_3PbI_3$/$PC_{70}BM$/BCP/Cu	1.05	18.61	74	14.46
ITO/Cu:NiOx (20 nm)/$CH_3NH_3PbI_3$/$PC_{70}BM$/BCP/Cu	1.03	17.19	79.5	14.13
ITO/Cu:NiOx (20 nm)/β-alanine (10 mg/mL)$CH_3NH_3PbI_3$/$PC_{70}BM$/BCP/Cu	1.07	20.13	71.7	15.51

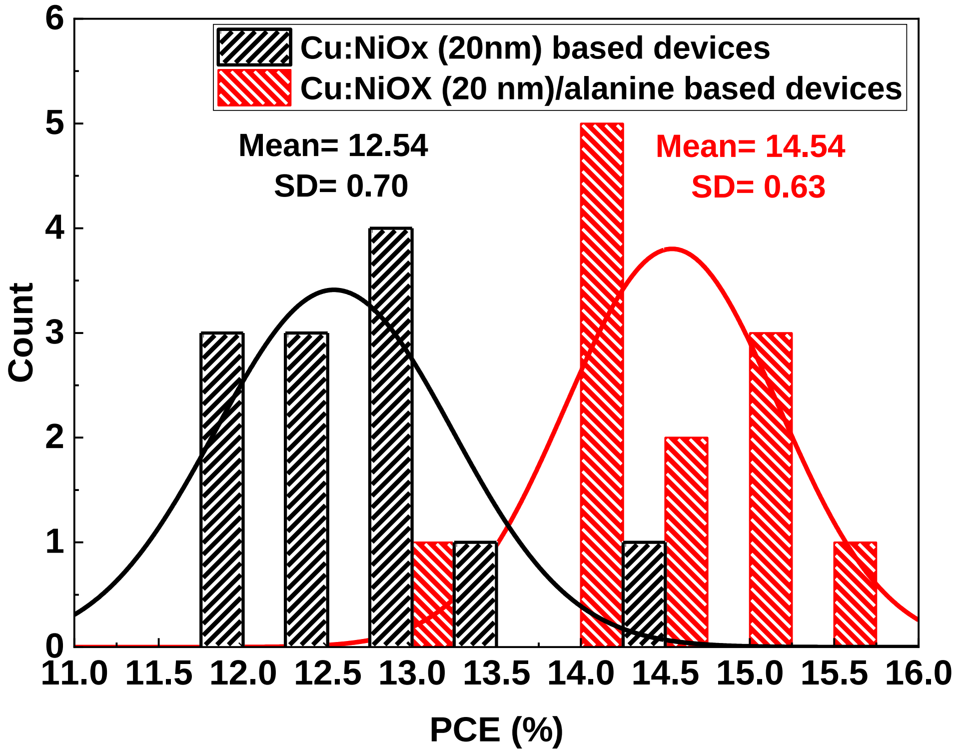

Figure 6-6: Average PCE and SD for the optimized devices based on Cu:NiOx (20 nm)

In Table 6-1 it is shown that upon surface treatment with β-alanine, the V_{OC} of Cu:NiOx based devices is increased from 0.94 to 1.05 V, however the FF drops dramatically from 81.6 to 48.4 %. We have observed that by decreasing the concentration of the β-alanine solution, the FF is improved. This is to be expected since amino acids in general are not conductive [150], and therefore a very thin layer should be coated on top of the Cu:NiOx to maintain functional devices. It is worth mentioning that apart from V_{oc}, the J_{sc} of devices is also improved upon the surface treatment of Cu:NiOx with β-alanine. As mentioned in the introduction, the stability of devices is equally important. The different device structures mentioned in Table 6-1 were subjected to accelerated heat conditions in inert atmosphere (60 ^{o}C, N_2) to assess the effect of β-alanine treatment in the stability of the devices.

By examining the lifetime plots in Figure 6-7 the difference in stability between Cu:NiOx and β-alanine-treated Cu:NiOx is very apparent. The PCE of Cu:NiOx (40 nm) based devices drops at ~ 40 % even in the first 24 h of aging, primarily due to a drop in J_{sc}. In the contrary, β-alanine-treated (10 mg/mL) Cu:NiOx devices retain their PCE and T_{80} (determined as the time needed for a device to reach 80 % of its initial PCE) is reached at 1000 h of aging. It is interesting to note that when the concentration of β-alanine is decreased to 6 mg/mL, the stability is also decreased, with the PCE dropping at 60 % of its initial value at 24 h of aging, similar to pristine Cu:NiOx. However, even if the PCE dropped to 60 % of its initial value, this is retained even at 1000 h of aging, although it is still lower than the standard T_{80}. When the thickness of Cu:NiOx is decreased from 40 to 20 nm, there is no significant difference observed in the device lifetime performances. The J/V characteristics of devices were studied to understand the mechanisms behind the degradation of Cu:NiOx devices and β-alanine-treated Cu:NiOx devices. Impedance spectroscopy was also used to understand these mechanisms in more detail. The characterization of devices was done in Cu:NiOx (40 nm) and Cu:NiOx (40 nm)/β-alanine (10 mg/mL) based devices. Both device structures were characterized at a time frame where the degradation phenomena were detectable but did not render the device un-measurable (24 h for untreated Cu:NiOx-based devices and 1000 h for β-alanine treated Cu:NiOx-based devices).

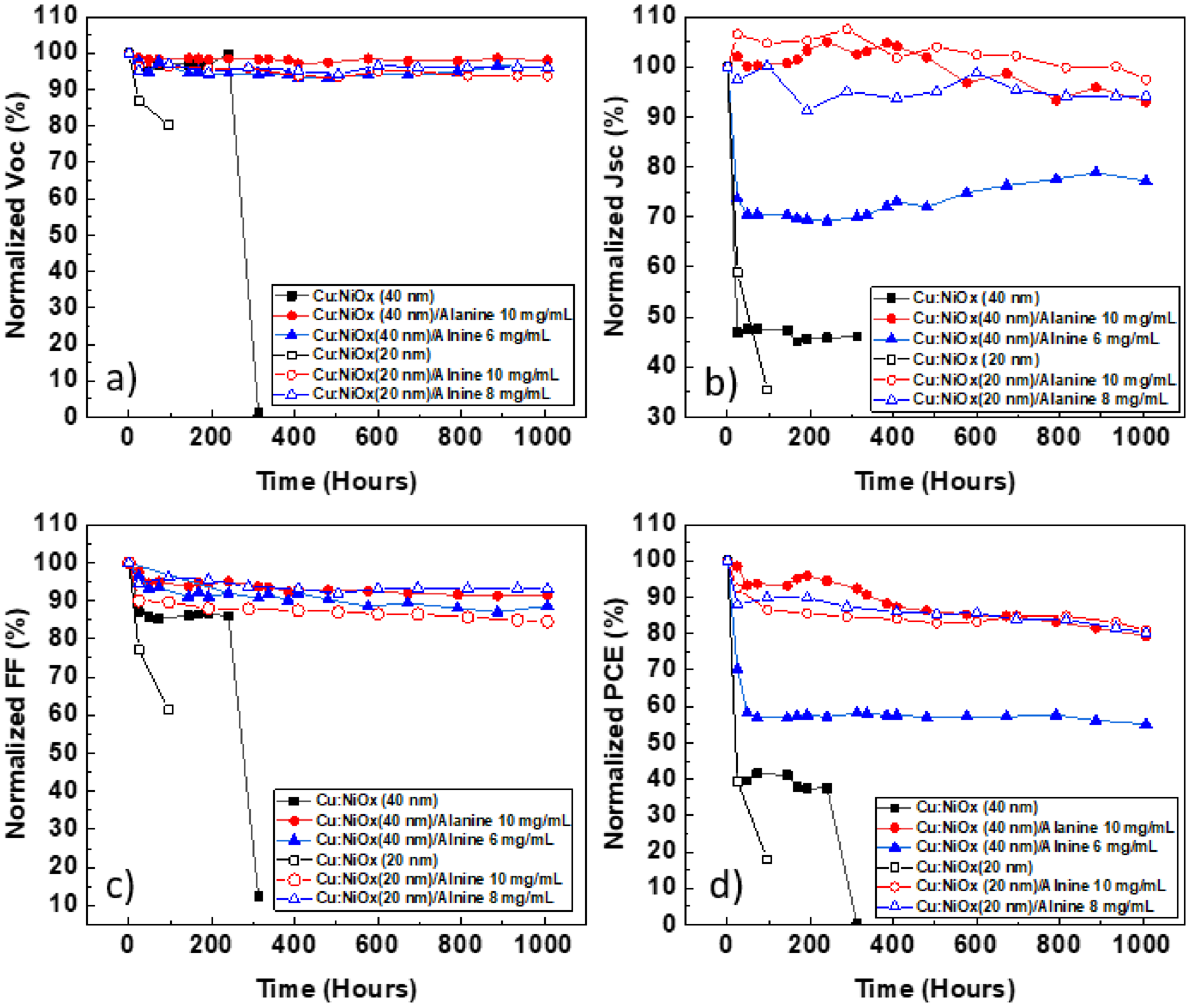

Figure 6-7: Lifetime plots of normalized: a) V_{oc}, b) J_{sc}, c) FF and d) PCE under accelerated heat conditions.

Cu:NiOx based devices exhibit severe hysteresis as it is shown in Figure 6-8 which is eliminated by leaving the devices under light soaking for 20 minutes. The PV parameters of Cu:NiOx based devises, in the forward (FW) and reverse (RV) scan direction, before and after light soaking are shown in Table 6-2.

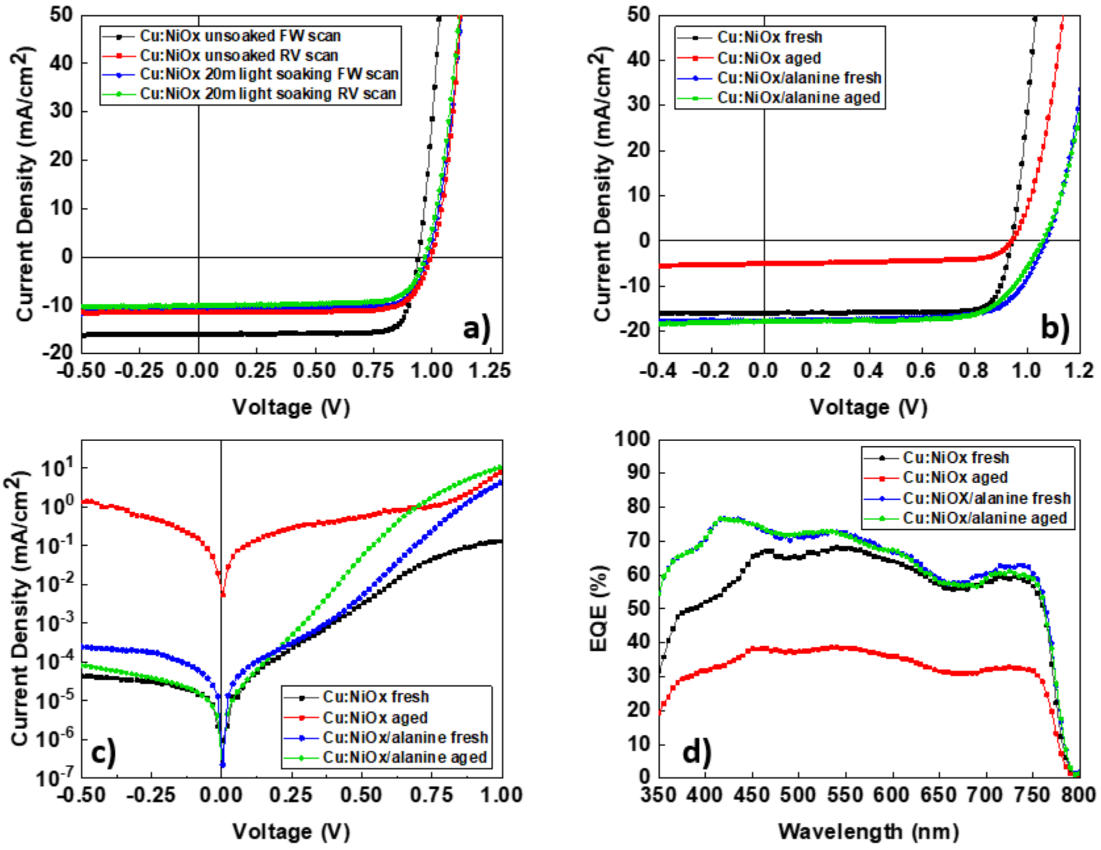

Figure 6-8: a) Illuminated J/V characteristics of Cu:NiOx devices before and after light soaking, b) illuminated J/V characteristics of fresh and aged Cu:NiOx and β-alanine-treated Cu:NiOx devices, c) dark J/V characteristics of fresh and aged Cu:NiOx and β-alanine-treated Cu:NiOx devices, d) EQE spectra of fresh and aged Cu:NiOx and β-alanine-treated Cu:NiOx devices.

Table 6-2. PV parameters of Cu:NiOx based devices before and after light soaking.

Device architecture	**V_{oc} (V)**	**J_{sc} (mA/cm^2)**	**FF (%)**	**PCE (%)**
Cu:NiOx based devices without light soaking	FW=0.94 RV=0.99	FW=16.05 RV=11.42	FW=81.6 RV=76.41	FW=12.31 RV=8.61
Cu:NiOx based devices after 20m light soaking	FW=0.98 RV=0.97	FW=10.79 RV=10	FW=77.4 RV=74.2	FW=8.19 RV=7.20

The hysteresis of p-i-n PSC devices based on Ni:Ox was also reported in the literature as we have previously stated and it was shown to have a recoverable effect on the PCE of the device upon light soaking. [141]In our case, even though the hysteresis is reduced significantly after light soaking for 20 minutes, the PCE is not recovered, in the contrary it decreases, primarily due to a decrease in J_{SC}. Interestingly, the V_{OC} has increased after light soaking. J/V hysteresis is a very common phenomenon in PSCs that has been previously ascribed to trapping and de-trapping of charged carriers [151]. Specifically J_{SC} hysteresis has been previously ascribed to trapping of charged carriers due to bulk defects of the perovskite layer [152]. Upon light soaking, passivation of these traps can occur by the charged carriers themselves, however less photo generated charges will contribute to the J_{SC} of the device due to a change in local electrical polarization effects on the surface of the crystal, resulting in poorer charge dissociation and reduction in J_{SC}. A similar passivation mechanism can be used to explain the increase in V_{OC}. V_{OC} is directly related to the built-in electric field (E_{BI}) of the device which is affected by the accumulation of charges at the electrodes. The increase in V_{OC} after light soaking can be explained by the reduction of charge accumulation at the interfaces of the devices. Trap passivation in the Cu:NiOx/Pvsk interface due to charged carriers generated after light soaking can cause a reduction to charge accumulation in this interface thus increasing the V_{OC} [151]. Trap filling phenomena have been previously reported to decrease the FF of PSCs upon light soaking. [141] This is also true in our case where we observe a drop in FF upon light soaking of Cu:NiOx based devices as shown in Table 6-2.Upon surface treatment of Cu:NiOx with β-alanine we observe an increase in V_{OC} and J_{SC} as well as significant reduction in hysteresis, shown in Figure 6-8b. Following the investigation of the observed J/V characteristics of devices with and without light soaking, as well as the E_{WF} data reported from Shih et. al [148], the increase in V_{OC} can be attributed to a reduction of charge traps at the Cu:NiOx perovskite interface and the increase in J_{SC} to reduced bulk defects in the perovskite crystal. The reduction of charged traps both at the interfaces as well as the bulk perovskite layer are also ascribed to the improved stability that β-alanine-treated Cu:NiOx inverted PSCs shown. Significant changes are also observed in the dark J/V characteristics shown in Figure 6-8c. In detail, β-alanine-treated Cu:NiOx based devices show reduction in the series resistance (R_S) from 75.14 **Ω** to 18.25 **Ω** and increase in shunt resistance (R_{SH}) from 15.47 k **Ω** to 35.65 k **Ω**, resulting to the improved V_{OC} and J_{SC} that these devices exhibit. The EQE spectra were also studied and presented in Figure 6-8d

Interestingly, the shape of the spectra is similar between untreated and β-alanine-treated Cu:NiOx based devices. The spectra of untreated Cu:NiOx are lower than β-alanine-treated Cu:NiOx based devices. The EQE spectra of untreated Cu:NiOx based devices show a significant decrease upon aging, following the J_{SC} drop, whereas β-alanine-treated Cu:NiOx based devices show no significant decrease in their EQE. The photocurrent from the EQE spectra was calculated using the overlap integral of the EQE spectrum with the AM 1.5G global spectrum and was found to have <5 % deviation from the calculated J_{SC} using the J/V characteristics for all the device structures under test (Cu:NiOx fresh: EQE current=15.72 mA/cm^2, JV current=16.05 mA/cm^2, Cu:NiOx aged: EQE current= 8.31 mA/cm^2, JV current= 7.91 mA/cm^2, Cu:NiOx/alanine fresh: EQEcurrent= 17.76 mA/cm^2, JV current=17.68 mA/cm^2, Cu:NiOx/alanine aged: EQE current= 17.47 mA/cm^2, JV current= 17.25 mA/cm^2)

To have a visual representation of the degradation of untreated and β-alanine-treated Cu:NiOx based devices we have performed photocurrent (PCT) mapping, shown in Figure 6-9. PCT allows us to have a visual representation of the current distribution in the device. Untreated Cu:NiOx based devices show non-uniform current distribution even if they are fresh. There are also areas in the device that show very little presence of current, which can be tied to the defects. Upon aging, the areas that show defects are enlarged and show even further current loss. β-Alanine-treated devices show a much more uniform current distribution which is also retained at a large degree even after aging. It is interesting to note that there is a small current loss at the edges of β-alanine-treated devices after aging shown in Figure 6-9d which can be tied to ingress of moisture from the edges of the encapsulation cover slip after the prolonged aging test.

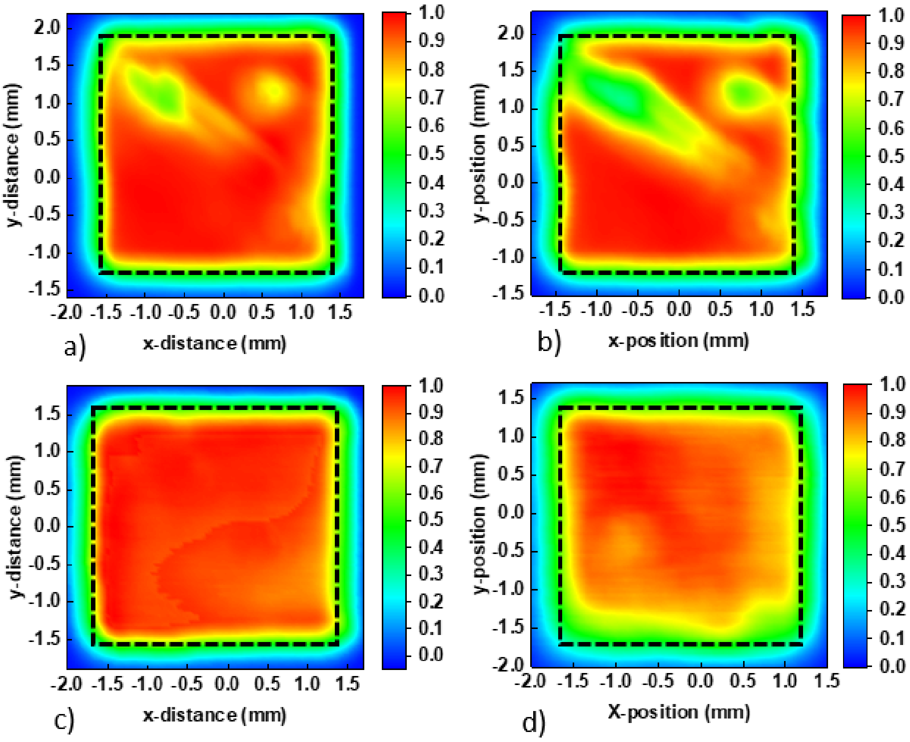

Figure 6-9: Photocurrent mapping of a) fresh Cu:NiOx, b) aged Cu:NiOx, c) fresh β-alanine-treated Cu:NiOx and d) aged β-alanine-treated Cu:NiOx based device.

To further investigate the origin of the degradation differences between the two device structures we have performed impedance spectroscopy (IS) and Mott-Schottky (MS) analysis. MS analysis is an extremely useful characterization technique that can be used to distinguish mechanisms that take place in the active layer with those in the interfaces. In reverse bias a capacitive plateau appears that corresponds to the geometric capacitance (Cg), related to the dielectric characteristics and polarizability of the active layer. The point of intersection of the linear slope with the x-axis corresponds to the estimated built-in voltage (EV_{BI}). It is interesting to note that the EV_{BI} deviates from the real V_{BI} value due to the depletion approximation used in MS analysis. The depletion approximation states that the capacitance in the space charge region manifests purely due to doping and not free charges, which generally does not hold true close to the metal contacts where free charges tend to accumulate. Although there is a deviation between EV_{BI} and V_{BI} it can still be used for comparative studies tied with the V_{OC} [111, 129]. By varying the frequency of the AC signal between high (HF) and low frequencies (LF) in MS analysis we can also detect trapping phenomena. In general at LF, since we approach DC conditions, trapped charges can de-trap and therefore by observing the change in MS plots between HF and

LF we can have a rough understanding of the trapping phenomena inside the device [126, 127]. In FIG. 6-10a an increase of the capacitive plateau from $3.2x10^{-9}$ F/cm^2 to $1.4x10^{-8}$ F/cm^2 is observed when we change the frequency from 100 to 5 kHz for untreated Cu:NiOx-based devices. The increase in capacitance at negative biases when we decrease the frequency indicates the presence of trapped charges in the space charge region, which is related to bulk defects of the perovskite layer. Capacitance increases further from $1.4x10^{-8}$ F/cm^2 to $7x10^{-7}$ F/cm^2 when we age the untreated Cu:NiOx-based devices and we keep the frequency constant at 5 kHz. When choosing an appropriate frequency for MS analysis it should usually coincide in the high-frequency plateau of the relevant capacitance frequency (CF) plot [129]. CF measurements were performed using this particular perovskite formulation and a similar p-i-n device structure in our previous work and therefore 5 kHz is an appropriate choice for our particular measurements [84]. In comparison, β-alanine-treated Cu:NiOx devices retain their capacitance at ~$2x10^{-9}$ F/cm^2 between HF and LF as well as after aging. These results agree with the J_{SC} and hysteresis behavior of both untreated and β-alanine-treated Cu:NiOx based devices. By observing the Nyquist plots we can observe two different frequency features at HF and LF, as denoted by the two different semi-circle arcs similar to what it is reported in the literature[153] The HF feature was previously attributed to the charge transport resistance (R_{TR}). There is also a small series resistance (R_S) shown by the indent of the curve with the y-axis and is attributed to the resistance from the experimental setup as well as the ITO. [109]The LF feature was previously attributed to ionic diffusion and the charge recombination resistance (R_{REC}) due to charge accumulation at the interfaces.[154,155] Under illumination the charge accumulation at the interfaces has been reported to be the dominant mechanism, similar to our case [109, 156]. Using the equivalent circuit model from our previous work [84] we have fitted the Nyquist plot data in order to extract values for R_{TR} and R_{REC} .Upon alanine treatment we report a drop for R_{TR} from 1.6 to 1.3 kΩ and an increase to R_{REC} from 19.5 to 33 kΩ . These values are in good agreement with the drop of R_S and increase of R_{SH} respectively. Since R_{REC} is tied to the charge accumulation at the interfaces, we can conclude that β-alanine-treated Cu:NiOx devices exhibit reduced charge trap density at the Cu:NiOx/Perovskite interface. This is also in agreement with the increased EV_{BI} in the MS analysis and improved V_{OC} that β-alanine-treated Cu:NiOx devices exhibit.

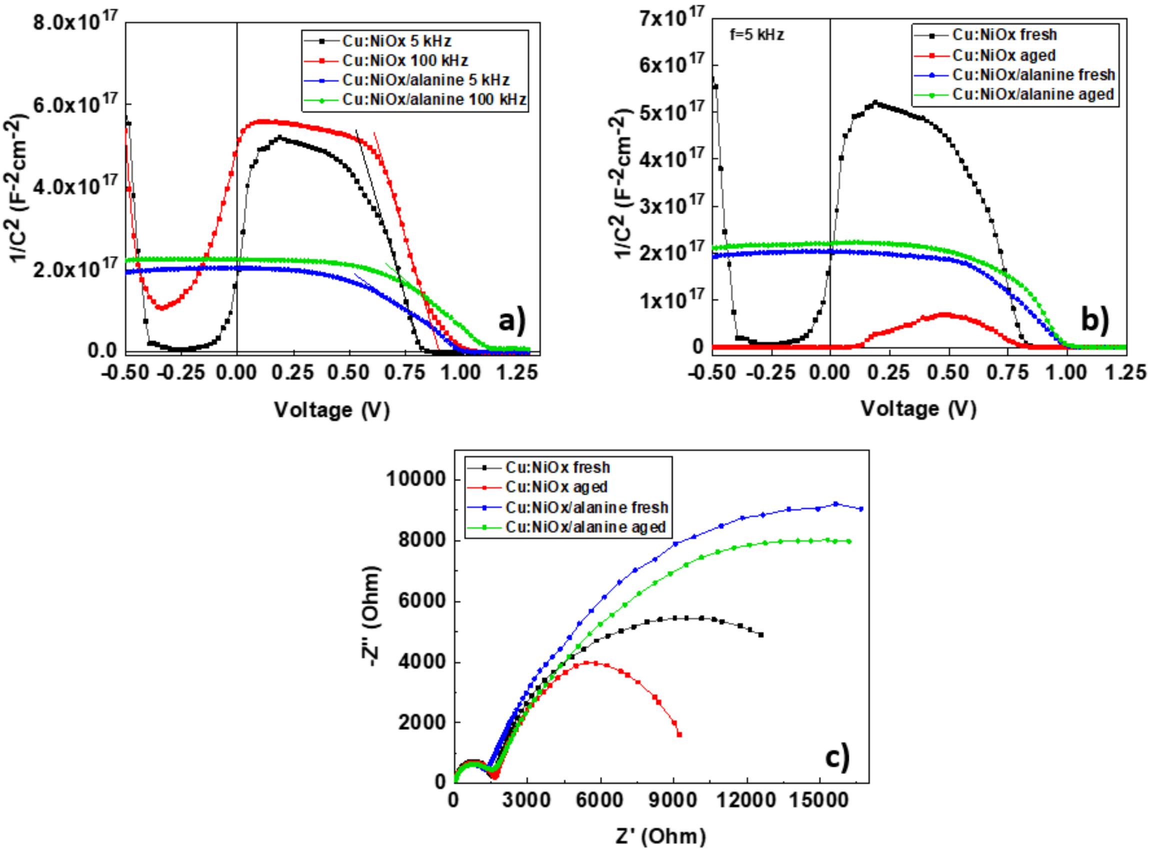

Figure 6-10: Mott-Schottky plots of a) untreated and β-alanine-treated Cu:NiOx-based devices in 5 and 100 kHz b) fresh and aged untreated an β-alanine-treated Cu:NiOx-based devices at 5 kHz, c) Nyquist plots fresh an aged untreated and β-alanine-treated Cu:NiOx-based devices.

The presence of traps in the Cu:NiOx/Pvsk interface as well as the degradation mechanisms of perovskite bulk layer can be explained by examining the nature of metal oxides. In particular, metal oxides functionality, including the Cu:NiOx under investigation within this work are known to influenced by oxygen vacancies that are caused by the impurities and the changes of stoichiometry. [157] The creation of oxygen defects within the metal-oxide is caused by loss of oxygen atoms which can serve as active sites on which oxidation or reduction take place during photocatalytic activity, or a trapping site which can inhibit and reduce the functionality of inverted PVSCs. [157] Oxygen vacancies can function as trap states themselves by inhibiting the carrier movement inside the charge-selective layer, in our case Cu:NiOx, as well as the Cu:NiOx/Pvsk interface and therefore promoting charge recombination in the interfaces of the device. Furthermore, metal oxides are known to form reactive superoxide (O_2^-)

species by adsorbing atmospheric oxygen through their vacancies and reacting with UV from ambient light. The O_2^- can further negatively impact PVSCs by deprotonating the MA^+ cation through oxidation and therefore negatively impact both PCE and cause instability by introducing charge traps in the active layer. [158] Deprotonation of the MA^+ cation was also recently reported by McGehee et. al to be caused the $Ni^{\geq 3+}$ metal cation sites in NiOx that can act both as Brønsted proton acceptors and Lewis electron acceptors and can react with the amine functional groups. This results in cation-deficient perovskite crystals, which cause poor hole extraction in the NiOx/Pvsk interface and promote charge recombination. In their work they used excess cation salts during the Pvsk active layer deposition to neutralize this effect. It is hypothesized that this happens to an extent in this case as well since alanine can function as a source of amine functional groups, similar to the MA^+ cation and therefore neutralize the effect described by McGehee at. al.[159] Through the proposed metal-oxide β-alanine treatment we have shown that the charge trap density can be reduced both at the Cu:NiOx/Pvsk interface as well as the perovskite active layer [157, 158]. The experimental results indicate the importance of the reduction of oxygen vacancies and therefore passivation of the charge traps for the development of high performance inverted PVSCs that are based on metal-oxide HTLs. By optimizing the thickness of Cu:NiOx high PCE is achieved while still retaining the improved lifetime. By decreasing the thickness of Cu:NiOx to 20 nm and by using the proposed β-alanine surface treatment, hysteresis-free devices with a PCE=15.51 % (Figure 6-11) and improved stability with T80 at 1000 h under accelerated heat conditions (60 ^oC, N_2) are developed.

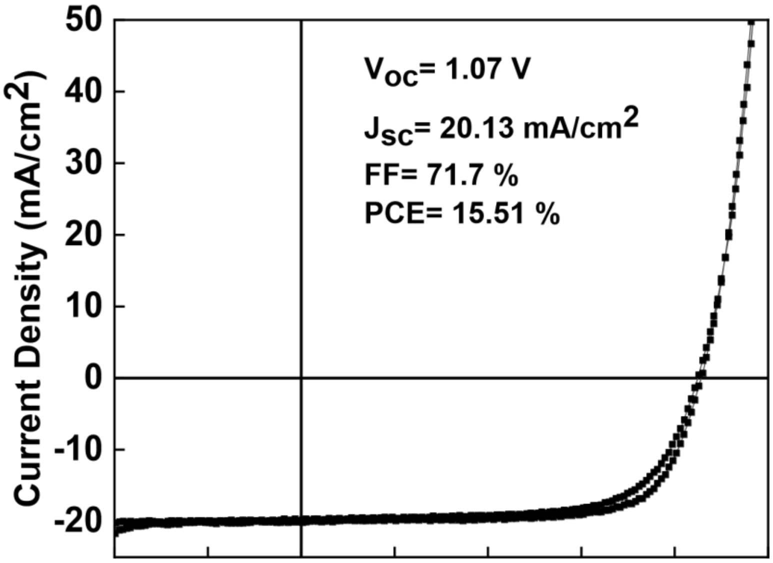

Figure 6-11: J/V characteristic of optimized ITO/Cu:NiOx/β-alanine/Pvsk/$PC_{70}BM$/BCP/Cu

6.5 Summary

It is identified that the main reason for the poor device performance and J/V hysteresis of inverted (p-i-n) PSCs incorporating Cu:NiOx HTLs to be the presence of charge traps at the bulk perovskite active layer as well as the Cu:NiOx/Pvsk interface. A β-alanine based metal-oxide surface treatment method is introduced that can improve the performance and stability of inverted PVSCs incorporating Cu:NiOx HTLs. Using β-alanine-surface treatment a reduction of interfacial charge trap density due to the formation of a more intimate Cu:NiOx/Pvsk interface is achieved, which results in improved V_{OC}. The improved J_{SC} is attributed to the reduced oxygen vacancies on β-alanine-treated Cu:NiOx HTL which leads to the reduction of the bulk perovskite active layer charge trap density. Those effects contribute to the improved PCE and stability of inverted PSCs that are using β-alanine-surface treated Cu:NiOx HTLs. Using the β-alanine metal-oxide surface treatment hysteresis-free inverted PSCs with PCE=15.51 % are reported. More importantly the thermal stability is greatly improved from 24 h for the un-treated Cu:NiOx HTL to 1000 h for the β-alanine-surface treated Cu:NiOx HTL based inverted PSCs at accelerated heat lifetime conditions in inert atmosphere (60 ^{o}C, N_2). The proposed surface treatment process using β-alanine can be applied in other functional metal oxides, thus paving the way to hysteresis-free, high performance and long-lived PSCs.

7 CONCLUDING REMARKS

7.1 Summary of results

One of the main obstacles towards commercialization of perovskite PVs is their limited lifetime performance. The interaction of the Al metal electrode with the perovskite active layer through diffusion mechanisms is the main thermal degradation mechanism for inverted perovskite solar cell under heat accelerated lifetime conditions. This Thesis first proposed that a 200 nm thick $PC_{70}BM$ diffusion blocking layer can be used to isolate the $CH_3NH_3PbI_3$ active layer from the top metal electrode, a procedure that effectively improves the device stability upon accelerating lifetime heating at 85 ^oC from 24 hours to over 168 hours. This improved thermal stability however is attained at the cost of reduced PCE due to the thick $PC_{70}BM$ fullerene buffer layer used for the isolation of the $CH_3NH_3PbI_3$ active layer from the top Al metal electrode.

This Thesis has further shown that colloidal synthesized γ-Fe_2O_3 can be effectively used to provide solution processed nanoparticulate interfacial layers within the top electrode of inverted PVSCs. Inverted PVSCs with $PC_{70}BM/Fe_2O_3/Al$ top electrode yield comparable PCE value to more conventional inverted PVSCs top electrodes such as $PC_{70}BM/Al$ and $PC_{70}BM$/AZO/Al. The proposed inverted PVSCs γ-Fe_2O_3 top electrode interface modification ($PC_{70}BM/Fe_2O_3/Al$) results in improved stability under accelerated heat conditions at 60 ^oC and N_2 atmosphere. On the contrary $PC_{70}BM$/AZO/Al device has shown the worst stability due to the deprotonation of MA^+ induced by the basic nature of ZnO compared to more acidic γ-Fe_2O_3. Overall, $PC_{70}BM/\gamma$-Fe_2O_3/Al results in less population of charge traps that potentially lie in the $PC_{70}BM/Al$ interface and, therefore, γ-Fe_2O_3 interface modification provides a better top electrode for inverted PVSCs.

As discussed above thick fullerene-based diffusion blocking layers although improve lifetime performance reduce PCE. To reduce the efficiency-stability gap of devices based on thick $PC_{70}BM$ diffusion blocking layers n-type doping of $PC_{70}BM$ to improve the electronic material conductivity was explored. By utilizing an optimal n-type doping concentration of 0.3 % w.t. N-DMBI in conjunction with thick (200 nm) $PC_{70}BM$ ETLs highly stable (T_{80}=1000 h under 60 ^OC, N_2) devices are achieved while still retaining good PCE at 13.1 %. By increasing the doping from 0.3 to 0.5 % w.t. a drop in lifetime is observed which was correlated with the promotion of I^- diffusion towards the metal electrode following the observations from the simulations by Tessler *et. al.* Retaining a good PCE was mainly a result of improved J_{SC} and FF due to the improvement of the $PC_{70}BM$ conductivity, which resulted in a decrease of R_S from 13.1 to 1.5 Ω and increase of R_{SH} from 41.7 to 50.2 kΩ. Utilizing thick $PC_{70}BM$ ETLs while still retaining a good compromise between lifetime and PCE is important for the up-scalability of p-i-n-inverted PSCs and optimized doping is essential to retain this balance. The proposed method of incorporating N-DMBI doped thick fullerene diffusion blocking layer within the inverted PSC device architecture can be in practice easily applied to roll to roll printing manufacturing process providing a simple device engineering route for achieving high performance PSCs.

Finally, many of the physical and engineering aspects that govern the behavior of hybrid perovskite photovoltaics occur at interfaces, this Thesis proposed an amino acid-based surface treatment method using β-alanine for $Cu:NiO_X$ HTLs is proposed to improve Hybrid Perovskite inverted PVs reliability and stability. It is identified that the main reason for the poor device performance and J/V hysteresis of inverted (p-i-n) PSCs incorporating Cu:NiOx HTLs to be the presence of charge traps at the bulk perovskite active layer as well as the Cu:NiOx/Pvsk interface. The introduced a β-alanine based metal-oxide surface treatment method improves the power conversion efficiency and thermal stability of inverted PVSCs incorporating Cu:NiOx HTLs. Using β-alanine-surface treatment reduced interfacial charge trap density is achieved due to the formation of a more intimate Cu:NiOx/Pvsk interface, which results in improved V_{OC} . The improved J_{SC} is attributed to the reduced oxygen vacancies on β-alanine-treated Cu:NiOx HTL which leads to the reduction of the bulk perovskite active layer charge trap density. The work included in this Thesis reported hysteresis-free inverted PSCs with PCE=15.51 %. More importantly the thermal stability is greatly improved from 24 h for the un-treated Cu:NiOx HTL to 1000 h for the β-alanine-surface treated Cu:NiOx HTL based inverted PSCs at accelerated heat lifetime conditions in inert atmosphere (60 ^oC, N_2).

7.2 Future perspectives

7.2.1 Perovskite solar cells based on $FAPbI_3$ and $CsPbI_3$ nanocrystals

In parallel to hybrid perovskite based electronic materials, Perovskite nanocrystals (PNCs) have attracted tremendous attention over the years for both LEDs and solar cells applications. Several inherent material properties are desirable for perovskite nanocrystal based optoelectronic applications such as high photoluminescence quantum yield (PLQY) [160] as well as the minimization of radiative recombination processes. [161] Furthermore, PNCs show relatively high defect tolerance and tenability of the band gap due to the easy control of the size of the nanoparticles (NPs).[162] In parallel to the detailed hybrid perovskite PVs work presented within this Thesis initial studies on perovskite nanocrystal $FAPbI_3$ and $CsPbI_3$ solar cells were also performed. Specifically, the photovoltaic (PV) performance of $FAPbI_3$ and $CsPbI_3$ in various processing conditions such as in ambient and inert fabrication atmospheres as well as introducing several ligands washing (LW) steps were evaluated.

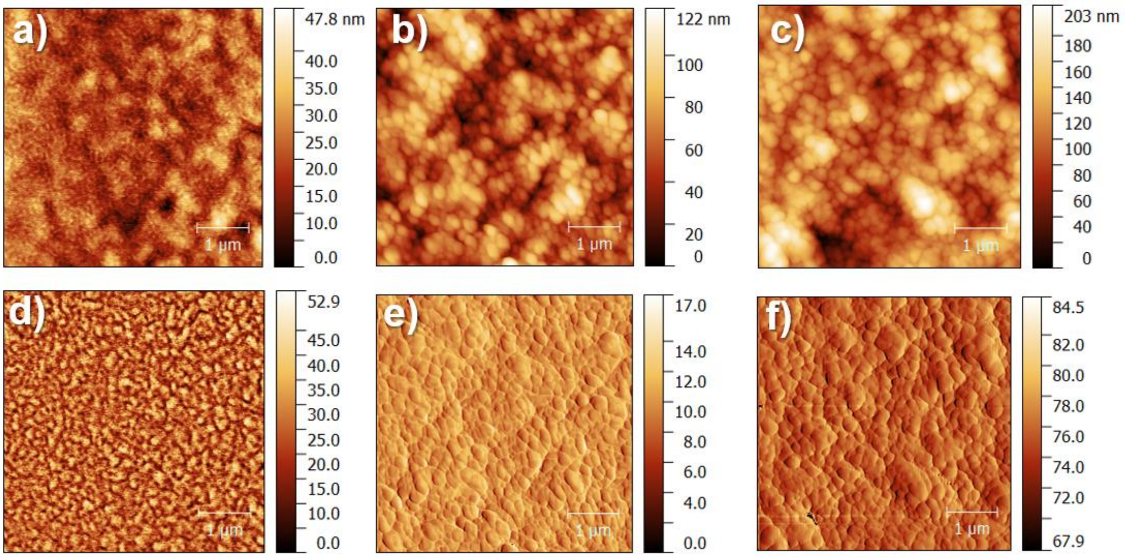

Figure 7-1: Topographical images of: a) $FAPbI_3$ pristine, b) $FAPbI_3$ FAI washing, c) $FAPbI_3$ FAI+EtAc washing. Phase contrast image of d) $FAPbI_3$ pristine, e) $FAPbI_3$ FAI washing, f) $FAPbI_3$ FAI+EtAc washing.

Based on the previous published work from *Luther et. al* we have based the studies around the concept of introducing a ligand washing step with FAI in EtAc on top of the PNC active layer in order to ensure proper washing of the oleic acid ligands. [163] AFM measurements were performed for ITO/$FAPbI_3$ films in three different conditions:

pristine, FAI washing and FAI+EtAc washing. From the AFM images we see enlargement of grain size upon washing with FAI and FAI+ EtAc. Treating the films with EtAc results in agglomeration of the NPs and therefore enlargement of grain size.

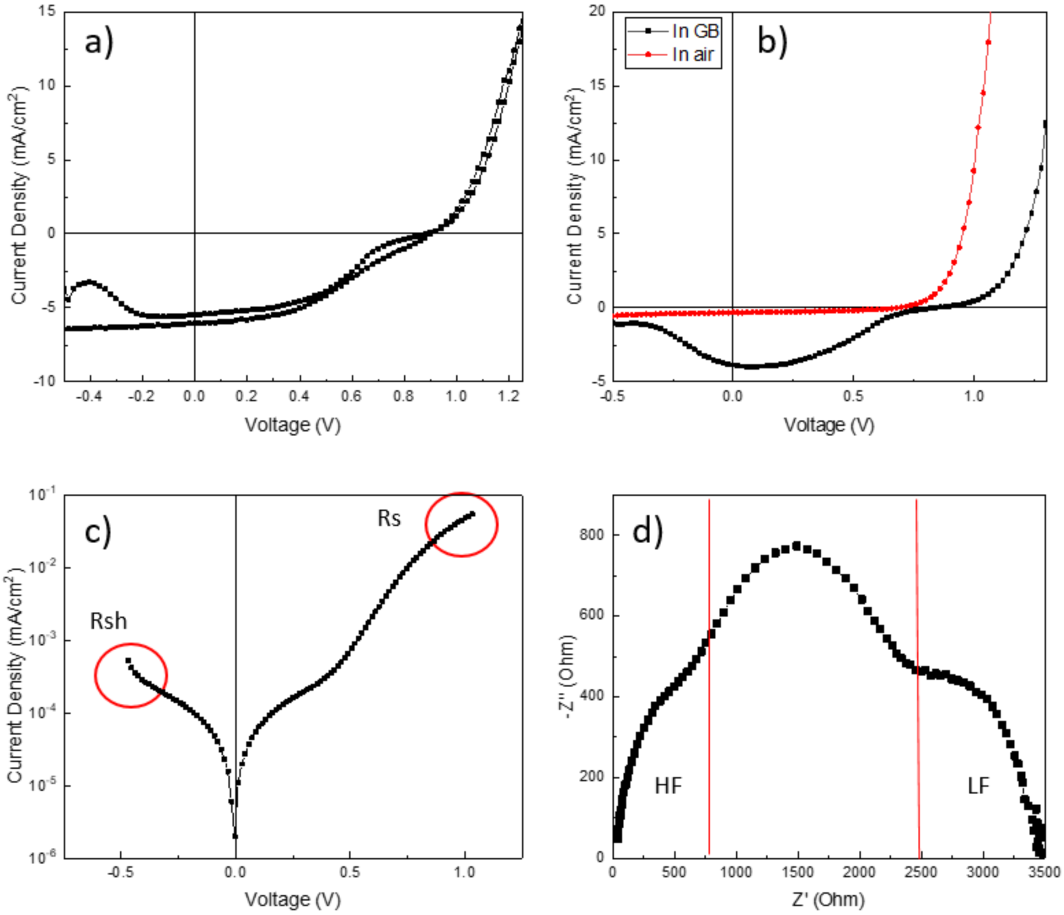

Figure 7-2: a) J/V curves for the champion device, b) J/V curves in inert and ambient conditions, c) dark J/V and d) Nyquist plots.

Perovskite nanocrystal based solar cell devices were fabricated based on a planar normal PV structure of ITO/TiO_2/$FAPbI_3$/MoO_3/Al. The active layer was treated with a combination of FAI in EtAc and pristine EtAc to ensure proper LW and remove the oleic acid ligands. The above process was repeated 3 times since previous experiments found that provide improved performance. The PV parameters are shown in Table 7-1. The maximum PCE achieved with $FAPbI_3$ devices was 1.93 % utilizing 3 LW steps. Comparing the devices fabricated in ambient conditions with devices in inert conditions we see that their PCE is significantly lower (0.09 %), primarily due to a drop in V_{OC} and J_{SC}. Studying the dark J/V plots and impedance spectroscopy we deduce that the low J_{SC} that is observed in $FAPbI_3$ base devices is a result of the high R_S, which can be a result of improper LW and residual oleic acid ligands. This is further shown in the Nyquist plots where a parasitic resistance manifests between high and low frequency (HF and LF) regimes.

Solar cell devices were also fabricated based on a planar normal structure of ITO/TiO_2/$CsPbI_3$/MoO_3/Al. The active layer was treated with a combination of FAI in EtAc and pristine EtAc to ensure proper LW and remove the oleic acid ligands. This process was repeated 3 times, which was previously found to be the optimum. The PV parameters are shown in Table 1.

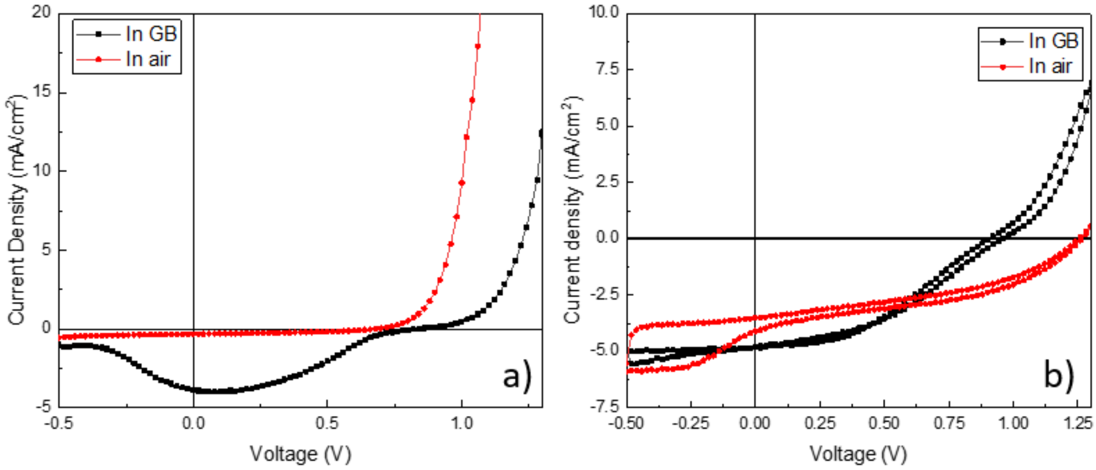

Figure 7-3: Devices based in GB and air for a) $FAPbI_3$ based devices and b) $CsPbI_3$ based devices

Comparing devices that were fabricated in inert and ambient conditions we can see that devices based on $CsPbI_3$ give similar PCEs (~1.8 %), although the devices in ambient conditions are less reproducible. On the other hand, devices based on $FaPbI_3$ exhibit a significant drop to the PCE from 1.14% (1.93 % champion) to 0.09 %.

Table 7-1: PNCs PV parameters

Device architecture	V_{oc} (V)	J_{sc} (mA/cm^2)	FF (%)	PCE (%)
ITO/TiO_2/$FAPbI_3$/MoO_3/Al (champion)	0.88	5.45	40.4	1.93
ITO/TiO_2/$FAPbI_3$/MoO_3/Al (inert)	0.84	3.85	35.4	1.14
ITO/TiO_2/$FAPbI_3$/MoO_3/Al (ambient)	0.68	0.32	40.3	0.09
ITO/TiO_2/$CsPbI_3$/MoO_3/Al (inert)	0.96	4.78	39.4	1.81
ITO/TiO_2/$CsPbI_3$/MoO_3/Al (ambient)	1.26	3.50	42.3	1.87

Following the initial experimental work on PNC solar cells the high R_S and low J_{SC} were identified as the main limiting factors for the low PCE. Two limiting factors that were identified were the limited conductivity due to improper LW of oleic acid and the inherently high charge recombination due to the quantum confinement effect of the NCs. To tackle these issues several ideas are explored currently. In detail, different weaker-bound ligands such as DDAB are explored as an alternative to oleic acid as well as optimization of the LW procedure by using different combinations of EtAc with other precursors such as CsI. Furthermore, in order to improve the electron extraction and NC based active layer light harvesting capabilities, devices incorporating a bulk heterojunction structure involving a mixture of NCs and molecular based electron acceptors will be investigated. Some of the options that will be explored is mixing the NCs with the commonly used PCBM as well as non-fullerene acceptors such as Y6 aiming to further improve NCs based PVs performance. Furthermore, by utilizing Y6, absorption at lower energy wavelengths (~950 nm) can be achieved compared to both $FAPbI_3$ (~775 nm) and $CsPbI_3$ (~650 nm), therefore improving the light harvesting capabilities of the PNC active layer. [164]

APPENDIX

1. Publications

A) Publications directly related to this Thesis

Galatopoulos, F., Papadas, I. T., Armatas, G. S. & Choulis, S. A. “Long Thermal Stability of Inverted Perovskite Photovoltaics Incorporating Fullerene-Based Diffusion Blocking Layer” *Adv. Mater. Interfaces* **5**, 1800280 (2018)

Papadas, I. T., Galatopoulos, F., Armatas, G. S., Tessler, N. & Choulis, S. A. Top Electrode Interface Modification Improves the Thermal Stability of Inverted Perovskite Photovoltaics. *J. Phys. Chem. C* (2019).

Galatopoulos, F., Papadas, I. T., Ioakeimidis, A., Eleftheriou, P. & Choulis, S. A. Surface Treatment of Cu:NiOx Hole-Transporting Layer Using β-Alanine for Hysteresis-Free and Thermally Stable Inverted Perovskite Solar Cells. *Nanomaterials* **10**, 1961 (2020).

Galatopoulos, F. Tessler, N., Choulis S.A., High Performance Inverted Perovskite Solar Cells Incorporating Doped Fullerene Difusion Blocking Layer [To be submitted].

B) Publications related with the research activity within the MEP group

Galatopoulos, F., Savva, A., Papadas, I. T. & Choulis, S. A. “The effect of hole transporting layer in charge accumulation properties of p-i-n perovskite solar cells” *APL Mater.* **5**, 076102 (2017)

Savva, A.. Papadas I.T., Tsikritzis, D., Ioakeimidis, A., Galatopoulos, F., Kapnisis, K., Fuhrer, R., Hartmeier, B., Oszajca, M.F., Luechinger, N.A., Kennou, S., Armatas, G.S. & Choulis, S. A “Inverted Perovskite Photovoltaics Using Flame Spray Pyrolysis Solution Based CuAlO 2 /Cu–O Hole-Selective Contact” *ACS Appl. Energy Mater.* **2**, 2276–2287 (2019).

2. Conference presentations

Galatopoulos, F., Papadas, I.T. & Choulis, S.A. "Thermal degradation mechanisms of perovskite photovoltaics under accelerated heat lifetime conditions", *SEPV 2018 Stability of Emerging Photovoltaics from Fundamental to Applications, Barcelona, Spain,* (2018). [Poster presentation]

Galatopoulos, F., Papadas, I.T., Armatas, G.S. & Choulis, S.A. "Long Thermal Stability of Inverted Perovskite Photovoltaics Incorporating Fullerene-based Diffusion Blocking Layer", *XXXIII Panhellenic Conference on Solid State Physics and Materials Science, Nicosia, Cyprus*, (2018)**.** [Poster presentation]

Galatopoulos, F., Papadas, I.T., Armatas, G.S. & Choulis, S.A. "Long Thermal Stability of Inverted Perovskite Photovoltaics Incorporating Fullerene-based Diffusion Blocking Layer", *Next-Gen IV: PV Materials, Groningen, Netherlands*, (2019). [Poster presentation]

Galatopoulos, F., Papadas, I.T., Ioakeimides, A., Eleftheriou, P. Choulis, S.A., "Surface Treatment of Cu:NiOx Hole-Transporting Layer Using β-Alanine for Hysteresis Free and Thermally Stable Inverted Perovskite Photovoltaics", *nanoGe Fall Meeting 20*, 2020. [Poster Presentation]

F. Galatopoulos , P. Papagiorgis , A. Z. Chrusou , C. Bernasconi , C. Christodoulou , M. I. Bodnarchuk , M. V. Kovalenko , G. Itskos and S. A. Choulis, "Colloidal Perovskite Nanomaterials Processing and Photovoltaic Loss Analysis" , *nanoGe Spring Meeting 2022.* [Poster Presentation]

REFERENCES

1. Fraas, L. M. *Low-Cost Solar Electric Power*. (Springer International Publishing, 2014). doi:10.1007/978-3-319-07530-3
2. Seger, B. Global Energy Consumption: The Numbers for Now and in the Future. (2016).
3. Szabo, L. The history of using solar energy. in *2017 International Conference on Modern Power Systems (MPS)* 1–8 (IEEE, 2017). doi:10.1109/MPS.2017.7974451
4. Gray, J. L. *Handbook of Photovoltaic Science and Engineering*.
5. Green, M. Solar cells—Operating principles, technology and system applications. *Sol. Energy* **28**, 447 (1982).
6. *Solar Cells - Silicon Wafer-Based Technologies*. (InTech, 2011). doi:10.5772/1758
7. NREL PV efficiency chart 2019.
8. Kuhlmann, A. M. The Second Most Abundant Element in the Earth's Crust. *JOM* **15**, 502–505 (1963).
9. Sampaio, P. G. V. & González, M. O. A. Photovoltaic solar energy: Conceptual framework. *Renew. Sustain. Energy Rev.* **74**, 590–601 (2017).
10. Luceño-Sánchez, J., Díez-Pascual, A. & Peña Capilla, R. Materials for Photovoltaics: State of Art and Recent Developments. *Int. J. Mol. Sci.* **20**, 976 (2019).
11. Green, M. A. *et al.* Solar cell efficiency tables (version 50). *Prog. Photovoltaics Res. Appl.* **25**, 668–676 (2017).
12. Chopra, K. L., Paulson, P. D. & Dutta, V. Thin-film solar cells: an overview. *Prog. Photovoltaics Res. Appl.* **12**, 69–92 (2004).
13. Feurer, T. *et al.* Progress in thin film CIGS photovoltaics - Research and development, manufacturing, and applications. *Prog. Photovoltaics Res. Appl.*

25, 645–667 (2017).

14. Green, M. A. Third generation photovoltaics: Ultra-high conversion efficiency at low cost. *Prog. Photovoltaics Res. Appl.* **9**, 123–135 (2001).
15. *Organic-Inorganic Halide Perovskite Photovoltaics*. (Springer International Publishing, 2016). doi:10.1007/978-3-319-35114-8
16. Fu, Q. *et al.* Recent Progress on the Long-Term Stability of Perovskite Solar Cells. *Adv. Sci.* **5**, 1700387 (2018).
17. Marinova, N., Valero, S. & Delgado, J. L. Organic and perovskite solar cells: Working principles, materials and interfaces. *J. Colloid Interface Sci.* **488**, 373–389 (2017).
18. Ossila. Perovskite crystal phases.
19. Poglitsch, A. & Weber, D. Dynamic disorder in methylammoniumtrihalogenoplumbates (II) observed by millimeter-wave spectroscopy. *J. Chem. Phys.* **87**, 6373–6378 (1987).
20. Weller, M. T., Weber, O. J., Henry, P. F., Di Pumpo, A. M. & Hansen, T. C. Complete structure and cation orientation in the perovskite photovoltaic methylammonium lead iodide between 100 and 352 K. *Chem. Commun.* **51**, 4180–4183 (2015).
21. Kojima, A., Teshima, K., Shirai, Y. & Miyasaka, T. Organometal Halide Perovskites as Visible-Light Sensitizers for Photovoltaic Cells. *J. Am. Chem. Soc.* **131**, 6050–6051 (2009).
22. Lee, M. M., Teuscher, J., Miyasaka, T., Murakami, T. N. & Snaith, H. J. Efficient Hybrid Solar Cells Based on Meso-Superstructured Organometal Halide Perovskites. *Science (80-.).* **338**, 643–647 (2012).
23. Eperon, G. E. *et al.* Formamidinium lead trihalide: a broadly tunable perovskite for efficient planar heterojunction solar cells. *Energy Environ. Sci.* **7**, 982 (2014).
24. Liu, Y. *et al.* Understanding Interface Engineering for High-Performance Fullerene/Perovskite Planar Heterojunction Solar Cells. *Adv. Energy Mater.* **6**, 1501606 (2016).

25. Chen, B., Yang, M., Priya, S. & Zhu, K. Origin of J – V Hysteresis in Perovskite Solar Cells. *J. Phys. Chem. Lett.* **7**, 905–917 (2016).

26. Savva, A., Burgués-Ceballos, I. & Choulis, S. A. Improved Performance and Reliability of p-i-n Perovskite Solar Cells via Doped Metal Oxides. *Adv. Energy Mater.* **6**, 1600285 (2016).

27. Miyata, A. *et al.* Direct measurement of the exciton binding energy and effective masses for charge carriers in organic–inorganic tri-halide perovskites. *Nat. Phys.* **11**, 582–587 (2015).

28. Wehrenfennig, C., Eperon, G. E., Johnston, M. B., Snaith, H. J. & Herz, L. M. High Charge Carrier Mobilities and Lifetimes in Organolead Trihalide Perovskites. *Adv. Mater.* **26**, 1584–1589 (2014).

29. Zhou, D., Zhou, T., Tian, Y., Zhu, X. & Tu, Y. Perovskite-Based Solar Cells: Materials, Methods, and Future Perspectives. *J. Nanomater.* **2018**, 1–15 (2018).

30. Leijtens, T., Lauber, B., Eperon, G. E., Stranks, S. D. & Snaith, H. J. The Importance of Perovskite Pore Filling in Organometal Mixed Halide Sensitized TiO 2 -Based Solar Cells. *J. Phys. Chem. Lett.* **5**, 1096–1102 (2014).

31. Saliba, M. *et al.* Incorporation of rubidium cations into perovskite solar cells improves photovoltaic performance. *Science (80-.).* **354**, 206–209 (2016).

32. Futscher, M. H. *et al.* Quantification of ion migration in CH 3 NH 3 PbI 3 perovskite solar cells by transient capacitance measurements. *Mater. Horizons* **6**, 1497–1503 (2019).

33. Chueh, C.-C., Li, C.-Z. & Jen, A. K.-Y. Recent progress and perspective in solution-processed Interfacial materials for efficient and stable polymer and organometal perovskite solar cells. *Energy Environ. Sci.* **8**, 1160–1189 (2015).

34. Min, H. *et al.* Perovskite solar cells with atomically coherent interlayers on SnO2 electrodes. *Nature* **598**, 444–450 (2021).

35. Shen, H. *et al.* Metal halide perovskite: a game-changer for photovoltaics and solar devices via a tandem design. *Sci. Technol. Adv. Mater.* **19**, 53–75 (2018).

36. Wang, R. *et al.* A Review of Perovskites Solar Cell Stability. *Adv. Funct. Mater.* 1808843 (2019). doi:10.1002/adfm.201808843

37. Kwon, Y. S., Lim, J., Yun, H.-J., Kim, Y.-H. & Park, T. A diketopyrrolopyrrole-containing hole transporting conjugated polymer for use in efficient stable organic–inorganic hybrid solar cells based on a perovskite. *Energy Environ. Sci.* **7**, 1454 (2014).

38. Liu, J. *et al.* A dopant-free hole-transporting material for efficient and stable perovskite solar cells. *Energy Environ. Sci.* **7**, 2963–2967 (2014).

39. Chen, B., Wang, S., Song, Y., Li, C. & Hao, F. A critical review on the moisture stability of halide perovskite films and solar cells. *Chem. Eng. J.* **430**, 132701 (2022).

40. Cao, J. *et al.* Thiols as interfacial modifiers to enhance the performance and stability of perovskite solar cells. *Nanoscale* **7**, 9443–9447 (2015).

41. Fang, R. *et al.* [6,6]-Phenyl-C 61 -Butyric Acid Methyl Ester/Cerium Oxide Bilayer Structure as Efficient and Stable Electron Transport Layer for Inverted Perovskite Solar Cells. *ACS Nano* **12**, 2403–2414 (2018).

42. Kore, B. P., Zhang, W., Hoogendoorn, B. W., Safdari, M. & Gardner, J. M. Moisture tolerant solar cells by encapsulating 3D perovskite with long-chain alkylammonium cation-based 2D perovskite. *Commun. Mater.* **2**, 100 (2021).

43. Aristidou, N. *et al.* The Role of Oxygen in the Degradation of Methylammonium Lead Trihalide Perovskite Photoactive Layers. *Angew. Chemie Int. Ed.* **54**, 8208–8212 (2015).

44. Duan, L. & Uddin, A. Defects and stability of perovskite solar cells: a critical analysis. *Mater. Chem. Front.* **6**, 400–417 (2022).

45. Leijtens, T. *et al.* Overcoming ultraviolet light instability of sensitized TiO2 with meso-superstructured organometal tri-halide perovskite solar cells. *Nat. Commun.* **4**, 2885 (2013).

46. Bryant, D. *et al.* Light and oxygen induced degradation limits the operational stability of methylammonium lead triiodide perovskite solar cells. *Energy Environ. Sci.* **9**, 1655–1660 (2016).

47. Arora, N. *et al.* Perovskite solar cells with CuSCN hole extraction layers yield stabilized efficiencies greater than 20%. *Science (80-.).* **358**, 768–771 (2017).

48. Conings, B. *et al.* Intrinsic Thermal Instability of Methylammonium Lead Trihalide Perovskite. *Adv. Energy Mater.* **5**, 1500477 (2015).

49. Lee, J.-W., Seol, D.-J., Cho, A.-N. & Park, N.-G. High-Efficiency Perovskite Solar Cells Based on the Black Polymorph of HC(NH 2) 2 PbI 3. *Adv. Mater.* **26**, 4991–4998 (2014).

50. Zhao, X., Kim, H.-S., Seo, J.-Y. & Park, N.-G. Effect of Selective Contacts on the Thermal Stability of Perovskite Solar Cells. *ACS Appl. Mater. Interfaces* **9**, 7148–7153 (2017).

51. Domanski, K. *et al.* Not All That Glitters Is Gold: Metal-Migration-Induced Degradation in Perovskite Solar Cells. *ACS Nano* **10**, 6306–6314 (2016).

52. Thambidurai, M. *et al.* Enhanced Thermal Stability of Planar Perovskite Solar Cells Through Triphenylphosphine Interface Passivation. *ChemSusChem* **15**, (2022).

53. Amat, A. *et al.* Cation-Induced Band-Gap Tuning in Organohalide Perovskites: Interplay of Spin–Orbit Coupling and Octahedra Tilting. *Nano Lett.* **14**, 3608–3616 (2014).

54. Misra, R. K. *et al.* Temperature- and Component-Dependent Degradation of Perovskite Photovoltaic Materials under Concentrated Sunlight. *J. Phys. Chem. Lett.* **6**, 326–330 (2015).

55. Jesper Jacobsson, T. *et al.* Exploration of the compositional space for mixed lead halogen perovskites for high efficiency solar cells. *Energy Environ. Sci.* **9**, 1706–1724 (2016).

56. D’Innocenzo, V. *et al.* Excitons versus free charges in organo-lead tri-halide perovskites. *Nat. Commun.* **5**, 3586 (2014).

57. Lee, J.-W. *et al.* Formamidinium and Cesium Hybridization for Photo- and Moisture-Stable Perovskite Solar Cell. *Adv. Energy Mater.* **5**, 1501310 (2015).

58. Koh, T. M. *et al.* Formamidinium-Containing Metal-Halide: An Alternative Material for Near-IR Absorption Perovskite Solar Cells. *J. Phys. Chem. C* **118**, 16458–16462 (2014).

59. Binek, A., Hanusch, F. C., Docampo, P. & Bein, T. Stabilization of the Trigonal

High-Temperature Phase of Formamidinium Lead Iodide. *J. Phys. Chem. Lett.* **6**, 1249–1253 (2015).

60. Yi, C. *et al.* Entropic stabilization of mixed A-cation ABX 3 metal halide perovskites for high performance perovskite solar cells. *Energy Environ. Sci.* **9**, 656–662 (2016).

61. Deepa, M. *et al.* Cesium power: low Cs + levels impart stability to perovskite solar cells. *Phys. Chem. Chem. Phys.* **19**, 4069–4077 (2017).

62. Saliba, M. *et al.* Cesium-containing triple cation perovskite solar cells: improved stability, reproducibility and high efficiency. *Energy Environ. Sci.* **9**, 1989–1997 (2016).

63. Hao, F., Stoumpos, C. C., Cao, D. H., Chang, R. P. H. & Kanatzidis, M. G. Lead-free solid-state organic–inorganic halide perovskite solar cells. *Nat. Photonics* **8**, 489–494 (2014).

64. Xing, G. *et al.* Long-Range Balanced Electron- and Hole-Transport Lengths in Organic-Inorganic CH3NH3PbI3. *Science (80-.).* **342**, 344–347 (2013).

65. Eperon, G. E., Burlakov, V. M., Docampo, P., Goriely, A. & Snaith, H. J. Morphological Control for High Performance, Solution-Processed Planar Heterojunction Perovskite Solar Cells. *Adv. Funct. Mater.* **24**, 151–157 (2014).

66. Stranks, S. D. *et al.* Electron-Hole Diffusion Lengths Exceeding 1 Micrometer in an Organometal Trihalide Perovskite Absorber. *Science (80-.).* **342**, 341–344 (2013).

67. Aharon, S., Cohen, B. El & Etgar, L. Hybrid Lead Halide Iodide and Lead Halide Bromide in Efficient Hole Conductor Free Perovskite Solar Cell. *J. Phys. Chem. C* **118**, 17160–17165 (2014).

68. Wang, D. *et al.* Reproducible One-Step Fabrication of Compact MAPbI 3– x Cl x Thin Films Derived from Mixed-Lead-Halide Precursors. *Chem. Mater.* **26**, 7145–7150 (2014).

69. Chen, Y., Li, B., Huang, W., Gao, D. & Liang, Z. Efficient and reproducible CH 3 NH 3 PbI 3−x (SCN) x perovskite based planar solar cells. *Chem. Commun.* **51**, 11997–11999 (2015).

70. Yan, J., Qiu, W., Wu, G., Heremans, P. & Chen, H. Recent progress in 2D/quasi-2D layered metal halide perovskites for solar cells. *J. Mater. Chem. A* **6**, 11063–11077 (2018).

71. Quan, L. N. *et al.* Ligand-Stabilized Reduced-Dimensionality Perovskites. *J. Am. Chem. Soc.* **138**, 2649–2655 (2016).

72. Smith, I. C., Hoke, E. T., Solis-Ibarra, D., McGehee, M. D. & Karunadasa, H. I. A Layered Hybrid Perovskite Solar-Cell Absorber with Enhanced Moisture Stability. *Angew. Chemie Int. Ed.* **53**, 11232–11235 (2014).

73. Pereyra, C., Xie, H. & Lira-Cantu, M. Additive engineering for stable halide perovskite solar cells. *J. Energy Chem.* **60**, 599–634 (2021).

74. Zhang, Y. *et al.* Propylammonium Chloride Additive for Efficient and Stable FAPbI 3 Perovskite Solar Cells. *Adv. Energy Mater.* **11**, 2102538 (2021).

75. Saliba, M. *et al.* A molecularly engineered hole-transporting material for efficient perovskite solar cells. *Nat. Energy* **1**, 15017 (2016).

76. Abate, A. *et al.* Lithium salts as “redox active” p-type dopants for organic semiconductors and their impact in solid-state dye-sensitized solar cells. *Phys. Chem. Chem. Phys.* **15**, 2572 (2013).

77. Mengistie, D. A., Ibrahem, M. A., Wang, P.-C. & Chu, C.-W. Highly Conductive PEDOT:PSS Treated with Formic Acid for ITO-Free Polymer Solar Cells. *ACS Appl. Mater. Interfaces* **6**, 2292–2299 (2014).

78. Sun, W. *et al.* Solution-Processed Copper Iodide as an Inexpensive and Effective Anode Buffer Layer for Polymer Solar Cells. *J. Phys. Chem. C* **118**, 16806–16812 (2014).

79. Conings, B. *et al.* Perovskite-Based Hybrid Solar Cells Exceeding 10% Efficiency with High Reproducibility Using a Thin Film Sandwich Approach. *Adv. Mater.* **26**, 2041–2046 (2014).

80. Yang, W. S. *et al.* High-performance photovoltaic perovskite layers fabricated through intramolecular exchange. *Science (80-.).* **348**, 1234–1237 (2015).

81. Yang, W. S. *et al.* Iodide management in formamidinium-lead-halide–based perovskite layers for efficient solar cells. *Science (80-.).* **356**, 1376–1379 (2017).

82. You, J. *et al.* Improved air stability of perovskite solar cells via solution-processed metal oxide transport layers. *Nat. Nanotechnol.* **11**, 75–81 (2016).

83. Kim, J. H. *et al.* High-Performance and Environmentally Stable Planar Heterojunction Perovskite Solar Cells Based on a Solution-Processed Copper-Doped Nickel Oxide Hole-Transporting Layer. *Adv. Mater.* **27**, 695–701 (2015).

84. Galatopoulos, F., Savva, A., Papadas, I. T. & Choulis, S. A. The effect of hole transporting layer in charge accumulation properties of p-i-n perovskite solar cells. *APL Mater.* **5**, 076102 (2017).

85. Qin, P. *et al.* Inorganic hole conductor-based lead halide perovskite solar cells with 12.4% conversion efficiency. *Nat. Commun.* **5**, 3834 (2014).

86. Savva, A. *et al.* Inverted Perovskite Photovoltaics Using Flame Spray Pyrolysis Solution Based CuAlO 2 /Cu–O Hole-Selective Contact. *ACS Appl. Energy Mater.* **2**, 2276–2287 (2019).

87. Papadas, I. T. *et al.* Employing surfactant-assisted hydrothermal synthesis to control CuGaO 2 nanoparticle formation and improved carrier selectivity of perovskite solar cells. *Mater. Today Energy* **8**, 57–64 (2018).

88. Papadas, I. T., Ioakeimidis, A., Armatas, G. S. & Choulis, S. A. Low-Temperature Combustion Synthesis of a Spinel NiCo 2 O 4 Hole Transport Layer for Perovskite Photovoltaics. *Adv. Sci.* **5**, 1701029 (2018).

89. Ioakeimidis, A. *et al.* Enhanced photovoltaic performance of perovskite solar cells by Co-doped spinel nickel cobaltite hole transporting layer. *APL Mater.* **7**, 021101 (2019).

90. Habisreutinger, S. N. *et al.* Carbon Nanotube/Polymer Composites as a Highly Stable Hole Collection Layer in Perovskite Solar Cells. *Nano Lett.* **14**, 5561–5568 (2014).

91. Yeo, J.-S. *et al.* Highly efficient and stable planar perovskite solar cells with reduced graphene oxide nanosheets as electrode interlayer. *Nano Energy* **12**, 96–104 (2015).

92. Liu, M., Johnston, M. B. & Snaith, H. J. Efficient planar heterojunction perovskite solar cells by vapour deposition. *Nature* **501**, 395–398 (2013).

93. Burschka, J. *et al.* Sequential deposition as a route to high-performance perovskite-sensitized solar cells. *Nature* **499**, 316–319 (2013).

94. Pathak, S. K. *et al.* Performance and Stability Enhancement of Dye-Sensitized and Perovskite Solar Cells by Al Doping of TiO 2. *Adv. Funct. Mater.* **24**, 6046–6055 (2014).

95. Ito, S., Tanaka, S., Manabe, K. & Nishino, H. Effects of Surface Blocking Layer of Sb 2 S 3 on Nanocrystalline TiO 2 for CH 3 NH 3 PbI 3 Perovskite Solar Cells. *J. Phys. Chem. C* **118**, 16995–17000 (2014).

96. Hu, T. *et al.* Indium-Free Perovskite Solar Cells Enabled by Impermeable Tin-Oxide Electron Extraction Layers. *Adv. Mater.* **29**, 1606656 (2017).

97. Brinkmann, K. O. *et al.* Suppressed decomposition of organometal halide perovskites by impermeable electron-extraction layers in inverted solar cells. *Nat. Commun.* **8**, 13938 (2017).

98. Wang, Z. *et al.* Efficient and Air-Stable Mixed-Cation Lead Mixed-Halide Perovskite Solar Cells with n-Doped Organic Electron Extraction Layers. *Adv. Mater.* **29**, 1604186 (2017).

99. Zhao, J. *et al.* Is Cu a stable electrode material in hybrid perovskite solar cells for a 30-year lifetime? *Energy Environ. Sci.* **9**, 3650–3656 (2016).

100. Zhou, H. *et al.* Hole-Conductor-Free, Metal-Electrode-Free TiO 2 /CH 3 NH 3 PbI 3 Heterojunction Solar Cells Based on a Low-Temperature Carbon Electrode. *J. Phys. Chem. Lett.* **5**, 3241–3246 (2014).

101. Zhang, H. *et al.* High-efficiency (>20%) planar carbon-based perovskite solar cells through device configuration engineering. *J. Colloid Interface Sci.* **608**, 3151–3158 (2022).

102. Krebs, F. C. Fabrication and processing of polymer solar cells: A review of printing and coating techniques. *Sol. Energy Mater. Sol. Cells* **93**, 394–412 (2009).

103. Tang, Z. Studies of Inverted Organic Solar Cells Fabricated by Doctor Blading Technique. (Linkopings Universitet, 2010).

104. Ossila. Solar Cells: A Guide to Theory and Measurement.

105. Pearson, A. J. *et al.* Oxygen Degradation in Mesoporous Al 2 O 3 /CH 3 NH 3 PbI 3- x Cl x Perovskite Solar Cells: Kinetics and Mechanisms. *Adv. Energy Mater.* **6**, 1600014 (2016).

106. Glatthaar, M. *et al.* Efficiency limiting factors of organic bulk heterojunction solar cells identified by electrical impedance spectroscopy. *Sol. Energy Mater. Sol. Cells* **91**, 390–393 (2007).

107. Shao, S. *et al.* Elimination of the light soaking effect and performance enhancement in perovskite solar cells using a fullerene derivative. *Energy Environ. Sci.* **9**, 2444–2452 (2016).

108. Hermerschmidt, F. *et al.* Influence of the Hole Transporting Layer on the Thermal Stability of Inverted Organic Photovoltaics Using Accelerated-Heat Lifetime Protocols. *ACS Appl. Mater. Interfaces* **9**, 14136–14144 (2017).

109. Bag, M. *et al.* Kinetics of Ion Transport in Perovskite Active Layers and Its Implications for Active Layer Stability. *J. Am. Chem. Soc.* **137**, 13130–13137 (2015).

110. Guerrero, A. *et al.* Properties of Contact and Bulk Impedances in Hybrid Lead Halide Perovskite Solar Cells Including Inductive Loop Elements. *J. Phys. Chem. C* **120**, 8023–8032 (2016).

111. Guerrero, A. *et al.* Interfacial Degradation of Planar Lead Halide Perovskite Solar Cells. *ACS Nano* **10**, 218–224 (2016).

112. Back, H. *et al.* Achieving long-term stable perovskite solar cells via ion neutralization. *Energy Environ. Sci.* **9**, 1258–1263 (2016).

113. Bi, E. *et al.* Diffusion engineering of ions and charge carriers for stable efficient perovskite solar cells. *Nat. Commun.* **8**, 15330 (2017).

114. Zhang, G. *et al.* Extensive Penetration of Evaporated Electrode Metals into Fullerene Films: Intercalated Metal Nanostructures and Influence on Device Architecture. *ACS Appl. Mater. Interfaces* **7**, 25247–25258 (2015).

115. Akbulatov, A. F. *et al.* Effect of Electron-Transport Material on Light-Induced Degradation of Inverted Planar Junction Perovskite Solar Cells. *Adv. Energy Mater.* **7**, 1700476 (2017).

116. Papadas, I. T., Galatopoulos, F., Armatas, G. S., Tessler, N. & Choulis, S. A. Top Electrode Interface Modification Improves the Thermal Stability of Inverted Perovskite Photovoltaics. *J. Phys. Chem. C* (2019).

117. Hou, Q. *et al.* Synergistic Hematite-Fullerene Electron-Extracting Layers for Improved Efficiency and Stability in Perovskite Solar Cells. *ChemElectroChem* **5**, 726–731 (2018).

118. Flak, D. *et al.* Electronic Structure and Surface Properties of Non-Stoichiometric Fe2O3-δ (α and γ) and Its Application in Gas Sensing. *Procedia Eng.* **47**, 257–260 (2012).

119. Tessler, N. & Vaynzof, Y. Preventing Hysteresis in Perovskite Solar Cells by Undoped Charge Blocking Layers. *ACS Appl. Energy Mater.* **1**, 676–683 (2018).

120. Mingorance, A. *et al.* Interfacial Engineering of Metal Oxides for Highly Stable Halide Perovskite Solar Cells. *Adv. Mater. Interfaces* **5**, 1800367 (2018).

121. Cheng, Y. *et al.* Decomposition of Organometal Halide Perovskite Films on Zinc Oxide Nanoparticles. *ACS Appl. Mater. Interfaces* **7**, 19986–19993 (2015).

122. Yang, J., Siempelkamp, B. D., Mosconi, E., De Angelis, F. & Kelly, T. L. Origin of the Thermal Instability in CH 3 NH 3 PbI 3 Thin Films Deposited on ZnO. *Chem. Mater.* **27**, 4229–4236 (2015).

123. Watanabe, H. & Seto, J. The Point of Zero Charge and the Isoelectric Point of γ-Fe 2 O 3 and α-Fe 2 O 3. *Bull. Chem. Soc. Jpn.* **59**, 2683–2687 (1986).

124. Kosmulski, M. *Chemical Properties of Material Surfaces*. **20011074**, (CRC Press, 2001).

125. *Principles and Practice of Bioanalysis*. (CRC Press, 2008).

126. Zohar, A. *et al.* What Limits the Open-Circuit Voltage of Bromide Perovskite-Based Solar Cells? *ACS Energy Lett.* **4**, 1–7 (2019).

127. Paasch, G. & Scheinert, S. Simulation and modeling of C–V curves of OLEDs with trap states for the holes. *Synth. Met.* **122**, 145–147 (2001).

128. Ahn, N. *et al.* Trapped charge-driven degradation of perovskite solar cells. *Nat. Commun.* **7**, 13422 (2016).

129. Almora, O., Aranda, C., Mas-Marzá, E. & Garcia-Belmonte, G. On Mott-Schottky analysis interpretation of capacitance measurements in organometal perovskite solar cells. *Appl. Phys. Lett.* **109**, 173903 (2016).

130. Duan, C. *et al.* Efficient Thick-Film Polymer Solar Cells with Enhanced Fill Factors via Increased Fullerene Loading. *ACS Appl. Mater. Interfaces* **11**, 10794–10800 (2019).

131. Shekhar, H. *et al.* Doping induced performance enhancement in inverted small molecule organic photodiodes operating below 1V reverse bias - Towards compatibility with CMOS for imaging applications. *Org. Electron.* **67**, 1–9 (2019).

132. Wang, Z. *et al.* Efficient and Air-Stable Mixed-Cation Lead Mixed-Halide Perovskite Solar Cells with n-Doped Organic Electron Extraction Layers. *Adv. Mater.* **29**, 1604186 (2017).

133. Bin, Z., Li, J., Wang, L. & Duan, L. Efficient n-type dopants with extremely low doping ratios for high performance inverted perovskite solar cells. *Energy Environ. Sci.* **9**, 3424–3428 (2016).

134. Kim, S. S., Bae, S. & Jo, W. H. Performance enhancement of planar heterojunction perovskite solar cells by n-doping of the electron transporting layer. *Chem. Commun.* **51**, 17413–17416 (2015).

135. Bitton, S. & Tessler, N. Electronic-ionic coupling in perovskite based solar cells: Implications for device stability. *Appl. Phys. Lett.* **117**, 133904 (2020).

136. Naab, B. D. *et al.* Mechanistic Study on the Solution-Phase n-Doping of 1,3-Dimethyl-2-aryl-2,3-dihydro-1 H -benzoimidazole Derivatives. *J. Am. Chem. Soc.* **135**, 15018–15025 (2013).

137. Jin, C. *et al.* Direct Solid-Phase Hydrogenation of Fullerenes. *J. Phys. Chem.* **98**, 4215–4217 (1994).

138. Said, A. A., Xie, J. & Zhang, Q. Recent Progress in Organic Electron Transport Materials in Inverted Perovskite Solar Cells. *Small* **15**, 1900854 (2019).

139. Zhu, X. *et al.* Perovskite Self-Passivation with PCBM for Small Open-Circuit Voltage Loss. *Energy Power Eng.* **12**, 257–272 (2020).

140. Liu, Z. *et al.* High-Performance Planar Perovskite Solar Cells Using Low Temperature, Solution-Combustion-Based Nickel Oxide Hole Transporting Layer with Efficiency Exceeding 20%. *Adv. Energy Mater.* **8**, 1703432 (2018).

141. Cheng, Y. *et al.* Impact of surface dipole in NiOx on the crystallization and photovoltaic performance of organometal halide perovskite solar cells. *Nano Energy* **61**, 496–504 (2019).

142. He, J. *et al.* Ligand-Free, Highly Dispersed NiO x Nanocrystal for Efficient, Stable, Low-Temperature Processable Perovskite Solar Cells. *Sol. RRL* **2**, 1800004 (2018).

143. Kokkin, D. L., Dewberry, D. & Steimle, T. C. The permanent electric dipole moment of nickel oxide, NiO. *Chem. Phys. Lett.* **609**, 1–5 (2014).

144. Yun, S.-C. *et al.* Amino acid salt-driven planar hybrid perovskite solar cells with enhanced humidity stability. *Nano Energy* **59**, 481–491 (2019).

145. Ogomi, Y. *et al.* All-Solid Perovskite Solar Cells with HOCO-R-NH 3 + I – Anchor-Group Inserted between Porous Titania and Perovskite. *J. Phys. Chem. C* **118**, 16651–16659 (2014).

146. Li, H., Zhang, C., Ma, Y., Mai, Y. & Xu, Y. Alanine induced structure reconstruction of PEDOT:PSS films in perovskite solar cells. *Org. Electron.* **62**, 468–473 (2018).

147. Gadelmawla, E. S., Koura, M. M., Maksoud, T. M. A., Elewa, I. M. & Soliman, H. H. Roughness parameters. *J. Mater. Process. Technol.* **123**, 133–145 (2002).

148. Shih, Y.-C. *et al.* Amino-Acid-Induced Preferential Orientation of Perovskite Crystals for Enhancing Interfacial Charge Transfer and Photovoltaic Performance. *Small* **13**, 1604305 (2017).

149. Jung, J. W., Chueh, C.-C. & Jen, A. K.-Y. A Low-Temperature, Solution-Processable, Cu-Doped Nickel Oxide Hole-Transporting Layer via the Combustion Method for High-Performance Thin-Film Perovskite Solar Cells. *Adv. Mater.* **27**, 7874–7880 (2015).

150. Mehl, J. & Schmidt, C. The Conductivities of Aqueous Solutions of Glycine, d,l-Valine, and l-Asparagine. *Div. Biochem. Univ. ofCalifornia Med. Sch.*

151. Zhao, C. *et al.* Revealing Underlying Processes Involved in Light Soaking Effects and Hysteresis Phenomena in Perovskite Solar Cells. *Adv. Energy Mater.* **5**, 1500279 (2015).

152. Shao, Y., Xiao, Z., Bi, C., Yuan, Y. & Huang, J. Origin and elimination of photocurrent hysteresis by fullerene passivation in CH3NH3PbI3 planar heterojunction solar cells. *Nat. Commun.* **5**, 5784 (2014).

153. Kavan, L. Electrochemistry and perovskite photovoltaics. *Curr. Opin. Electrochem.* **11**, 122–129 (2018).

154. Batmunkh, M. *et al.* Carbon Nanotubes in TiO 2 Nanofiber Photoelectrodes for High-Performance Perovskite Solar Cells. *Adv. Sci.* **4**, 1600504 (2017).

155. Niu, G. *et al.* Study on the stability of CH 3 NH 3 PbI 3 films and the effect of post-modification by aluminum oxide in all-solid-state hybrid solar cells. *J. Mater. Chem. A* **2**, 705–710 (2014).

156. Mora-Seró, I. *et al.* Implications of the Negative Capacitance Observed at Forward Bias in Nanocomposite and Polycrystalline Solar Cells. *Nano Lett.* **6**, 640–650 (2006).

157. Noh, M. F. M., Arzaee, N. A. & Teridi, M. A. M. Effect of Oxygen Vacancies in Electron Transport Layer for Perovskite Solar Cells. in *Solar Cells* 283–305 (Springer International Publishing, 2020). doi:10.1007/978-3-030-36354-3_11

158. Boyd, C. C., Cheacharoen, R., Leijtens, T. & McGehee, M. D. Understanding Degradation Mechanisms and Improving Stability of Perovskite Photovoltaics. *Chem. Rev.* **119**, 3418–3451 (2019).

159. Boyd, C. C. *et al.* Overcoming Redox Reactions at Perovskite-Nickel Oxide Interfaces to Boost Voltages in Perovskite Solar Cells. *Joule* **4**, 1759–1775 (2020).

160. Yuan, J. *et al.* Metal Halide Perovskites in Quantum Dot Solar Cells: Progress and Prospects. *Joule* **4**, 1160–1185 (2020).

161. Akkerman, Q. A., Rainò, G., Kovalenko, M. V. & Manna, L. Genesis, challenges and opportunities for colloidal lead halide perovskite nanocrystals. *Nat. Mater.* **17**, 394–405 (2018).

162. ten Brinck, S. & Infante, I. Surface Termination, Morphology, and Bright Photoluminescence of Cesium Lead Halide Perovskite Nanocrystals. *ACS Energy Lett.* **1**, 1266–1272 (2016).

163. Sanehira, E. M. *et al.* Enhanced mobility CsPbI 3 quantum dot arrays for record-efficiency, high-voltage photovoltaic cells. *Sci. Adv.* **3**, (2017).

164. Ma, R. *et al.* Improving open-circuit voltage by a chlorinated polymer donor endows binary organic solar cells efficiencies over 17%. *Sci. China Chem.* **63**, 325–330 (2020).